Paper Waste Sludge Magnetic Biochar Sorbs Multispecies from Wastewater

By

Masale Clement Manoko

27126855

Supervisor: Prof. Evans MN Chirwa

Co-Supervisor: Dr Katlego Makgopa

Dissertation Submitted in fulfilment for the degree of

Master of Science (Applied Sciences) Water Utilization

In the Faculty of Engineering, Built Environment and Information Technology
University of Pretoria

Pretoria

2022

DECLARATION

I, **Masale Clement Manoko** with student number **27126855** do hereby declare the authenticity of this research work as my own to the best of my knowledge. As far as I am aware this work has not been submitted in part or entirely to any other higher learning for a qualification and that all references have been acknowledged.

SIGNED: 30th Day of March 2022

Masale Clement Manoko

Paper Waste Sludge Magnetic Biochar Sorbs Multispecies from Wastewater

ABSTRACT

Adsorption of pollutants from wastewater by demineralized and synthesized biochar derived from paper waste sludge has been received significant interest in recent studies. however there has been minimal research on non-demineralized paper waste sludge derived biochar uses for pollutant adsorption. The main focus of this study to prepare a neat non-demineralized paper waste sludge and a magnetized variant by the introduction of Fe^{3+} and Fe^{2+} salts to the feedstock and subsequent slow pyrolysis.

Adsorption studies were performed to assess the efficiency of biochar's removal of phosphorus, selenate, and methylene blue as a function of carbonization temperature, biochar loading, adsorbate concentration, pH, and contact time. MBC-SPS 450 was observed to be the best performing adsorbate with adsorption capacities of phosphorus 48.83 mg/g, Selenium 58.43 mg/g, and Methylene blue 5.92 mg/g. MBC SPS 450°C was selected as the desirable adsorbent due to excellent adsorption efficiencies, lower carbonization temperature, magnetic separation from solution, and low loading requirements with an optimum loading of 5 g/L. The biochar can be regenerated up to three times with excellent efficiencies observed. Its intrinsic characteristics make it a good adsorbent that can be regenerated and reused with high efficiencies observed. The results observed demonstrates paper waste sludge-derived biochar as a good low-cost alternative to activated carbon adsorbent in wastewater treatment with additional benefits that its part of closing the loop in the fiber recycling process.

Keywords: magnetic biochar, wastewater treatment, selenate, phosphorus, methylene blue, adsorption

ACKNOWLEDGEMENTS

I am immensely grateful to Mpact Paper and Mpact Recycling management who believed in me and availed resources and time for me to go and pursue my studies, to John hunt, Ntuthuko Khoza and Howard Emmert I remain eternally grateful for all you have done for me through this process.

To my supervisor Professor Evans Chirwa, I am grateful for his guidance and belief in the project from its inception, your insights and encouragement carried me through the difficult times and my co-supervisor Dr Katlego Makgopa I am immensely grateful for your contribution to this project, your guidance and words of encouragement also carried m through this project.

To my wife (Maserole) and children (Ngwedi and Mahlatse) Manoko I am eternally grateful for the support and sacrifices, I would not have gone far if it was not for your support and encouragement.

To Lehlogonolo Shane Tabana I will eternally remain grateful for your kind heart, patience and assistance through my studies, you have been a great friend and mentor throughout, may God eternally bless you.

Lastly, I acknowledge all the people that have been a part of my career development which has led me to be where I am and fulfilling my potential, it takes a village to raise a child.

Finally, the lord almighty, who is my source of strength and hope I am thankful.

DEDICATION

To my wife and children

For encouraging and allowing me the time to complete this work.

To my sisters and parents

For always believing in me and offering support at all times.

To my employer (Recycling Consolidated Holdings)

For availing all resources and granting me the space and time to complete this work.

To Lehlogonolo Shane Tabana

For holding my hand and being the source of encouragement and guidance.

Table of Contents

DECLARATION 1
ABSTRACT i
ACKNOWLEDGEMENTS ii
DEDICATION iii
LIST OF FIGURES viii
LIST OF TABLES x
ACRONYMS xi
LIST OF SYMBOLS xii
PUBLICATIONS xiii
INTRODUCTION 1
1.1 Background 1
1.2 Problem statement 2
1.3 Hypothesis 3
1.4 Aims and objectives 4
1.5 Dissertation outline 4
LITERATURE REVIEW 6
2.1 Paper waste sludge from pulp and paper mills 6
2.2 Biomass feedstock 7
2.2.1 Cellulose 8
2.2.2 Hemicellulose 9
2.2.3 Lignin 10
2.2.4 Extractives and Ash 11
2.3 Utilization of Paper Waste Sludge & Rejects 11
2.3.1 Land application 12
2.3.2 Integration of paper waste sludge in materials 12
2.3.3 Energy recovery 12
2.3.4 Thermochemical conversion 13
2.3.4.1 Thermochemical conversion of biomass 13
2.3.5 Combustion 14
2.3.6 Gasification 15
2.3.7 Pyrolysis 15
2.4 Pyrolytic degradation of lignocellulosic biomass 17
2.4.1 Pyrolysis of cellulose 18
2.4.2 Pyrolysis of hemicellulose 19

2.4.3 Pyrolysis of lignin 20
2.5 Pyrolysis products 20
2.5.1 Flue gas/ Syngas 21
2.5.2 Pyrolysis oil 21
2.5.3 Biochar 21
2.6 Adsorption 24
2.6.1 Nutrients and adsorption 25
2.6.2 Adsorption of selenium 28
2.6.3 Adsorption of methylene blue 29
2.7 Adsorption isotherms 29
2.7.1 Langmuir isotherm model 30
2.7.2 Freundlich isotherm model 31
2.7.3 Sips isotherm model 31
2.8 Adsorption kinetics 32
MATERIALS AND METHODS 34
3.1 Materials 34
3.1.1 Source and feedstock preparation 34
3.1.2 Chemicals 34
3.1.3 Preparation of adsorbents and carbonization 34
3.2 Physio-chemical characterization 35
3.2.1 Proximate analysis 35
3.2.2 Ultimate analysis 35
3.2.3 Fourier-transform infrared spectroscopy 36
3.2.4 X-ray diffraction 36
3.2.5 X-Ray Fluorescence 36
3.2.6 Brunauer-Emmett-Teller 37
3.2.7 Scanning electron microscopy 37
3.2.8 Scanning electron microscopy and energy dispersive x-ray spectroscopy 37
3.2.9 Transmission electron microscopy 38
3.3 Adsorption studies 38
3.3.1 Design 38
3.3.2 The effect of carbonization temperature 38
3.3.3 The effect of adsorbent loading 39
3.3.4 The effect of pH and contact time 39
3.3.5 The effect of competition for sites 40

3.3.6 Determination of adsorption mechanism 40
3.3.7 Determination of Adsorption Isotherms 40
3.3.8 Determining of Reusability and Regeneration Potential of Biochars 41
3.3.9 Modelling of Adsorption Kinetics 41
CHARACTERISATION 43
4.1 Biochar yields 43
4.2 Physicochemical characterization 43
4.2.1 Proximate analysis and ultimate analysis 43
4.2.2 X-ray fluorescence 47
4.2.3 Fourier transform infrared spectroscopy 49
4.2.4 Brunauer-Emmett-Teller analysis specific surface area 51
4.2.5 Scanning electron microscopy (SEM) 51
4.2.6 Energy dispersive x-ray spectroscopy and elemental mapping 54
4.2.7 Transmission Electron Microscopy 57
Adsorption studies 58
5.1 Effect of carbonization temperature 58
5.1.1 Phosphorus removal 58
5.1.2 Selenate removal 59
5.1.3 Methylene blue removal 60
5.2 Effect of adsorbent loading 61
5.2.1 Phosphorus 61
5.2.2 Selenium 62
5.2.3 Methylene blue 62
5.3 Effect of pH and contact time 63
5.3.1 Phosphorus 63
5.3.2 Selenium 64
5.3.3 Methylene Blue 65
5.4 Adsorption mechanism 66
5.4.1 Selenium 66
5.4.2 Phosphorus 68
5.4.3 Methylene Blue 70
5.5 Adsorption Isotherms 71
5.5.1 Phosphorus 72
5.5.2 Selenate 73
5.5.3 Methylene Blue 75

5.6 Adsorption kinetics 75
5.7 Regeneration and reusability of Biochar 78
5.7 Effect of competing ions 80
Conclusions and recommendations 82
References 84
APPENDICES 93
Characterization 93
Appendix A: XRD patterns 93
Appendix B: FTIR Spectra 94
Appendix C: SEM micrographs 95
Appendix D: EDS Spectra and elemental mapping 97
Appendix E: TEM micrographs of pristine and synthesized biochar. 101
Adsorption 103
Appendix F : Adsorption isotherms. 103
Appendix G : Adsorption kinetic plots and parameters. 105
Appendix H: UV Spectrophotometer calibration data 110

LIST OF FIGURES

Figure 2. 1: Biomass components (Wang & Luo, 2016) 7
Figure 2. 2: Rejected fiber from a recycling mill, RPS (a) and SPS (b). (Mpact Springs Mill-South Africa). 8
Figure 2. 3: Basic structure of Cellulose (Wang *et al*, 2016b). 9
Figure 2. 4: Fundamental chemical structure of sugar units in hemicellulose (Wang & Luo, 2016). 10
Figure 2. 5: Three basic structural units of lignin. 10
Figure 2. 6: Thermochemical conversion pathways and their products (Gent *et al*, 2017). 14
Figure 2. 7: Thermogravimetric curves (TG) and derivative thermal gravimetric curve of the lignocellulosic biomass components (Assis & Chirwa, 2021). 18
Figure 2. 8: Pyrolytic reactions of cellulose (Basu, 2018). 19
Figure 2. 9: Biochar modification processes (Ok *et al*, 2018). 24
Figure 2. 10: Types of adsorption isotherms (Mohammed *et al*, 2020) 30
Figure 4. 1: Thermogravimetric (TG) and differential thermogravimetric (dTG) curves of SPS and RPS.X-ray diffraction 45
Figure 4. 2: XRD patterns for (a) RPS and (b) MBC SPS 46
Figure 4. 3: FTIR spectra of (a) RPS and (b) MBC-SPS 50
Figure 4. 4: SEM images RPWS variants at 20 µ magnification (a) SPS and (b) RPS. 52
Figure 4. 5: SEM images of resultant SPS 450ºC pristine biochar (a) 2µ magnification and (b) 200µ magnification. 52
Figure 4. 6: SEM images of resultant RPS 450ºC synthesized biochar (a) 2µ magnification and (b) 200µ magnification. 53
Figure 4. 7: SEM images of resultant 650 ºC synthesized biochar (a) RPS at 2µ magnification, (b) RPS at 200µ magnification, (c) SPS at 2µ magnification, (d) SPS at 200µ magnification. 54
Figure 5. 1: Phosphorus Removal efficiencies of biochar. 58
Figure 5. 2: Selenate Removal efficiencies of biochar. 60
Figure 5. 3: Methylene blue Removal efficiencies of biochar. 61
Figure 5. 4: Effect of biochar loading on adsorption efficiencies for P, Se, and MB. 62
Figure 5. 5: Effect of pH and time on phosphorus adsorption efficiency. 64
Figure 5. 6: Effect of pH and time on selenate adsorption efficiency. 65
Figure 5. 7: Effect of pH and time on methylene blue adsorption efficiency. 66
Figure 5. 8: EDS elemental mapping of Spent Biochar after selenate adsorption. 67
Figure 5. 9: XRD plots for neat and spent biochar. 68
Figure 5. 10: EDS elemental mapping of Spent Biochar after phosphorus adsorption. 69
Figure 5. 11: EDS elemental mapping of Spent Biochar after methylene blue adsorption. 71
Figure 5. 12: Phosphorus adsorption isotherms at pH 5 73
Figure 5. 13: Selenate adsorption isotherms at pH 9 74
Figure 5. 14: Methylene blue adsorption isotherms 75
Figure 5. 15: Phosphorus adsorption kinetics (pH 7) 76
Figure 5. 16: Selenium adsorption kinetics (pH 7) 77
Figure 5. 17: Methylene blue adsorption kinetics (pH 7) 77
Figure 5. 18: Adsorption efficiencies on regenerated biochar (a) phosphorus, (b) Selenate and (c) Methylene Blue 80
Figure 5. 19: Effect of competition for adsorption sites 81
Appendix A- 1: XRD Plot MBC RPS 93
Appendix A- 2: XRD Plot SPS 93

Appendix B- 1: FTIR spectra of MBC-RPS 94
Appendix B- 2: FTIR spectra of SPS 94
Appendix C- 1: SEM images of resultant synthesized 450ºC biochar (a) MBC-RPS at 2µ magnification, (b) MBC-RPS at 200µ magnification, (c) MBC-SPS at 2µ magnification, (d) MBC-SPS at 200µ magnification 95
Appendix C- 2: SEM images of resultant 550ºC pristine biochar (a) RPS at 2µ magnification, (b) RPS at 200µ magnification, (c) SPS at 2µ magnification, (d) SPS at 200µ magnification 95
Appendix C- 3: SEM images of resultant 550ºC synthesized biochar (a) RPS at 2µ magnification, (b) RPS at 200µ magnification, (c) SPS at 2µ magnification, (d) SPS at 200µ magnification 96
Appendix C- 4: SEM images of resultant 650ºC pristine biochar (a) RPS at 2µ magnification, (b) RPS at 200µ magnification, (c) SPS at 2µ magnification, (d) SPS at 200µ magnification 96
Appendix D - 1: EDS Spectra of RPWS (a) SPS and (b) RPS. 97
Appendix D - 2: EDS Spectra of 450 ºC pristine biochar (a) SPS and (b) RPS 97
Appendix D - 3: Elemental mapping of 650 ºC synthesized biochar (a) SPS and (b) RPS. 97
Appendix D - 4: EDS spectra and elemental mapping micrographs of resultant MBC 450ºC biochar (a) RPS spectra, (b) RPS elemental map, (c) SPS spectra, (d) SPS elemental map ...98
Appendix D - 5: EDS spectra of resultant pristine 550ºC biochar (a) RPS spectra and (b) SPS spectra 98
Appendix D - 6: EDS spectra and elemental mapping micrographs of resultant MBC 550ºC biochar (a) RPS spectra, (b) RPS elemental map, (c) SPS spectra, (d) SPS elemental map ...99
Appendix D - 7: EDS spectra and elemental mapping micrographs of resultant pristine 650ºC biochar (a) RPS spectra, (b) RPS elemental map, (c) SPS spectra, (d) SPS elemental map. ..99
Appendix D - 8: EDS spectra of resultant MBC 650ºC biochar (a) RPS spectra and (b) SPS spectra 100
Appendix E- 1: TEM micrographs of resultant pristine and magnetic 550ºC biochar (a) SPS, (b) RPS, (c) MBC SPS, (d) MBC RPS 101
Appendix E- 2: TEM micrographs of resultant pristine and magnetic 650ºC biochar (a) SPS, (b) RPS, (c) MBC SPS, (d) MBC RPS 102
Appendix F - 1: Phosphorus adsorption isotherms at (a) pH 7 and (b) pH 9 104
Appendix F - 2: Selenate adsorption isotherms at (a) pH 5 and (b) pH 7 104
Appendix G- 1: Phosphorus Pseudo-First Order plots (a) pH 5, (b) pH 7 and (b) pH 9. 106
Appendix G- 2: Phosphorus Pseudo-Second Order plots (a) pH 5 and (b) pH 9. 107
Appendix G- 3: Selenium Pseudo-First Order plots (a) pH 5, pH 7 and (b) pH 9 108
Appendix G- 4: Selenium Pseudo-Second Order plots (a) pH 5 and (b) pH 9 109
Appendix G- 5: Adsorption kinetic model parameters 110
Appendix H- 1: UV Spectrophotometer calibration 110
Appendix H- 2: UV Spectrophotometer calibration plot 111

LIST OF TABLES

Table 2. 1: Composition of paper waste sludge (wt.%, db) (Brown *et al*, 2017) 10
Table 2. 2: Operational parameters that govern each thermochemical conversion process. ...14
Table 2. 3: Pyrolysis processes 16
Table 2. 4: Common adsorbents 25
Table 4. 1: Biochar yields 43
Table 4. 2: Proximate and Ultimate analysis results 44
Table 4. 3: Raw sample and biochar XRF results 48
Table 4. 4: Brunauer-Emmet and teller analysis results 51
Table 4. 5: Elemental Analysis of raw SPS and RPS (wt.%, d.b) 54
Table 4. 6: Elemental Analysis of pristine resultant biochar (wt.%, d.b). 55
Table 4. 7: Elemental Analysis of synthesized resultant biochar (wt.%, d.b) 56
Table 5. 1: XRF analysis of neat and spent biochar. 67
Table 5. 2: Elemental analysis of spent biochar after selenate adsorption (wt.%)(d.b) 67
Table 5. 3: XRF analysis of neat and spent biochar after phosphorus adsorption. 69
Table 5. 4: Elemental analysis of spent biochar after phosphorus adsorption (wt.%, d.b) 70
Table 5. 5: XRF analysis of neat and spent biochar after methylene blue adsorption. 70
Table 5. 6: Elemental analysis of spent biochar after methylene blue adsorption. 71
Table 5. 7: Phosphorus adsorption isotherm parameters. 72
Table 5. 8: Selenate adsorption isotherm parameters. 74
Table 5. 9: Selenate adsorption isotherm parameters. 75
Table 5. 10: Adsorption kinetic model parameters 78

ACRONYMS

ATR	Attenuated Total Reflection
BET	Brunauer-Emmett Teller
GDP	Gross Domestic Product
EDS	Energy Dispersive X-Rat Spectroscopy
FTIR	Fourier Transform Infrared Spectroscopy
IUPAC	International Union of Pure Applied Science
LOI	Loss on Ignition
PAH	Polycyclic Aromatic Hydrocarbons
PAMSA	Paper Manufacturing Association of South Africa
SEM	Scanning Electron Microscopy
TCD	Thermal Conductivity Detector
TEM	Transmission Electron Microscopy
TGA	Thermogravimetric Analysis
TPD	Temperature Programmed Desorption
WHO	World Health Organization
XRD	X-Ray Diffraction
XRF	X-Ray Fluorescence

LIST OF SYMBOLS

C_i	Initial solution concentration (mg/L)
C_e	Equilibrium concentration of adsorbate (mg/L)
C_t	Solution concentration at a time T (mg/L)
K_L	Langmuir equilibrium constant (L/mg), also referred to as b
K_F	Freundlich equilibrium constant (L/g)
K_1	Lagergren rate constant (min^{-1})
K_2	Pseudo-second order rate constant (g/mg.min)
m	Mass of adsorbent (g)
n	Adsorption intensity
n	Adsorption intensity
q_e	equilibrium adsorption capacity (mg/g)
q_m	maximum adsorption capacity (mg/g)
R_L	Separation Factor
T	Time (min)
V	Solution volume (L)
Wt.%	Weight percentage

PUBLICATIONS

Peer Reviewed Articles

1. Manoko, M.C., Chirwa, E.M. and Makgopa, K., 2021. Structural Elucidation of Magnetic Biochar Derived from Recycled Paper Waste Sludge. *Chemical Engineering Transactions*, 88, pp.193-198. (https://doi.org/10.3303/CET2188032).

2. Manoko, M.C., Chirwa, E.M. and Makgopa, K., 2021. Non-demineralized paper waste sludge derived magnetic biochar as sorbs for removal of methylene blue, phosphorus, and selenate in wastewater. *Journal of Cleaner Chemical Engineering* PRES'21 Special Issue. 2772-7823, (https://doi.org/10.1016/j.clce.2022.100048)

Conference Presentations

Structural Elucidation of Magnetic Biochar Derived from Recycled Paper Waste Sludge. 24th conference on Process Integration for Energy Saving and Pollution Reduction. 31st October- - 3rd November 2021, Brno, Czech Republic. (Online Presentation)

INTRODUCTION

1.1 Background

The paper industry produces large volumes of paper waste sludge, these waste products have found little application in the circular economy. There have been studies to explore the use of recycled paper waste sludge (RPWS) in energy recoveries and fuel production (Brown *et al*, 2017; Ridout *et al*, 2015). However, there has been limited studies in wastewater treatment where non-demineralized carbonized recycled paper waste sludge was used as a biomass feedstock to produce adsorbents. (Wang *et al*, 2021) used calcium-rich RPWS as a feedstock to produce biochar that was used in the adsorption of phosphorus from aqueous solution with excellent results, interest in biochar has increased significantly in recent years due to its viability for use as an adsorbent in wastewater treatment, (Chen *et al*, 2011) created magnetic biochar using orange peel and metal oxide many researchers have used various synthesized biomass feedstocks to adsorb different water pollutants.

Biochar has many multidisciplinary advantages, some of the known benefits include; adsorption of nutrients from wastewater, stable carbon storage, prevention of greenhouse gas emission due to biomass degradation, increasing available nutrients for plant growth, improve water retention in soils, reduce fertilizer use by prevention of nutrients leaching from the soil, reduction of methane and nitrous oxide from the soil, can be used as a solid fuel for heat generation and production of activated carbon (Hornung, 2014; Xiang *et al*, 2020). Biochar offers a viable adsorbent for the removal of nutrients and other pollutants from wastewater and various researchers have applied various ways of synthesizing biochar to produce adsorbents that suit certain characteristics (Wang *et al*, 2016b). Paper waste sludge (PWS) from recycled board mills contains coating agents such as kaolinite, calcium carbonate, titanium dioxide which are potentially good adsorbents of water pollutants (Mouni *et al*, 2018; Setthaya *et al*, 2017; Wang *et al*, 2021). Other researchers demineralize biochar feedstocks, a process that leads to loss of intrinsic properties that may be of benefit in wastewater treatment.

This practice leads to the loss of embedded minerals that can be beneficial to the resultant biochar's adsorption efficiency. The fillers and coating agents introduce the mineral content found in RPWS, kaolin has seen the widest use followed by calcium carbonate and to a lesser degree talc and titanium dioxide (Bundy & Ishley, 1991) a phenomenon still observed in South African recycled board mills as the technology employed has not significantly changed from the 1970s.

1.2 Problem statement

Anthropogenic activities that lead to the discharge of poorly treated industrial and domestic wastewater into aquatic systems is a continuous problem in many societies, excessive nutrients in aquatic systems lead to eutrophic conditions (Han *et al*, 2019), effluent from certain industrial areas contain dyes and macro-nutrients which can lead to adverse health effects for the receiving ecosystems and human health. Pollution caused by both domestic and industrial wastewater discharge in receiving water bodies is one of the most widespread challenging environmental problems, this problem emanating from inadequate treatment technologies, overloading of treatment plants, and poorly treated wastewater discharge (Morrissey, 2020). Discharged nutrients and industrial wastewaters have been proven to support the growth of algae and other aquatic plants which creates eutrophic conditions in the receiving bodies (Wang *et al*, 2021), while dyes contained in industrial effluent like methylene blue contribute to the turbidity of receiving water bodies and may be mutagenic and carcinogenic to humans (Vedula & Yadav, 2022). Selenium is also a by-product of production in industries such as mining, metallurgy and is widely used in electronics such as photocells, light meters, solar cells, and the glass industry (Hong *et al*, 2020). It is expected to see wider applications in the future as more and more solar cells will be manufactured as the world moves further towards green energy applications (Benis *et al*, 2022).

There is minimal research that has focused on the use of non-demineralized paper waste sludge derived from a recycled paper mill with the primary intention of producing magnetic biochar for application in wastewater treatment. Biochar loaded with magnetic metal oxides derived from metal salts is referred to as magnetic biochar (Xiang *et al*, 2020). It is generally produced by co-pyrolyzing biomass with metal chloride solutions to negate the difficulty of removing biochar from process wastewater (Yang *et al*, 2020). Researchers such as (Chen *et al*, 2011) created magnetic biochar by combining iron oxide and biochar formation during pyrolysis primarily for removal of contaminants in wastewater, harnessing their magnetic properties for their easy removal by magnets for regeneration and reuse (Feng *et al*, 2021b). To adsorb nutrients from wastewater, activated carbon, zeolites, polymeric adsorbents, clay minerals, porous silica, and zeolites have all been employed, with activated carbon having the greatest applications due to its high surface area, porous structure, and durability, etc. (Almanassra. *et al*, 2021).

The disadvantage of activated carbon is that it has relatively weak (negative) surface charged groups, which results in poor adsorption of anions such as phosphates. (Miyazato *et al*, 2020), and during the activation process, acidic wastewater is generated which require further treatment is generated while minerals like calcium carbonate are washed out reducing the adsorption capacity those minerals present (Wang *et al*, 2021).

(Godlewska *et al*, 2020) found that the adsorption capacity of biochar increased due to the increase of positive charge on the surface of biochar, however, it was also found that co-pyrolyzing biomass with magnetic precursors (iron oxides, natural iron ores, and transitional metal salts) produces biochar with the reduced surface area when compared to pristine biochar produced from the same feedstocks without the magnetic precursor (Chen *et al*, 2011), typically Al, Fe, La, and Mg salts have been used in impregnation to improve adsorption capacity of negatively charged anions (Li *et al*, 2016a). RPWS also contains titanium dioxide (TiO_2) which is a superior photocatalyst due to properties such as non-toxicity, non-photocorrosion, photocatalytic oxidation, and thermal stability (Setthaya *et al*, 2017). These clays typically have high surface areas and an additional property that they are negatively charged this makes them suitable unmodified adsorbents for cation adsorption from wastewater (Benis *et al*, 2022).

Demineralization of RPWS does not confine itself to the circular economy principle as acidic waste is produced which will require further disposal. Carbonization of RPWS as presents an opportunity to avoid further waste generation and the intrinsic characteristics of the minerals found in the sludge matrix have advantageous properties in wastewater treatment such as efficiently purifying phosphorus-containing wastewater (Wang *et al*, 2021). Researchers such as (Li *et al*, 2020) reported equilibrium removal capacities of 213.22 ±13.57 mg/g using similar adsorbents, these observations support the argument of not washing nor demineralizing RPWS feedstock meant for biochar production.

1.3 Hypothesis

Non-demineralized paper waste sludge from recycling board mills can be used as an adsorbent to remove methylene blue, phosphorus and selenate from wastewater. The presence of filler and coating agents such as calcium carbonate, kaolinite and titanium dioxide in the feedstock matrix can be beneficial in the removal of pollutants from wastewater by the resultant biochar after carbonization.

Magnetizing the biochar can add additional adsorption capacity and enable easy recovery of the biochar for nutrient recovery and regeneration purposes. The performance of paper waste sludge derived magnetic biochar is expected to be comparable or better to that of other biomass-based adsorbents like activated carbon and synthesized biomass derived biochars due to the abundant high BET surface area and the presence of coating agents within the biochar matrix.

1.4 Aims and objectives

This study aims to evaluate the ability of both neat and magnetized paper waste sludge-based biochar to remove methylene blue, phosphorus and selenate from wastewater. Required conditions in the production and utilization of resultant biochar were carefully considered, the main objectives of the study are to:

i. Establish the most suitable carbonization temperature and conditions for paper waste sludge,
ii. Establish the physical and chemical properties of both pristine and magnetized biochar using several characterization techniques,
iii. Investigate the effect of filler, coating agents and magnetite within the biochar matrix on the adsorption capacity,
iv. Establish methylene blue, phosphorus and selenate adsorption mechanisms using equilibrium isotherms,
v. Investigate the adsorption process kinetics,
vi. Investigate the regeneration and reusability of the resultant biochars, and
vii. Compare performance of the resultant biochars wit other adsorbents currently available.

1.5 Dissertation outline

Chapter 1: This chapter provides the background on environmental challenges encountered due to pollution by methylene blue, phosphorus and selenate' s elevated presence in wastewater. It also provides a brief overview of the paper industry challenge in sludge management and disposal and why paper waste sludge from recycling board mills can be used as an adsorbent for pollutant removal. It also provides the problem statement and objectives of this study.

Chapter 2: This chapter presents the literature review for this study. Its focal areas are: (1) Recycled paper waste sludge (RPWS) and management practices, (2) Current RPWS uses and developments in its valorization, (3) Conversion processes of RPWS into various industry products, (4). Carbonization of RPWS, (5) Synthesis techniques for RPWS in biochar production, (6) Biochar and magnetized biochar, and (7) Desorption potential of non-demineralized RPWS.

Chapter 3: The materials, experimental procedures, methodologies used, characterization, and analytical techniques used in this study are all described in this chapter. It is split into two sections, namely: characterization techniques and adsorption studies.

Chapter 4: This chapter details the characterization study results of the resultant biochars. The results include yields, elemental composition, phase purity & functional group identification, morphology, elemental mapping and BET surface area.

Chapter 5: This chapter presents results from the adsorption studies of methylene blue, phosphorus and selenate. The results are divided into design, effects of variables such as (carbonization temperature, pH & contact time), adsorption mechanisms, adsorption isotherms, competition for adsorption sites, spent biochar reusability and regeneration potential, and adsorption kinetics

Chapter 6: This chapter presents the results based final conclusions and recommendations for future studies.

LITERATURE REVIEW

2.1 Paper waste sludge from pulp and paper mills

The paper and pulp industry contributes an estimated R 1.45 billion 0.53 % to the Gross Domestic Product (GDP) of South Africa according to the Paper Manufacturing Association of South Africa (PAMSA) 2019 report (Pamsa, 2019).The industry largely produces products from virgin wood fiber (pulp derived from sustainable plantations) and recycled paper fiber (pulp derived from recovered waste paper) (Pamsa, 2019). Pulp and paper mills utilize recycled fiber or virgin pulp in the production of a variety of finished products such as Kraft board and ceiling board. There are different processes involved in the paper and pulp manufacturing processes (Bajpai, 2018) which can be grouped into five main categories; *viz* mechanical (grinding and refining), chemical (*i.e.*, Kraft and sulphite process), chemo-mechanical (batch and continuous systems) and thermo-mechanical paper making (Faubert *et al*, 2016).

During the various production stages in the paper, production waste is generated, these wastes can be categorized as primary reject paper waste (RPS) and secondary paper waste sludge (SPS) which are common in recycled fiber mills. RPS emanates from the screening processes before the paper machine while secondary paper waste sludge (SPS) emanates from the wastewater clarification plants within the mill. Typically, RPS is dried in holding areas while moisture from SPS is reduced using filter presses within the plant before disposal.

Depending on the mill type and feedstock, the paper and pulp industry generates significant quantities of waste, it is estimated that mills generate about 50 kg – 500 kg of waste for every ton of paper product produced. Organic matter (cellulose fibers from recycled paper or wood with added organic components), inorganic fillers and coatings (mostly calcium carbonate, kaolinite, and talc), and water make up the majority of these wastes.(Méndez *et al*, 2009; Monte *et al*, 2009).

2.2 Biomass feedstock

Organic matter derived from living or recently lived species, such as plants, animals, and microorganisms, as well as metabolized organic matter or excreta from or by organisms, is referred to as biomass. (Dhyani & Bhaskar, 2019; Wang & Luo, 2016) It is commonly referred to as lignocellulosic biomass, and it refers to plants or plant-based materials that are not intended for food or feed, with a concentration on agriculture and forestry by-products. Biomass is made up of a wide range of plant and animal species, each having its own shape and chemical content. Plant biomass is made up of a wide range of polymeric compounds with multifunctional molecular structures, resulting in a wide range of morphologies. It is characterized by a high carbon to oxygen ratio with a lower carbon to hydrogen ratio when compared to oils due to an abundance of hydroxyl groups. The distinct differences in elemental composition, morphology, and molecular structures and the variety of plant phenotypes present in bio-renewable feedstocks are of great importance when considerations are made for tailored future industrial value chains (Pandey *et al*, 2015). As illustrated in Figure 2.1, the cell wall of plants is made up of three primary components: cellulose, hemicellulose, and lignin. The components are irregularly distributed throughout the cell wall, forming the skeleton, connecting material, and hard solids. The plant cell's skeleton is composed of cellulose molecules that appear as tubes and form strong microfibers, with amorphous connecting material (hemicellulose) filling the inner space and hard solid lignin filling the outer space. (Manuel, 2010; Wang & Luo, 2016).

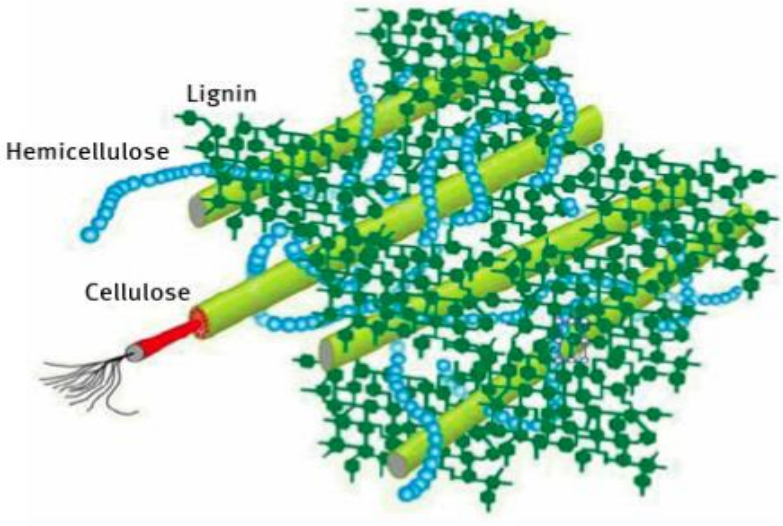

Figure 2. 1: Biomass components (Wang & Luo, 2016)

Figure 2.2 illustrates lignocellulosic biomass, which includes paper waste sludge. Staples and metals from ring binders, sand, and glass are removed before the fibers are discarded, depending on the mill and techniques used. Because of the low quality of the fiber, these fibers are often dumped as a blend with plastics.

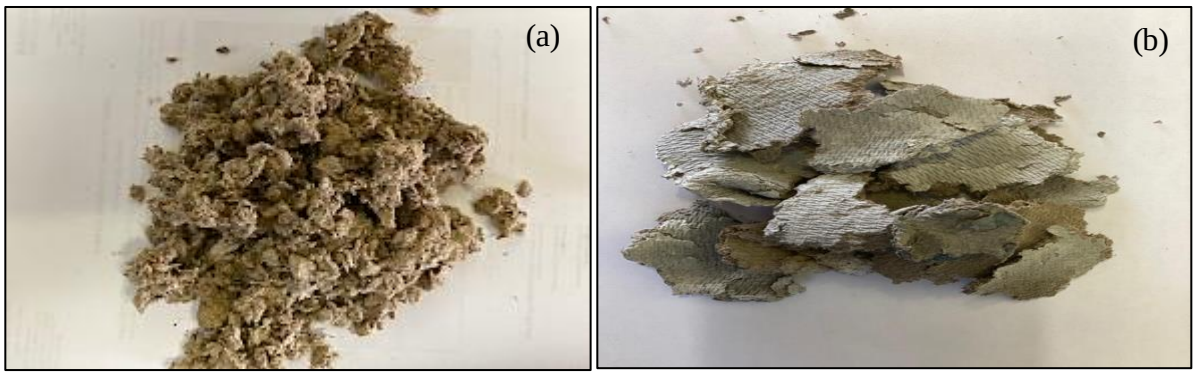

Figure 2. 2: Rejected fiber from a recycling mill, RPS (a) and SPS (b). (Mpact Springs Mill-South Africa).

SPS is collected in bulk at clarification plants within fiber recycling mills, where flocculation and sedimentation are the primary phases separation process. RPS is generated at screening processes before the board machines. Depending on the recovered fiber being processed the sludge is predominantly characterized by unusable short degraded fibers, fines and fillers, and other contaminants like glue, ink, inorganics, and clay (Monte *et al*, 2009). Carbon (C), hydrogen (H), and oxygen (O) are the main constituents of this type of biomass, the distribution of these atoms forms complex macromolecules that are composed of aromatic compounds (lignin) and carbohydrates (Cellulose and Hemicellulose) (Dufour, 2016).

2.2.1 Cellulose

As per Table 2.1, cellulose is by far the most common polymer on the earth, with an average molecular weight of 100 000 g/mol and contributing for 40 % - 60 % of lignocellulosic biomass. Since cellulose is comprised of glucose molecules, it is commonly referred to as a glucose polymer. Cellulose's chemical formula is $(C_6H_{10}O_5)_n$ (Ragauskas, 2014). Figure 2.3 with a primarily crystalline structure linked by glycosidic linkages that form the skeleton of the plant cell and is the principal element of wood and another biomass. The linkages in cellulose produce microfibril that are exceptionally robust and resistant to chemical attack due to a high degree of hydrogen bonding that can occur between cellulose chains. (Wang & Luo, 2016).

Hydrogen bonding between cellulose chains prevents the molecules from bending, which is required for the hydrolytic breakdown of glycosidic linkages, making the polymers more rigid. Through hydrolysis, cellulose can be converted to a cellobiose repeating unit ($C_{12}H_{22}O_{11}$), and then to glucose ($C_6H_{10}O_5$) (Hornung, 2014).

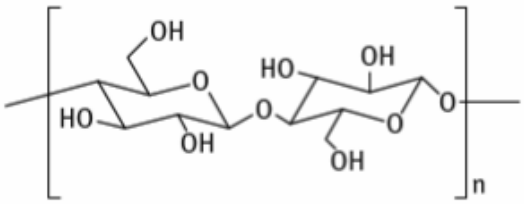

Figure 2. 3: Basic structure of Cellulose (Wang & Luo, 2016).

Through chemical digestion, the pulp mill industry produces large amounts of cellulose from solid wood. It has the advantage of being abundantly available from renewable sources, having a minimal carbon footprint, and being biodegradable. cellulose has exceptional chemical and physical qualities as an inexhaustible sustainable biopolymer that may be used for a wide range of applications (Thakur *et al*, 2017).

2.2.2 Hemicellulose

Hemicellulose makes up 10 % - 30 % of lignocellulosic biomass and has a molecular weight of less than 30000 g/mol. The primary function of hemicellulose in the biomass structure is to connect cellulose microfibrils and lignin. The hydrogen bonds and van der Waals force are responsible for the relationship between hemicellulose and cellulose. (Hornung, 2014). The length of a glycan chain is typically greater than the distance between two cellulose chains, allowing it to cover the cellulose surface and make hydrogen bonds with several cellulose chains. Furthermore, covalent bonds are used to connect hemicellulose with lignin (Basu, 2018; Wang *et al*, 2016b). Hemicellulose is made up of sugar chains that are short and highly branched. Hemicellulose is a polymer comprising five distinct sugars, unlike cellulose, which is a polymer of solely glucose. It's made up of five-carbon sugars (mostly d-xylose and l-arabinose), six-carbon sugars (d-galactose, d-glucose, and d-mannose), and uronic acid (Figure 2.4). Acetic acid has a high substitution rate for sugars. Hemicellulose's branching form gives it amorphous qualities that make it easier to hydrolyze to its constituent sugars than cellulose. When hardwood hemicellulose is hydrolyzed, it produces xylose-rich compounds (a pentose sugar) (Hornung, 2014).

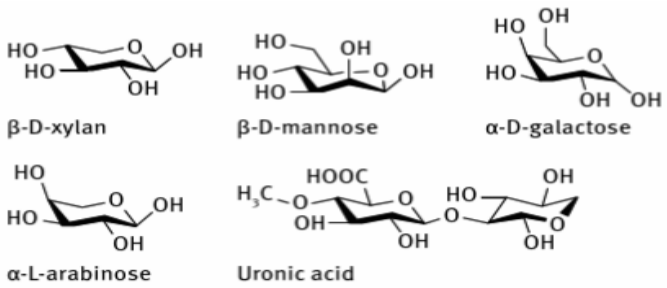

Figure 2. 4: Fundamental chemical structure of sugar units in hemicellulose (Wang & Luo, 2016).

2.2.3 Lignin

Lignin is the principal non-carbohydrate, polyphenolic structural component of wood 18 % - 30 % and other native plant matter that encrusts the cell wall structure and aids in bonding the cells intact. It is a highly polymeric molecule derived mostly from coniferyl alcohol ($C_{10}H_{12}O_3$), with a complex, cross-linked, highly aromatic structure and a molecular weight of approximately 10 000 mg/mol, by extensive condensation and polymerization (Hornung, 2014). Lignin has long been considered of as an unfavorable by-product that is typically incinerated for energy production. It is a key by-product of industry such as paper manufacturing and renewable biofuel production (Thakur *et al*, 2017).

Lignin is mostly composed of non-linear and random phenylpropanoid units. Figure 2.5 depicts three basic structures: hydroxy-phenyl lignin (H-lignin) polymerized by P-hydroxy phenylpropanoid units, guaiacyl lignin (G-lignin) polymerized by guaiacyl phenylpropanoid units, and syringyl lignin (S-lignin) polymerized by syringyl phenyl. Because lignin only has three fundamental structural units, different functional groups on the benzene rings contribute to the lignin structure's complexity.

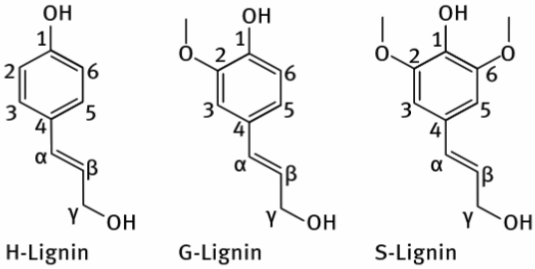

Figure 2. 5: Three basic structural units of lignin (Wang & Luo, 2016).

Table 2. 1: Composition of paper waste sludge (wt.%, db) (Brown *et al*, 2017)

Biomass	Cellulose	Hemicellulose	Lignin	Reference
Corrugated PWS	47.70	16.00	7.10	(Ridout *et al*, 2015)
Virgin pulp PWS	55.70	16.80	3.60	(Ridout *et al*, 2015)

2.2.4 Extractives and Ash

Secondary metabolism forms non-structural compounds called extractives in plants. These extractives are hydrophilic and lipophilic organic compounds that can be extracted by hot water or with the aid of organic solvents. There are 4-5 times more extractives in tree bark than in free wood. Which categorically add color, durability, odor and protect plants against predation (Manuel, 2010). Mineral materials found within the biomass matrix are composed mainly of metals, silica, phosphates, sulphates, and carbonates, these compounds act as catalysts for polycondensation reactions leading to char formation (Manuel, 2010).

2.3 Utilization of Paper Waste Sludge & Rejects

Rejects within a papermill production system are fibers (screening and clarification processes), plastics, metals and grit will vary amongst mills based on the feedstock used (Méndez *et al*, 2009), typical composition of these wastes is organic matter (cellulose fibers from recycled paper or wood including added organic compounds), inorganic compounds used as fillers and coatings (mainly calcium carbonate, kaolinite and talc) and water (Méndez *et al*, 2009; Monte *et al*, 2009). As regulations keep changing and becoming stricter when coming to waste management, the industry is also searching for better ways to manage and valorize their waste. This is driven by jurisdictions increasingly reducing and banning landfilling of organic wastes by legislating towards improving the efficiency of resource use and recycling (Faubert *et al*, 2016), the sustainability of industry going into the future is also heavily reliant on the management or valorization of waste into products that can be reintegrated into the economy. It is necessary to integrate different paper waste sludge management practices to deal with the volumes produced by mills (Faubert *et al*, 2016), more well understood environmentally friendly approaches are necessary to explore the valorization of paper waste sludge and rejected fiber.

There are various utilization options of paper waste sludge such as land application (Faubert *et al*, 2016), integration into materials (de Azevedo *et al*, 2019), energy recovery (Ridout *et al*, 2016), biochemical (Tawalbeh *et al*, 2021) and thermochemical (Brown, 2019) conversion.

2.3.1 Land application

Incorporation of organic matter into soil has been achieved by spreading paper waste sludge at the beginning and/or at the end of the crop growing season. The benefits of spreading on agricultural areas are well documented as this process improves soil fertility due to an increase in organic matter content (carbon), nutrient content (potassium, nitrogen, and phosphates), pH, cation exchange capabilities, aggregates, and water holding (Marche *et al*, 2003). Ultimately crop yield is improved (Faubert *et al*, 2016). However, there must be a strong consideration of the negative impact this method might have as there is potential water pollution through nutrient leaching, soil pollution, crop growth induced by heavy metals, and pathogens that cannot be overlooked (Wang *et al*, 2021).

2.3.2 Integration of paper waste sludge in materials

There are numerous options of using paper waste sludge as a material component which includes building materials, (de Azevedo *et al*, 2019) concluded that paper waste has sufficient characteristics to allow its incorporation into construction materials (cement and clay materials) with high CaO concentrations >50 %, in which the availability of calcite and a homogeneous distribution of particles indicated a potential increase in structural rigidity and other technological features.

2.3.3 Energy recovery

Paper waste sludge is a type of biomass that can be used in various energy recovery practices. Energy recovery can be direct like combustion to produce heat, microbiological production of biogas through anaerobic digestion, physicochemical processes leading to the production of biofuel and bioethanol from processes such as pyrolysis and fermentation (Faubert *et al*, 2016). The conversion of biomass into useful forms of energy is achieved using two distinct processes, namely: biochemical and thermochemical conversion (Brown, 2019; Ridout *et al*, 2016).

2.3.3.1 Biochemical conversion

Bacteria or enzymes break down large biomass molecules into smaller molecules in biochemical conversion, it is a process that is much slower than thermochemical conversion and requires a far less external energy input (Brown *et al*, 2017; Ridout *et al*, 2015). The three categories of biochemical conversion are:

Digestion (aerobic and anaerobic): In anaerobic digestion carbon dioxide, methane and a solid residue are the main products, the process entails an uptake of oxygen from the biomass by bacteria rather than ambient air (Veluchamy *et al*, 2018). In aerobic digestion, the breakdown of biomass occurs is carried out by bacteria that access oxygen from the air (Mussoline *et al*, 2013).

Fermentation: The conversion of biomass using enzymes and acids produce carbohydrates, which are further converted into ethanol or other chemicals with the help of yeast. This process doesn't convert lignin (Basu, 2018).

Enzymatic or acid hydrolysis: Breaking down of cellulose and hemicellulose in the presence of enzymes into fermentable sugars by bacteria and yeast (Basu, 2018), the final product is composed of a residue with few carbohydrates, and elevated amounts of lignin and ash (Brown *et al*, 2017)

2.3.4 Thermochemical conversion

Thermochemical conversion of biomass is characterized by three main processes, namely: Pyrolysis, gasification, and combustion. The three processes can be used to primarily produce energy in different forms. (Brown *et al*, 2017). This approach is characterized by the biomass pyrolytic treatment processes to produce gas, liquid and solid products that can be upgraded into synthetic biofuels. The reaction conditions determine the type of conversion method used to produce gas, liquid, and solid fuels intermediates. Thermochemical conversion is possible with all biomass (Pandey *et al*, 2015).

2.3.4.1 Thermochemical conversion of biomass

Biomass thermochemical conversion entails pyrolytic treatment of biomass to yield gaseous, liquid, and solid products that can be converted into fuels. (Basu, 2018). The heating rate, residence duration, temperature, and degree of oxidation all influence the final product distribution. (Brown, 2019) the various thermochemical conversion pathways and their products are detailed in Figure 2.6. and the operational parameters summarized in Table 2.2.

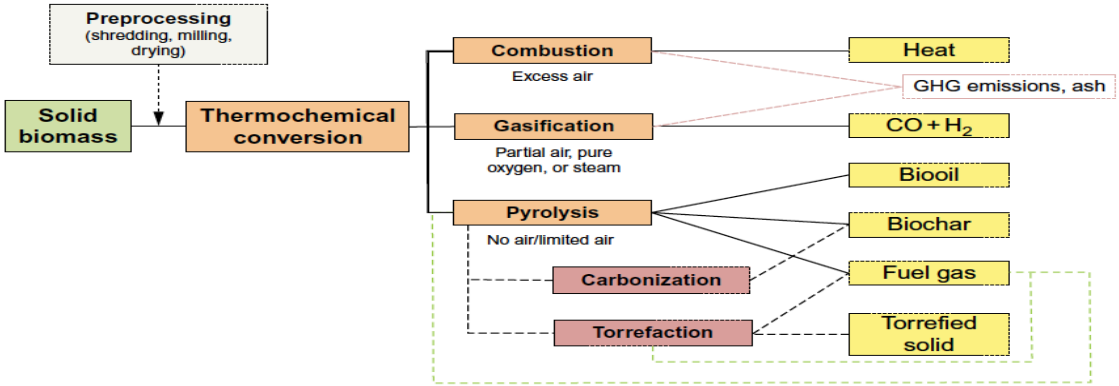

Figure 2. 6: Thermochemical conversion pathways and their products (Gent *et al*, 2017).

Table 2. 2: Operational parameters that govern each thermochemical conversion process.

Conversion process condition	Pyrolysis	Gasification	Combustion	Reference
Temperature(°C)	300-600	500-1300	700-1400	
Environment	No oxygen	Hydrogen, Steam	Air	(Basu, 2018)
Products	Solid char produced at low temperatures; liquid and gases at higher temperatures	High yield of hydrogen, carbon monoxide, carbon dioxide, methane, ethane, nitrogen, and water	Recoverable heat can be used to generate steam and produce electricity	(Basu, 2018)
Other factors	High quantity and quality of liquid and gas produced in a hydrogen atmosphere	Higher yield and quality of gas produced than with pyrolysis; costlier than pyrolysis	No synthetic fuel gas produced	(Basu, 2018)

2.3.5 Combustion

Combustion is a thermochemical reaction wherein biomass fuel is burnt in the presence of atmospheric air or only oxygen (Balaman, 2018). Combustion is an exothermic chemical

process in which a substance reacts rapidly with oxygen and gives off heat, from primitive open fires and cooking stoves to modern controlled furnaces. The process produces thermal energy in the range of 800 °C - 1600 °C suitable for heat and power purposes (Brown, 2019).

2.3.6 Gasification

Gasification is a thermochemical conversion process in which biomass is partially oxidized at high temperatures of 800 °C-1400 °C to produce syngas, a combustible mixture of carbon monoxide (CO), hydrogen (H_2), methane (CH_4), nitrogen (N), carbon dioxide (CO_2), and smaller amounts of hydrocarbons. (Balaman, 2018; Brown, 2019). The procedure can be done in either air or oxygen. The gasification process can be used to convert carbonaceous solids or liquids into gas mixtures with low molecular weight. Biomass may be gasified more easily than standard coal due to its high volatile content. (Brown, 2019). An important characteristic of biochar produced from gasification is that it contains polycyclic aromatic hydrocarbons (PAHs) which are toxic and limit the usage of biochar produced from gasification in environmental remediation applications (Ok *et al*, 2018). Gasification is dependent on the system deficiency of Oxygen in respect of the stoichiometric amount (Bhaskar *et al*, 2018). These conditions inhibit the completion of combustion reactions leading to CO and H_2 being the main products (Breeze, 2017). The conversion process requires the addition of an oxidant, usually steam, oxygen, or CO_2, at levels below the stoichiometric amount required for full conversion of the feedstock carbon content (Ciuta *et al*, 2017).

2.3.7 Pyrolysis

Pyrolysis is a thermal process in which organic material is degraded in an inert environment at temperatures ranging from 250 °C - 900 °C and held at a specified temperature known as the pyrolysis temperature, yielding value-added products such as charcoal, syngas, and bio-oil. (Basu, 2018). At specific temperatures, lignocellulosic biomass components (lignin, hemicellulose, and cellulose) go through processes like depolymerization, fragmentation, and cross-linking to generate distinct products during pyrolysis. (Yaashikaa *et al*, 2020). The process, composition, and fuel properties of the products are detailed in the following sections. The feedstock used is a big determinant of the quantity for biochar, oil, and gas together with heating rate and vapor residence times. Depending on how these parameters are manipulated pyrolysis can be classified into three sub-categories which are summarized in Table 2.3 below, namely torrefaction, slow pyrolysis or carbonization, and fast pyrolysis (Brown, 2019).

The process produces an energy-dense char when compared to the parent biomass with less dense liquid and gas products (Basu, 2018). The char remains in the reactor while condensable and non-condensable gases produced in the process are released from the reactor and cooled downstream in a condenser where the condensable gases are condensed into bio-oil while the non-condensable gases are released as syngas (Brown, 2019). The quantity of char produced decreases with an increase of pyrolysis temperature while ash and carbon content increase (Xiang *et al*, 2020).

Table 2. 3: Pyrolysis processes

Pyrolysis technique	Temperature (°C)	Residence time	Biochar yield (%)	Bio-oil yield (%)	Syngas production (%)	Reference (%)
Slow/ carbonization	300 - 800	> 1 hr	35 - 50	30	35	(Ok *et al*, 2018)
Fast	400 - 900	0.5 s -10.0 s	15 - 35	75	13	(Ok *et al*, 2018)
Flash/ gasification	600 - 1200	< 1 min	5 - 15	25-40	50-60	(Yaashikaa *et al*, 2020)

2.3.7.1 Fast pyrolysis

Fast pyrolysis is a thermal decomposition of biomass in an inert atmosphere at a temperature range of 400 °C - 900 °C to produce liquid bio-oil and smaller proportions of biochar and non-condensable gases (Brown, 2019). It is characterized by rapid heating of feedstocks and quenching usually in the order of seconds, primarily to produce bio-oil (Brown & Wang, 2014). The heating rate in fast pyrolysis can be high as 1000 °C - 10000 °C/s and the peak temperature must be below 650 °C whenever bio-oil is the desired final product (Basu, 2018; Wang *et al*, 2019a).

Fast pyrolysis produces bio-oil as the major product with a yield of up to 75 % and lesser amounts of biochar 12-15 wt.% and non-condensable gases at 13 - 25 wt.%. The gases are a flammable mixture of CO, CO_2 and light hydrocarbons which can be used for generating process heat. The main reactor configurations in fast pyrolysis are; bubbling fluidized-bed reactor, circulating fluidized-bed reactor, auger reactor (Wang *et al*, 2016a).

2.3.7.2 Slow pyrolysis

Slow pyrolysis is characterized by process conditions such as slow heating rates, relatively long solid & vapor residence time, and usually lower operating temperatures when compared to fast pyrolysis (Hornung, 2014). The process is widely used when biochar 35 wt.% -50 wt.% is the final product of interest. It also produces bio-oil 25 wt.% - 35 wt.% and gaseous product 25 wt.% - 35 wt.% (Pandey *et al*, 2019). Slow pyrolysis is broken down into two categories namely; torrefaction and carbonization where torrefaction is carried out at a lower and narrow temperature range 200 °C - 300 °C while carbonization has a higher and wider temperature range (Basu, 2018).The physicochemical properties of resultant char and the yield are dependent on the feedstock and operating conditions. These process conditions are similar to those in fast pyrolysis with the only difference being set values and times (Pandey *et al*, 2015). Pyrolysis oil and gaseous products formed during carbonization can be recycled and used as fuels in the thermal conversion process while the excess gas and pyrolysis oil can be recovered and used further in other applications (Gent *et al*, 2017). The recovered bio-oil and gaseous products can be processed into higher-value fuels such as bio-diesel or burned in the generation of heat or power. Biochar applications usage ranges from adsorption, renewable agricultural fertilizer, material for electrodes or production of carbon nanotubes, *etc*., (Strezov *et al*, 2007). The reactors used in slow pyrolysis are like those used in fast pyrolysis with the inclusion of a static batch reactor.

2.4 Pyrolytic degradation of lignocellulosic biomass

The process of biomass pyrolysis to produce biochar, bio-oil, and gas is comprised of the pyrolytic mechanisms of cellulose, hemicellulose, and lignin, these components of biomass have different thermal characteristics. Cellulose decomposes in the temperature range of 300 °C - 390 °C, hemicellulose at 200 °C - 320 °C, and lignin starts to decompose between 280 °C-500°C (Ok *et al*, 2018). During pyrolysis, primary reactions occur which include biochar formation, depolymerization, fragmentation, and further conversion of volatiles during secondary reactions (Ridout *et al*, 2016). Thermogravimetric analysis (TGA) is the technique of choice when analyzing the relationship between the weight change and reaction temperature of a sample on a thermal balance (Wang & Luo, 2016).

Degradation of lignocellulosic biomass components occurs in the temperature range of 200-500°C (Brown *et al*, 2017) Figure 2.7 illustrates the typical thermal behavior of paper waste sludge.

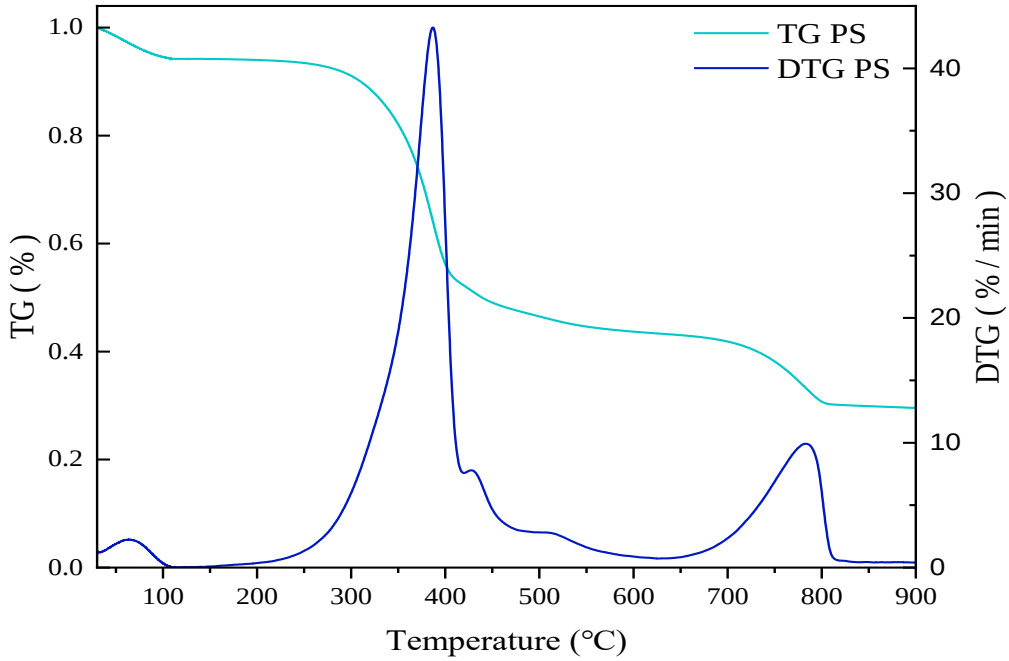

Figure 2. 7: Thermogravimetric curves (TG) and derivative thermal gravimetric curve of the lignocellulosic biomass components (Assis & Chirwa, 2021).

To understand the thermal behavior around the weight loss behavior of biomass components Fourier Transform Infrared Spectroscopy (FTIR) is performed to determine the chemical compounds in the sample, this also allows for a better understanding of the release of volatiles throughout the entire pyrolysis process and the distribution of functional groups can be determined (Wang *et al*, 2016a).

2.4.1 Pyrolysis of cellulose

Thermal degradation of cellulose generally occurs at 300 °C - 390 °C with a maximum loss rate at 320 °C - 350 °C (Brown *et al*, 2017). During the thermal decomposition of cellulose, a series of complex initial reactions involving dehydration, condensation, and depolymerization occur, resulting in the formation of active cellulose, an active intermediate product with simple components and low degrees of polymerization, which is followed by competing reactions to form final pyrolysis products (Wang & Luo, 2016). The process flow diagram is shown in Figure 2.8.

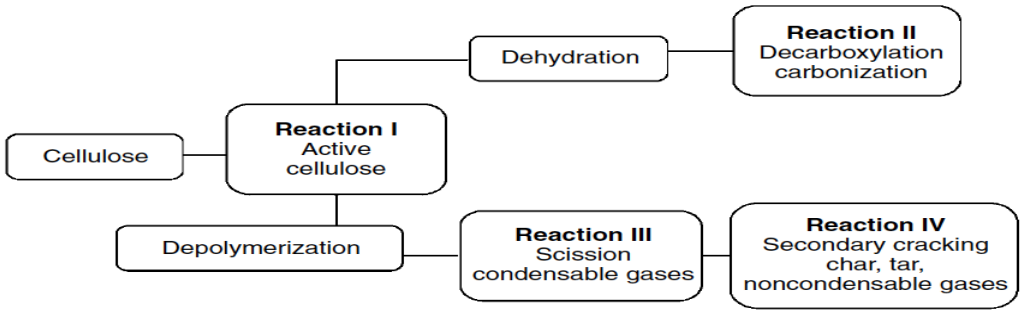

Figure 2. 8: Pyrolytic reactions of cellulose (Basu, 2018).

Reaction I: Two competing first-order reactions occur in an intermediate pre-reaction, this occurs at temperatures of about 100 °C.

Reaction II: These reactions involves dehydration, decarboxylation, and carbonization in sequential steps forming char, non-condensable gases like water vapor, CO_2, CO is more favourable at temperatures below 300 °C.

Reaction III: These reactions include depolymerization, scission of bonds, forming vapors including tar and condensable gases

Reaction IV: Condensable vapors that reside in the reactor for longer periods undergo secondary reactions such as cracking the vapor into secondary char, tar, and gases (Basu, 2018).

Cellulose pyrolysis is reported to be exothermic at low heating rates and has increased mass transfer limitations as char forms over bond scissions (Ridout *et al*, 2016). During volatilization of cellulose, laevoglucose develops which further undergoes dehydration simultaneously with char formation to produce hydroxymethyl furfural which can decompose further to form bio-oil and syngas. Hydroxymethyl furfural can further undergo reactions like aromatization, condensation, and polymerization to produce biochar again (Yaashikaa *et al*, 2020).

2.4.2 Pyrolysis of hemicellulose

Hemicellulose degradation occurs at a temperature range of 200 °C - 320 °C with the maximum rate of mass loss observed at ~270 °C as indicated in Figure 2.6 (Brown *et al*, 2017). The mechanism for decomposition of hemicellulose during pyrolysis is similar to that of cellulose, it produces more gas and less tar and char when compared to cellulose due to rapid volatilization which starts at a lower temperature.

It proceeds to further to form biochar and laevoglucose through a series of reactions such as decarboxylation, intramolecular rearrangement, depolymerization, and aromatization. These products further decompose to form bio-oil or syngas (Yaashikaa *et al*, 2020).

2.4.3 Pyrolysis of lignin

The lignin pyrolysis mechanism is more complex than that of cellulose and hemicellulose, where the dominant pathway to lignin pyrolysis is a free radical reaction (Ok *et al*, 2018). The degradation of lignin occurs over a broader temperature range of 280 ℃- 500 ℃ when compared to cellulose and hemicellulose with the maximum release rate occurring at 350 ℃ - 450 ℃ (Basu, 2018). The breakage of β-O-4 linkage in lignin results in the formation of free radicals which capture the protons of species with weak O-H or C-H bonds that leads to the formation of decomposed products like vanillin and creosol (Yaashikaa *et al*, 2020).

These products then blend with other molecules causing chain propagation (Ok *et al*, 2018).The lignin pyrolysis process results in the production of more char and aromatics than that of cellulose and hemicellulose, the yield of char is approximately 40 wt.% in a slow heating regime (Wang *et al*, 2016a). The liquid yield is approximately 35 wt.% which is characterized by aqueous components and tar. The phenols produced via cleavage of C-C linkages and its gaseous product yield is approximately 10 wt.% of the original mass (Basu, 2018).

2.5 Pyrolysis products

As discussed in previous sections, pyrolysis of biomass involves the breaking down of complex molecules into several small molecules, producing three products:

i. Solid (Biochar)
ii. Liquid (pyrolysis oil)
iii. Gas (Syngas)

Researchers such as (Brown *et al*, 2017; Nguyen *et al*, 2020; Ridout *et al*, 2016; Wang *et al*, 2021) have performed pyrolysis experiments with paper waste sludge as a feedstock and achieved varying char yields due to process characteristics.

2.5.1 Flue gas/ Syngas

Condensable and non-condensable vapors are the principal by-products of biomass degradation. The heavier molecules in condensable gases cause them to condense when cooled, improving the yield of pyrolysis liquid. The non-condensable gas mixture of lower molecular weight contain carbon dioxide (CO_2), carbon monoxide (CO), methane (CH_4), ethane (C_2H_6) and ethylene (C_2H_4) (Basu, 2018). This mixture of gases produced during the decomposition of biomass at elevated temperatures (800 °C - 1400 °C) is called syngas (Brown, 2019).

2.5.2 Pyrolysis oil

The liquid product of pyrolysis is known as bio-oil and it's a black tarry fluid that contains up to 20 % water that consists of mainly homologous phenolic compounds (Basu, 2018; Yaashikaa *et al*, 2020). It is a mixture of complex hydrocarbons with large amounts of oxygen and water and these hydrocarbons fall into the five broad categories of hydroxyaldehydes, hydroxyketones, sugars & dehydrosugars, carboxylic acids, and phenolic compounds (Basu, 2018). The quenching of pyrolysis products to minimize secondary reactions that can crack vapors is critical in ensuring high bio-oil yield during fast pyrolysis. It is extremely reactive leading to polymerization at ambient temperatures and these physicochemical properties of bio-oil render it unsuitable for use as a transportation fuel without upgrading. Catalytic cracking, hydro-processing, aqueous phase reforming, and fermentation are the processes that have been explored in the upgrading of bio-oil to produce transportation fuels from it (Brown & Wang, 2017)

2.5.3 Biochar

Biochar is a porous solid carbonaceous product of thermochemical decomposition of biomass in an inert environment (Yaashikaa *et al*, 2020), it is characterized by a large surface area and pores mainly the reason why it has a large number of uses aside from fuel such as chemical adsorption and carbon storage in the ground (Basu, 2018; Xiang *et al*, 2020), it continually is being recognized as a multifunctional material for environmental and agricultural applications (Chen *et al*, 2011).

The characteristics of biochar produced depend on the reaction parameters and characteristics of feedstock used, at higher pyrolysis temperatures the biochar quantity produced is reduced while the fixed carbon content is increased (Manya, 2012). It is generally characterized by a large surface area (200 m^2/g -1000 m^2/g), high porosity, and low density (Perez-Mercado *et al*, 2018). Biochar quality is defined by the internal surface area or Brunauer Emmet teller (BET), pH, cation exchange capacity and carbon recovery. These characteristics are influenced by the reaction temperature, type of biomass, and reaction time (Basu, 2018). Biochar has many multidisciplinary advantages, some of the known benefits include; adsorption of nutrients from wastewater, stable carbon storage, prevention of greenhouse gas emission due to biomass degradation, increasing available nutrients for plant growth, improve water retention in soils, reducing fertilizer use by prevention of nutrients leaching from the soil, reduction of methane and nitrous oxide from the soil, can be used as a solid fuel for heat generation and production of activated carbon (Xiang *et al*, 2020) (Hornung, 2014).

The low environmental and economic footprint of biochar presents an opportunity for its meaningful and successful utilization in water-related research projects. Its increasing usage in resource recovery from wastewater necessitates the proper understanding of its before and after use, biochar should be regarded as part of the recycling process rather than the material used for resource recovery (Yang *et al*, 2020). Although activated carbon and biochar are made from similar feedstocks and methods, biochar production is at a lower temperature and usually costs 86% lower than activated carbon (Almanassra. *et al*, 2021), it is important to note that magnetic biochar will cost slightly higher than normal biochar due the additional metal oxides used in its production (Chen *et al*, 2011).

Biochar is an attractive alternative in the treatment of wastewater to conventional treatment techniques like chemical precipitation, ion-exchange, adsorption, and membrane filtration which are costly and generate considerable amounts of waste, it has also attracted significant research interest for its application as a low cost, excellent stability, high porosity, environmentally friendly organic remediation medium (Ok *et al*, 2018). In large-scale wastewater treatment applications, its limitations are derived from its removal difficulty from processes, the recovery of biochar requires sedimentation and further handling (Xiang *et al*, 2020).

2.5.3.1 Magnetic biochar

Biochar loaded with magnetic metal oxides derived from metal salts is referred to as magnetic biochar (Xiang *et al*, 2020). It is generally produced by co-pyrolyzing biomass with metal chloride solutions (Yang *et al*, 2020). To negate the difficulty of removing biochar from process wastewater researchers such as (Chen *et al*, 2011) created magnetic biochar by combining iron oxide and biochar formation during pyrolysis primarily for removal of contaminants in wastewater, harnessing their magnetic properties for their easy removal by magnets for regeneration and reuse (Feng *et al*, 2021b). Activated carbon, zeolites, polymeric adsorbents, clay minerals, porous silica, and zeolites have all been used to remove nutrients from wastewater, with activated carbon having the most applications due to its high surface area, porous structure, and durability (Almanassra. *et al*, 2021). The shortcoming of activated carbon is that it has relatively weak (negative) surface charged groups, which results in poor adsorption of anions including phosphates (Miyazato *et al*, 2020), and during the activation process, acidic wastewater is generated which require further treatment while minerals like calcium carbonate are washed out reducing the adsorption capacity those minerals present (Wang *et al*, 2021).

(Godlewska *et al*, 2020) found that the adsorption capacity of biochar increased due to the increase of positive charge on the surface of biochar, however, it was also found that co-pyrolyzing biomass with magnetic precursors (iron oxides, natural iron ores, and transitional metal salts) produces biochar with the reduced surface area when compared to pristine biochar produced from the same feedstock without the magnetic precursor (Chen *et al*, 2011), typically Al, Fe, La, and Mg salts have been used in impregnation to improve adsorption capacity of negatively charged anions as illustrated by Figure 2.9. The introduction of magnetic precursors to biochar elevates the production costs. This has prompted other researchers to also focus on other waste streams like iron-containing biomass waste and sludge which contain iron to negate the addition of salts (Xiang *et al*, 2020). However this can significantly reduce magnetic separation of the resulting biochars due to low iron content in the feedstocks, it is important to ensure iron content is at least 8% to ensure magnetic separation (Wang *et al*, 2020a). Common magnetic biochar synthesis techniques as illustrated by Figure 2.9 are:

i. **Impregnation:** The feedstock is mixed with a magnetic precursor, this can be done before pyrolysis or after pyrolysis (Xiang *et al*, 2020)
ii. **Chemical co-precipitation:** The feedstock is mixed with a magnetic precursor and subsequently the pH is increased by the addition of an alkaline solution for surface precipitation of magnetic particles before pyrolysis (Xiang *et al*, 2020).
iii. **Bioaccumulation:** Spiked solutions are added to the biomass during its production, an example is irrigating with spiked solutions.
iv. **Co-pyrolysis:** Biomass is mixed with metal-rich natural materials and pyrolyzed (Almanassra. *et al*, 2021)

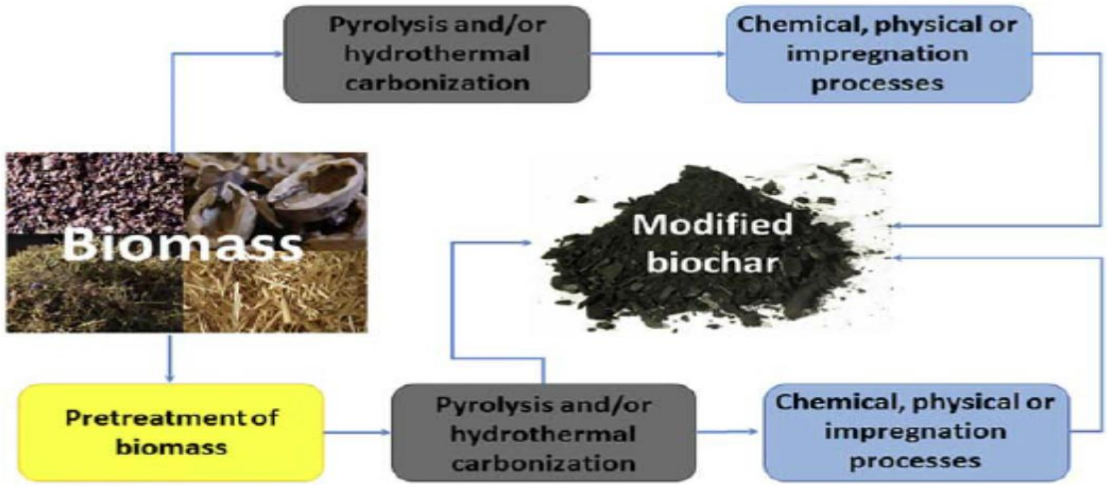

Figure 2. 9: Biochar modification processes (Ok *et al*, 2018).

Pyrolysis conditions play a major role during biochar synthesis, pyrolysis temperature's influence on iron-based magnetic biochar is of significance as the desired magnetic substance is dependent on it. The magnetic properties of biochar are significantly improved between 300 °C - 450 °C when Hematite Fe_2O_3 transforms into magnetite Fe_3O_4 (Wang *et al*, 2019b), however, should the temperature rise to approximately 1000 °C magnetite gradually converts to ferrous oxide and the magnetic properties are lost (Chen *et al*, 2019), these factors are important in selecting set pyrolysis temperature.

2.6 Adsorption

The adherence of atoms, ions, and molecules of gaseous, liquid, or dissolved solids to a surface is defined as adsorption (Naushad & Al-Othman, 2013). There are various adsorbents used in wastewater treatment that generally are of natural origin or engineered (Worch, 2012).

Although natural adsorbents are easily accessible and cost-effective, they are usually characterized by small surface area and porosity which result in lower adsorption capacity when compared with engineered adsorbents (Hernandez-Maldonado & Blaney, 2019). The adsorbents as per defined origins are shown in Table 2.4 below:

Table 2. 4: Common adsorbents

Adsorbent	Origin	Feedstock	Production Process	Capacity/ surface area	Structure	Source
Activated carbon	Engineered	Biomass/ plastic	Carbonization with chemical activation	High	Porous	(Hernandez-Maldonado & Blaney, 2019)
Biochar	Engineered	Biomass	Carbonization	High	Porous	
Adsorbent resin	Engineered	Styrene	Copolymerization	Moderate	Porous	(Worch, 2012)
Oxidic	Engineered	Hydroxides	Precipitation and partial dehydration	High	Crystalline	(Worch, 2012)
Synthetic Zeolites	Engineered	Zeolites	Hydrothermal conditions	Moderate	Crystalline	(Rida *et al*, 2013)
Natural	Natural	Clay, Ash etc.	Natural, Agricultural by-products	Low	Variable	(Rida *et al*, 2013)

Chemisorption and physisorption are two types of adsorption processes that are based on the strength of the adsorbate and adsorbent interaction. Chemisorption is defined by covalent bonds between both the adsorbent and adsorbent through either sharing or transferring electrons, whilst physisorption is described by weak electrostatic interactions like van der Waals, dipole-dipole, and London forces which are easily broken (Al-Ghouti & Da'ana, 2020).

2.6.1 Nutrients and adsorption

Eutrophication degrades the water resources and consequently is of great risk to local ecosystems within and nearby the affected water body (Yang *et al*, 2020). Phosphorus in water systems exists in different forms, total phosphorus, soluble phosphorus, and particulate phosphorus the common form is soluble orthophosphate. There are various methods available to remove phosphorus from wastewater such as precipitation (Christensen *et al*, 2021), biological nutrient removal (Liu *et al*, 2015), adsorption (Zhang *et al*, 2021b), and sludge-based (Fan *et al*, 2021) methods which require large spaces, large investment and high operations & maintenance costs (Wang *et al*, 2021).

Unique advantages are offered by adsorption because of the possible use of synthetic and natural feedstocks to achieve efficient pollutant removal (Han *et al*, 2019). The potential of biochar in resource recovery is a subject of intense research and its properties will continue to make it a sought-after alternative in wastewater treatment. As regulations become stricter towards the effluent discharge and waste management, environmentally benign and cost-effective solutions for recycling and resource recovery become a necessity (Yang *et al*, 2020). Human activities that produce effluent discharges disrupt the biochemical cycling of elements within nature (Ok *et al*, 2018; Yaashikaa *et al*, 2020), the primary inorganic species that cause ecotoxicological effects in natural environments are phosphates, nitrates, fluorides, heavy metals, hydrogen sulphite gas, and other greenhouse gases (Ok *et al*, 2018). In industrial wastewater applications, magnetic biochar has also demonstrated good results in the removal of methylene blue (Yao *et al*, 2020).

The mechanisms of adsorption are $\pi - \pi$ interaction, hydrophobic sorption, hydrogen bonding, electrostatic interaction, pore diffusion, surface complexation, and partitioning through functional groups (Ok *et al*, 2018). The presence of Mg, Ca, Fe, La, Si, Zn, Cu, Ce, Bi, Mn, or Al elements on the surface of biochar improves its uptake of nutrients more than the characteristic high surface area alone (Almanassra. *et al*, 2021). Iron oxide (FeO) has also shown good sorption capacity for anionic ions (Wang *et al*, 2019b). The presence of clays like kaolinite ($Al_2O_3 \cdot 2SiO_2 \cdot 2H_2O$) enhances the adsorption properties due to having been previously proven to have good adsorption capacity in the removal of heavy metals from wastewater (Gao & Goldfarb, 2021).

At temperatures above 450 °C during pyrolysis kaolin starts to undergo dihydroxylation and subsequently forms an amorphous aluminosilicate derivative called metakaolin ($Al_2O_3 \cdot 2SiO_2$) (Setthaya *et al*, 2017) as described by the equation below:

$$Al_2O_3 \cdot 2SiO_2 \cdot 2H_2O \rightarrow Al_2O_3 \cdot 2SiO_2 + 2H_2O\uparrow \qquad (2.1)$$

Magnetic biochar has a high affinity for phosphorus and thus a high efficiency in its removal from aqueous solution than pristine biochar due to higher surface area, increased reaction activity, and surface functional groups (Xiang *et al*, 2020; Yang *et al*, 2020).

The mechanism of adsorption is interconnected with the adsorption isotherms, kinetics, capacity, and adsorption thermodynamics (Almanassra. *et al*, 2021). Ion-exchange, surface deposition (weak bonds), and strong chemical bonds (ion exchange or precipitation) are the main mechanisms of phosphorus recovery from aqueous solution, with strong chemical bond being the dominant mechanism when biochar was used in the recovery process (Yang *et al*, 2020).

An important consideration is that since biochar is a carbon-based adsorbent with a negative surface charge in an aqueous solution, the electrostatic interaction of biochar and nutrients becomes heavily reliant on pH. In this case, the adsorption is promoted by the solution pH being lower than the point of zero charge (PZC) of the adsorbent (Almanassra *et al*, 2021). Repulsion occurs when the pH is higher than the PZC (Yang *et al*, 2020). This however is not absolute due to other interactions occurring at the same time. An ion-exchange has been recorded to be the iron oxide magnetic biochar adsorption mechanism of phosphate from wastewater (Almanassra *et al*, 2021), similar findings were made by other researchers that electrostatic interactions could not be identified during adsorption experiments (Chen *et al*, 2011).

Phosphate adsorption via ion exchange mechanism is reversible as the phosphate can be recovered from the biochar surface. Phosphorus plays an important role in agricultural production by increasing crop yields and product quality, it's recycling from wastewater is a good practice for resource recovery and pollution abatement (Yang *et al*, 2020). The recovery of phosphates from wastewater using biochar and its subsequent application to agricultural lands has dual benefits of soil quality improvement coupled with the slow release of the nutrients during irrigation (Almanassra *et al*, 2021) as the demand for fertilizers is increasing globally, recycling is always encouraged.

2.6.2 Adsorption of selenium

Selenium as an element is abundant on the earth's crust and it is an essential macro-nutrient when consumption is lower than 200 µg/day and also has the potential to be toxic at levels above 400 µg/day (Benis *et al*, 2022). Various selenium species are introduced to the environment by human activities and can pollute both surface and groundwater resources. Bioaccumulation of selenium species can cause damage to the receiving ecosystem and environment (Sinharoy & Lens, 2020). As with most necessary macro-nutrients for human and animal life, elevated levels of Selenium can present high levels of toxicity, the species selenate (SeO_4^{2-}) is characterized by mobility and high toxicity to organisms (Zhang *et al*, 2021a). Physiological problems such as selenium neurotoxicity and toxic effects on endocrine functions can be caused by consumption over 400µg/day of selenium (Lee *et al*, 2021).

Selenium exists in four oxidation states (i.e., elemental selenium (Se^0), selenite (SeO_3^{2-}), Selenide (Se^{2-}), and selenate (SeO_4^{2-})). Selenites and selenates are the most soluble forms and are widely found in aquatic systems. The World Health Organization (WHO) and the Department of Water & Sanitation, South Africa, have set the permissible limits of Selenium to 40µg/L and 20 µg/L respectively. Thus, as regulations become tighter, the need for economically sustainable solutions for the removal of selenium from wastewater is increasing. Selenium is also a by-product of production in industries such as mining, metallurgy and is widely used in electronics such as photocells, light meters, solar cells, and the glass industry (Hong *et al*, 2020). It is expected to see wider applications in the future as more and more solar cells will be manufactured as the world moves further towards green energy applications (Benis *et al*, 2022). Adsorption has been researched intensively and found to be the preferred choice for the removal of SeO_4^{2-} from the aqueous solution above conventional methods such as ion exchange, precipitation, biological treatments, and lime softening due to ease of design and operation and maintenance (Zhang *et al*, 2021a). In literature, there has been an increase interest in the use of adsorbents as a means to remove selenate from solution due to the low costs, abundant feedstocks, and low footprint. Iron oxide nano particles-based adsorbents are seeing an increased application in the removal of selenites and selenates (Lee *et al*, 2021). Therefore, magnetite composite containing biochars presents an opportunity to effectively adsorb selenium in an aqueous solution. The effect of calcium-containing feedstocks has not been intensively investigated.

2.6.3 Adsorption of methylene blue

Methylene blue is a widely used dye in the textile, leather, food, and packaging industries (Vedula & Yadav, 2022), in water systems high accumulated concentrations of methylene blue, can exhibit toxicity to the receiving environment, increased turbidity leading to reduced sunlight uptake by aquatic plants and ultimately threatening human health (Setthaya *et al*, 2017). Conventional wastewater treatment methods such as ion exchange, coagulation-flocculation, and biodegradation have proved to be inefficient due to high costs (Mu *et al*, 2022) thus the solid-liquid phase adsorption method is more desirable. The bio-refractory characteristics of dyes and chemical oxidation treatment methods can potentially produce degradation by-products that are more toxic than the original dyes. It is desirable to have *in-Sutu* treatment methods for the removal of dyes and adsorption is one of the methods that has produced high efficiencies in the removal of dyes from wastewater (Mubarak *et al*, 2015). Absorbents with high surface areas and minimal particle diffusion have led to high rate removal efficiencies of dyes from aqueous solutions (Mak & Chen, 2004).

2.7 Adsorption isotherms

Adsorption isotherms characterize the equilibrium performance of adsorbents at constant temperature, a phenomenon that is influenced by the adsorbed species, adsorbent, adsorbate, and other solution parameters such as pH, ionic strength, and temperature. (Al-Ghouti & Da'ana, 2020). The isotherms and corresponding equations characterize the adsorption process completely and thoroughly. An important factor is that the interface concentration should be in dynamic balance with the adsorbate concentration existing in the bulk solution (Al-Ghouti & Da'ana, 2020; Mozaffari Majd *et al*, 2021). According to the International Union of Pure and Applied Science (IUPAC), adsorption isotherms can be categorized into five types, depending on the isotherm shape of adsorbate-adsorbent pairs as indicated by Figure 2.11.

Type I adsorption is convex (upward) throughout the curve and is considered as favorable for adsorption, it can be described by the Langmuir equation (Alley, 2007). Type II is concave upward throughout the curve describes adsorption on mesoporous monolayer materials and multilayer at low and high pressure respectively, it is considered unfavorable for adsorption (Al-Ghouti & Da'ana, 2020). Type III is concave (upward) and occurs where the adsorbate-adsorbate interaction is big compared to adsorbate-adsorbent interactions.

A typical example is the adsorption of water on hydrophobic zeolites and activated carbon (Al-Ghouti & Da'ana, 2020). Type IV and V are also concave (upward) can exhibit hysteresis, a condition where desorption occurs along a different isotherm than adsorption, type IV has one inflection point while type V has several points (Al-Ghouti & Da'ana, 2020; Alley, 2007).

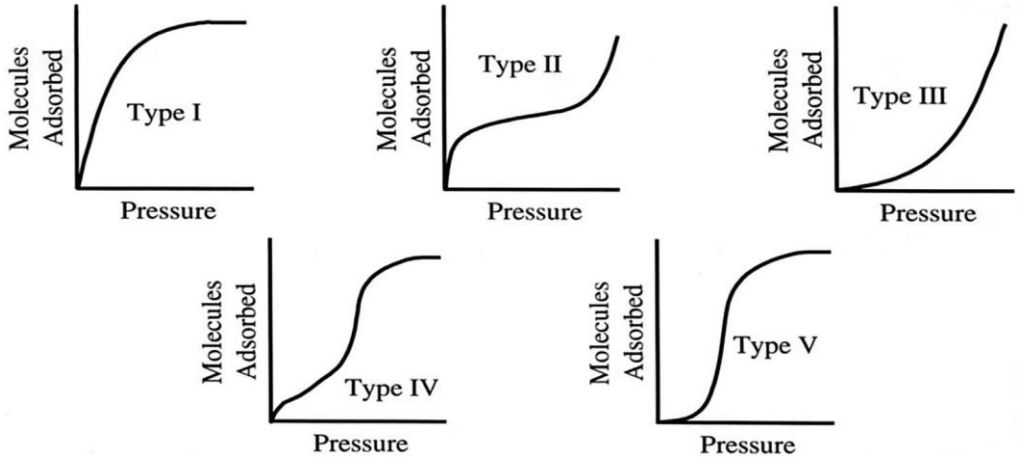

Figure 2. 10: Types of adsorption isotherms (Mohammed *et al*, 2020)

2.7.1 Langmuir isotherm model

Langmuir isotherm is one of the most widely used and applicable models for adsorption onto metal surfaces and particles and also forms a good basis for adsorption understanding, it treats the interaction between adsorbate and adsorbent as linear, revisable, monolayer chemical reaction (Al-Ghouti & Da'ana, 2020).

The model assumes that the adsorbent surface is completely homogenous to an extent that each adsorbent site can bind a maximum of one adsorbate molecule and that there are no interactions between adsorbate molecules (Alley, 2007). The model can be expressed mathematically in the following forms equation 2.2 for linear and equation 2.3 for non-linear. The adsorption nature is indicated by a separation factor (R_L) which is a dimensionless constant as represented by equation 2.4, and it can either be linear ($R_L = 1$), irreversible ($R_L = 0$), unfavorable ($R_L > 1$), or favorable ($0 < R_L < 1$).

$$\frac{C_e}{q_m} = \frac{1}{K_L\, q_m} + \frac{C_e}{q_m} \tag{2.2}$$

$$q_e = \frac{q_m K_L\, C_e}{1 + K_L\, C_e} \tag{2.3}$$

$$R_L = \frac{1}{1 + K_L\, C} \tag{2.4}$$

Where:

C_e = equilibrium concentration of adsorbate (mg/L)

q_e = equilibrium adsorption capacity (mg/g)

q_m = maximum adsorption capacity (mg/g)

K_L = Langmuir equilibrium constant (L/mg), also referred to as b

2.7.2 Freundlich isotherm model

The Freundlich isotherm model is a logarithmic model based on empirical data that seeks to account for the impacts of different adsorption energy levels. (Alley, 2007). Freundlich's model describes the reversible and non-ideal adsorption process and is not restricted to monolayer adsorption thus multilayer adsorption is applicable in its application (Al-Ghouti & Da'ana, 2020). The model can be expressed mathematically in the following forms equation 2.5 for linear and equation 2.6 for non-linear. For irreversible adsorption (1/n = 0), for favorable adsorption (0< 1/n < 1), unfavorable adsorption (1/n > 1) and for no adsorption (1/n →∞).

$$Inq_e = InK_F + \frac{1}{n} InC_e \quad (2.5)$$

$$q_e = K_F C_e^{1/n} \quad (2.6)$$

Where:

K_F = Freundlich equilibrium constant (L/g)

n = adsorption intensity

2.7.3 Sips isotherm model

To anticipate the heterogenicity of adsorption systems and to avoid the restrictions associated with the Freundlich model's increased adsorbate concentrations, a mixture of Langmuir and Freundlich isotherm models is utilized. At large concentrations, this results in the generation of an expression with a finite limit. It is useful for locating adsorption in the absence of adsorbate-adsorbate interactions. (Al-Ghouti & Da'ana, 2020). The model can be expressed mathematically in the following forms equation 2.7 for linear and equation 2.8 for non-linear

$$\beta_s In(C_e) = -In\left(\frac{K_s}{q_e}\right) + In(\alpha_s) \quad (2.7)$$

$$q_e = \frac{K_s C_e^{\beta} S}{1+\alpha_s C_e^{\beta} S} \quad (2.8)$$

2.8 Adsorption kinetics

Physical adsorption on porous adsorbents is used to remove organic molecules in multiple phases. Each of these factors has the potential to influence the overall rate at which contaminants are absorbed from solutions. (American Water Works & James, 2011):

- **Bulk solution transport:**
  When the adsorbate must be transferred from the bulk solution to the adsorbent particle boundary layer, diffusion is dominant at low mixing levels, whereas turbulence is dominating at high mixing levels (American Water Works & James, 2011).

- **External (film) resistance to transport:**
  Higher flow rates translate into shorter distances and contact times for adsorbates transported by molecular diffusion through the hydrodynamic boundary layer (water) that surrounds adsorbent particles when water flows past (American Water Works & James, 2011).

- **Internal interparticle transport:**
  Adsorbates must be delivered via the pores of the adsorbent to the active sites dispersed throughout the adsorbent after passing through the hydrodynamic boundary layer. Surface diffusion or pore diffusion may be used to transfer intraparticle

- **Adsorption:**
  After transport to available sites, an adsorption bond is formed between the adsorbate and the adsorbent.

The overall adsorption kinetics are affected by both the adsorbate molecular size and the adsorbent particle size; diffusion coefficients are inversely related to the molecular size to roughly one-third power.

Because size exclusion effects prevent larger molecules from accessing smaller pores, they must travel a shorter distance into the activated carbon particle to reach an adsorption site. Large molecules may so reach equilibrium faster than small molecules that must go further into the activated carbon particle, despite their lower diffusion coefficient. If intraparticle diffusion controls the rate of adsorbate uptake and the effective diffusion coefficient is constant, the time to reach adsorption equilibrium is proportional to the particle diameter squared (American Water Works & James, 2011).

MATERIALS AND METHODS

3.1 Materials

3.1.1 Source and feedstock preparation

Two variants of paper waste sludge were sourced from Mpact Springs Mill (South Africa), the rejected paper waste sludge (RPS) which is generated from the screening and high-density cleaning processes after pulping before the board machines and the secondary paper waste sludge (SPS) which is generated at the wastewater treatment (clarification) plant where the fiber is settled out and pressed for water recovery.

3.1.2 Chemicals

Analytical grade ferric chloride hexahydrate ($FeCl_3 \cdot 6H_2O$), ferrous chloride tetrahydrate ($FeCl_2 \cdot 4H_2O$), potassium dihydrogen orthophosphate (KH_2PO_4) and methylene blue ($C_{16}H_{18}ClN_3S \cdot_x H_2O$) were purchased from Glassworld (Johannesburg, South Africa), while sodium selenate (Na_2O_4Se) was purchased from Sigma Aldrich (Johannesburg, South Africa), all chemicals were and without further purification. Nylon syringe (filters 0.45 µm) were purchased from Anatech (Johannesburg, South Africa) and deionized water was produced from an Elga Veolia water purification system LA759.

3.1.3 Preparation of adsorbents and carbonization

The two variants of paper waste sludge underwent a natural drying process at approximately 27°C in a drying area at the Mill for 10 days. The samples were then milled, homogenized, filled into labelled ceramic pots with no space left, and sealed. For the preparation of magnetic biochar with magnetite nanoparticles serving as the magnetic medium, a 1000 mL solution of 1:1 molar ratio ferric chloride and ferrous chloride was prepared and mixed with 680 ± 2 g of each variant of sludge under rigorous mechanical stirring for 30 mins. The method was adapted from (Chen *et al*, 2011). Prior to carbonization, the samples were oven-dried at 110°C for 24 h. carbonization was performed in a muffle furnace under N_2 with a heating rate of 5°C/min and kept at the peak carbonization temperature of 450°C, 550°C and 650°C for 1 h.

The samples were then cooled to room temperature before being taken out, homogenized and denoted RPSX, SPSX, MBC-RPSX and MBC-SPSX with MBC denoting Magnetic biochar and X the corresponding carbonization temperature.

Biochar yields were calculated using equation 3.1:

$$\text{Biochar Yield} = \frac{\text{Mass of biochar}}{\text{Mass of PWS}} \times 100 \quad (3.1)$$

3.2 Physio-chemical characterization

3.2.1 Proximate analysis

Proximate analysis of both samples was performed using a Hitachi STA7300 TGA-DTA following the ASTM D7582–15 method, 1g of raw paper sludge (RPS) and secondary paper sludge (SPS) each was used. Experiments were carried out at atmospheric pressure and heating rates of 50 °C/min - 100 °C/min using ground samples; the temperature ranged from 50 °C - 950 °C. Nitrogen was used as an inert gas at a flow rate of 50 mL/min. The sample temperature was raised to 950 °C and held for 10 min then cooled from 950 °C - 600 °C under inert gas flow, increased to 750 °C where oxygen was introduced at a flow rate of 50 mL/min to combust the samples for fixed carbon during ash content determination.

3.2.2 Ultimate analysis

For ultimate analysis, 1.75 g -1.85 g of raw paper sludge (RPS) and secondary paper sludge (SPS) samples were weighed into a universal soft tin cup, folded into a barrel form, and deposited into an autosampler. Samples were fed into a quartz reactor in the instrument Furnace at 950 °C for flash combustion with the aid of oxygen using a Thermofisher Scientific Flash 2000 CHNS Elemental analyzer. The gaseous combustion products N_2, NO_x, H_2O, SO_2, O_2 and CO_2 were carried by helium through a column filled with copper oxide to a Cu-column where nitrogen oxides were reduced to elementary nitrogen (N), and O_2 to CuO. Water was be absorbed in another column. The remaining gasses were introduced into a Temperature Programmed Desorption (TPD) column where N_2 passes through it and other gases are bound to the column.

The gases are released individually when a temperature rise in the column is programmed. A thermal conductivity detector (TCD) and a gas flow create an electrical signal proportional to nitrogen, carbon, hydrogen, and Sulphur concentrations.

3.2.3 Fourier-transform infrared spectroscopy

A Perkin Elmer 100 Spectrophotometer was used to identify the principal functional groups and anions in the biochar. A MIRacle attenuated total reflection (ATR) attachment with a zinc-selenide (ZnSe) crystal plate was attached to the instrument. Prior to sample runs, the specimen holder's background data was acquired. The spectra were acquired across 32 scans and ranged from 500 cm^{-1} to 4000 cm^{-1} at a resolution of 2 cm^{-1}. After each spectrum was acquired, the crystal plate was cleaned with acetone.

3.2.4 X-ray diffraction

The samples were prepared with a standardized PANalytical loading system and investigated with Fe filtered Co-K radiation (λ=1.789Å) on a PANalytical X'Pert Pro powder diffractometer in - configuration with an X'Celerator detector and variable divergence- and fixed receiving slits. The mineralogy was determined using X'Pert Highscore plus software by selecting the best–fitting pattern from the ICSD database to the measured diffraction pattern.

3.2.5 X-Ray Fluorescence

To measure LOI, the samples were roasted at 1000 °C in alumina refractory crucibles (LOI). To generate a stable fused glass bead, 1 g material was combined with 6 g Lithiumteraborate flux and fused at 1050 °C. The paper waste sample was ashed and pressed to 10 tons as a boric acid-pressed powder. The investigations were carried out utilizing a Thermo Fisher ARL Perform'X Sequential XRF equipment and Uniquant software from Thermo Fisher. The software looked for all elements between Na and U in the periodic table, but only those detected above the detection thresholds were reported. To determine crystal water and oxidation state changes, the results were standardized to incorporate LOI. The standard sample material was prepared and tested in the same way as the samples, and the results were reported as such.

3.2.6 Brunauer-Emmett-Teller

BET analysis was performed using a Micrometrics Tri-Star II surface area and porosity instrument. The instrument has a separate degassing system (Micrometrics VacPrep 061 sample degas system) which consists of a vacuum system, a heating set-up, a pressure gauge as well as a cooling set-up. The samples were required to be dry and pure, mass measurements were taken before and after degassing as well as after the analysis. Glass tubes are used to hold the samples. The degassing was done at 110 °C for approximately 8 h under vacuum. For the analysis, a glass rod was inserted into the sample holder to reduce the dead volume of the tube. An isothermal jacket was used to cover the glass tubes. Liquid nitrogen was used for the analysis.

3.2.7 Scanning electron microscopy

Scanning electron microscopy was used to examine the morphology of the paper waste sludge and biochar samples (SEM). A Zeiss Crossbeam 540 FEG scanning electron microscope was used to create the images. SEM samples were prepared by dispersing the samples on a carbon tape adhered to a microscope stub, and then sputter-coating the samples with carbon under argon gas using a SEM auto-coating equipment E2500 (Polaron Equipment Ltd). Micrographs were taken at a voltage of 2 kV.

3.2.8 Scanning electron microscopy and energy dispersive x-ray spectroscopy

SEM was used to analyze the elements in the paper waste sludge and biochar samples. A Zeiss Ultra PLUS FEG scanning electron microscope with an Oxford instruments detector and Aztec 3.0 SP1 software was used to create the images. Samples were prepared by distributing them on a carbon tape adhered to a microscope stub, and then sputter-coating them with carbon under argon gas using a SEM auto-coating equipment E2500 (Polaron Equipment Ltd). The spectra were recorded at a voltage of 15 kV.

3.2.9 Transmission electron microscopy

Samples were dispersed in ethanol in a 3 ml sample vial and the mixture was sonicated for about 10 min to disperse the particles within the mixture before the morphology and structure of the paper waste sludge and biochar samples was captured using a TEM on a JOEL JEM 2100F TEM.

3.3 Adsorption studies

3.3.1 Design

Studies were designed to investigate the biochar adsorption efficiency of Phosphate, Selenium, and Methylene blue. The effect of carbonization temperature (450 °C, 550 °C, and 650 °C), biochar loading (2.5 g/L, 5 g/L, 10 g/L, and 20 g/L), pH (5,7 and 9), and concentration were investigated in triplicate tests and average results reported during a series of batch experiments. Solutions of sodium selenate (Na_2O_4Se), potassium dihydrogen orthophosphate (KH_2PO_4), and methylene blue ($C_{16}H_{18}ClN_3S{\cdot}_xH_2O$) were prepared by adding known concentrations of each adsorbate to deionized water and stirred for 30 min with a magnetic stirrer. The pH of solutions was adjusted dropwise with 0.1 mol solutions of hydrochloric acid (HCL) and sodium hydroxide (NaOH) to 5, 7, and 9 respectively. 100 mL of each solution were added into 200 mL Schott bottles.

3.3.2 The effect of carbonization temperature

To assess the effect of carbonization temperature on adsorption efficiencies standard samples containing 1 g of each biochar variant was mixed with 100 ml of 183 mg/L synthetic selenate solution in 200 ml Schott bottles with lids. The suspensions were shaken continuously on a platform shaker operating at 25 °C and 150 rpm for 72 h with grab samples collected every 24 h. The suspension was centrifuged at 9000 rpm for 10 min; and the supernatant was further filtered through 0.45 µm cellulose nylon membrane filters, sealed in labelled sample bottles and placed in a cold store for analysis the next day using an ICP-OES. The same steps were followed when determining efficiencies for phosphorus using a 110 mg/L solution and 20 mg/L of methylene blue solution. Adsorption efficiencies were determined using Equations 3.2-3.3 (Alley, 2007).

$$q_e = \left(\frac{C_i - C_e}{m}\right) V \quad (3.2)$$

$$q_t = \left(\frac{C_i - C_e}{m}\right) V \quad (3.3)$$

Where:

q_e = adsorption capacity of the biochar (mg/g).

C_i = Initial solution concentration (mg/L)

C_e = Solution concentration at time t (mg/L)

m = Mass of adsorbent (g)

V = Solution volume (L)

3.3.3 The effect of adsorbent loading

Having established the best economical performing biochar and optimum carbonization temperature, a performance variability assessment of the optimum loading was determined by evaluating loading regimes of 2.5g/L, 5g/L, 10g/L, and 20g/L. The synthetic solutions used were of the same concentration is in 3.3.1.1, they were further mixed with biochar of 2.5g, 5 g, 10g, and 20g in 200mL Schott bottles with lids and placed on a platform shaker operating at 25°C and 150 rpm for 24 h. The suspension was centrifuged at 9000 rpm for 10 min; and the supernatant was further filtered through 0.45µm cellulose nylon membrane filters, sealed in labelled sample bottles, and placed in a cold store for analysis the next day using an ICP-OES for Se and P while a UV spectrophotometer was used for MB. ideally changing the loading regimes was to assess an increase in adsorption sites. The efficiencies were also calculated using Equation 3.3 (Alley, 2007).

3.3.4 The effect of pH and contact time

To assess the solution pH effect, the synthetic solutions of selenium, orthophosphate, and MB were adjusted to pH of 5, 7, and 9 using 0.1 M solutions of HCL and NaOH. 200 mL of each pH adjusted synthetic solution was mixed with 2g of the selected biochar in Schott bottles with lids and placed on a platform shaker operating at 25 °C and 150 rpm for 24 h. To analyze the effect of contact time, grab samples were collected at 0.5 h, 1 h, 2 h, 4 h, 8 h, 12 h, 16 h, and 24 h.

The suspensions were centrifuged at 9000 rpm for 10 min; and the supernatant was further filtered through 0.45 µm cellulose nylon membrane filters, sealed in labelled sample bottles,

and placed in a cold store for analysis the next day using an ICP-OES (Se & P) and a UV spectrophotometer (MB).

3.3.5 The effect of competition for sites

To assess the effect of competition for sites, synthetic solutions of 110 mg/L-P, 183 mg/L-Se and 20 mg/L-MB were prepared and mixed in a 300 mL Schott bottle with a lid with 3 g of the selected biochars. The suspensions were placed on a platform shaker operating at 25 °C and 150 rpm for 24 h. The suspension was centrifuged at 9000 rpm for 10 min; and the supernatant was further filtered through 0.45 µm cellulose nylon membrane filters, sealed in labelled sample bottles, and placed in a cold store for analysis the next day using an ICP-OES for Se and P while a UV spectrophotometer was used for MB.

3.3.6 Determination of adsorption mechanism

To determine the adsorption mechanisms of selected biochars, all experiments were conducted at determining optimum conditions and loading as per sections 3.3.1.1 to 3.3.1.3. Grab samples of the solutions were collected at intervals of 0.5 h, 1 h, 2 h, 4 h, 8 h, 12 h, 16 h and 24 h, and the spent biochar was collected at 24 h. The spent biochar was analyzed using XRF to determine the available oxides, XRD for the spent biochar phase purity, SEM for the morphology, and EDS for elemental mapping.

3.3.7 Determination of Adsorption Isotherms

The pollutants concentration effect was determined by varying the synthetic pollutant concentrations to assess the robustness of the biochar in variable conditions as follows:

Selenium:	92 mg/L, 183 mg/L, 276 mg/L and 367 mg/L
Orthophosphate:	50 mg/L, 110 mg/L, 160 mg/L and 220 mg/L
Methylene Blue:	10 mg/L, 20 mg/L, 25 mg/L and 30 mg/L

All experiments were conducted at pH 5, pH 7, and pH 9, adsorption capacities were calculated using Equation 3.4 (Sun *et al*, 2015) and fitted to the Langmuir, Freundlich, and Sips isotherm models.

$$q_e = \left(\frac{C_i - C_e}{m}\right) V \quad (3.4)$$

Where:

q_e = Solution equilibrium concentration (mg/g).

C_i = Initial solution concentration (mg/L)

C_e = Solution concentration at time t (mg/L)

m = Mass of adsorbent (g)

V = Solution volume (L)

3.3.8 Determining of Reusability and Regeneration Potential of Biochars

To determine the reusability and regeneration of selected biochars, 100 mL synthetic solutions of 110 mg/L-P, 183 mg/L-Se, and 20 mg/L-MB were prepared and individually mixed in 200-ml Schott bottles, with 1g of the selected biochars. After 24h the samples were centrifuged at 9000 rpm for 10 mins, the supernatant was collected into labelled bottles and stored in a cold store for analysis with ICP-OES and UV Spectrophotometer. The spent biochars were then dried overnight at 110°C in an oven, the dried biochars were then re-carbonized at 450 °C under N_2 purge for 1 hr then cooled. The adsorption tests were repeated using the spent biochars and all succeeding steps were repeated.

3.3.9 Modelling of Adsorption Kinetics

After determination of optimum conditions and loading, adsorption tests were conducted under the same conditions. Samples were collected in 15 min intervals for 1 h, after which they were collected on an hourly basis for 24 h to investigate the kinetics. The kinetics was evaluated at pH 5, 7 and 9 at 25 °C.

For pseudo first-order kinetic model, the following Equation was applied:

$$\frac{dq}{dt} = K_1(q_e - q_t) \quad (3.5)$$

$$ln(q_e - q_t) = ln\, q_e - K_1 t \quad (3.6)$$

Where:

K_1 = Lagergren rate constant (1/min)

t = time (min)

For the pseudo second-order kinetic model, the following equations 3.7 and 3.8 were applied:

$$\frac{dq}{dt} = K_2(q_e - q_t)^2 \quad (3.7)$$

$$\frac{1}{qt} = \frac{q}{K_2 q_e^2}\left(\frac{1}{t}\right) + \frac{1}{q_e} \quad (3.8)$$

Where:

K_2 = pseudo-second order rate constant (g/mg.min)

CHARACTERISATION

4.1 Biochar yields

Carbonization temperature has a significant effect on biochar yield (Basu, 2018). This is evident as biochar yield decreased as the temperature was increased. At higher temperatures, the release of volatiles is higher and thus the reduction in char yields, the yields of raw paper sludge and secondary paper sludge are shown in Table 4.1. The highest yield was observed at 450 °C, lower yield in RPS results indicates higher volatile matter content than SPS. With an average mass loss of 70.58 wt.% when compared with SPS which averaged 53.64 wt.%. The results followed the same mass loss trend even with the impregnated samples with RPS 69.34 wt.% when compared with SPS 52.81 wt.%, which is consistent with the raw samples.

Table 4. 1: Biochar yields

Sample Name	450°C (wt.%, d.b)	550 °C (wt.%, d.b)	650 °C (wt.%, d.b)
SPS	51.63	45.65	41.78
RPS	41.11	25.20	21.93
MBC-SPS	53.62	46.89	41.04
MBC-RPS	42.94	26.54	22.50

4.2 Physicochemical characterization

4.2.1 Proximate analysis and ultimate analysis

A thermogravimetric study (TGA) was performed to analyze mass loss in both RPS and SPS samples as illustrated by the thermal degradation profile in Figure 4.1. Fiber degradation occurs in the region of 200 °C - 500 °C and plastics in the region of 400 °C - 500 °C with (>90 %) volatiles release (Singh *et al*, 2019) (Ridout *et al*, 2016). Proximate analysis was conducted to determine the moisture content, volatile matter, fixed carbon, and ash content. The results as per Figure 4.1 indicate the loss of moisture to occur in the region of ≤ 100 °C due to evaporation.

The derivative thermogravimetric (dTG) curves comprised of one main peak occurring between 250 °C and 420 °C with an average mass loss of 54.47 wt.% SPS and 73.53 wt.% RPS

which is characteristic of fiber decomposition and consistent with previous findings by (Brown *et al*, 2017; Ridout *et al*, 2016). It is observed that volatile matter decreases with a temperature increase in the range of 400 °C - 700 °C while fixed carbon increases (Devi & Saroha, 2015). The lag on the SPS dTG curve at 420 °C - 450 °C can be attributed to the degradation of Kaolin used as a filler with the continued release of volatiles (Souza *et al*, 2019). The complete decomposition of calcium carbonate ($CaCO_3$) occurs at the second peaks between 700 °C - 810 °C, this is consistent with reported literature. During the degradation of ($CaCO_3$) the wt.% loss of RPS is 11 % and SPS is 30 % consistent with ± 30 wt.% reported in the literature (Wang *et al*, 2021). Results are summarized in Table 4.2.

Table 4. 2: Proximate and Ultimate analysis results

Sample Name	Moisture	Volatile Matter	Fixed Carbon	Ash	C	H	O	N	S
RPS	12.67	73.53	9.31	4.69	46.06	5.84	47.91	0.06	0.13
SPS	5.44	54.47	5.82	34.51	41.06	4.41	54.17	0.24	0.12

For ultimate analysis, the results of elemental analysis results of the two biochar variants shown in Table 4.2 above, indicate carbon and oxygen are the major elements within the paper sludge matrix. Based on these results, it was observed that the physical changes occur in the region of 300 °C -700 °C, therefore it was decided to carbonize RPWS within the same temperature range.

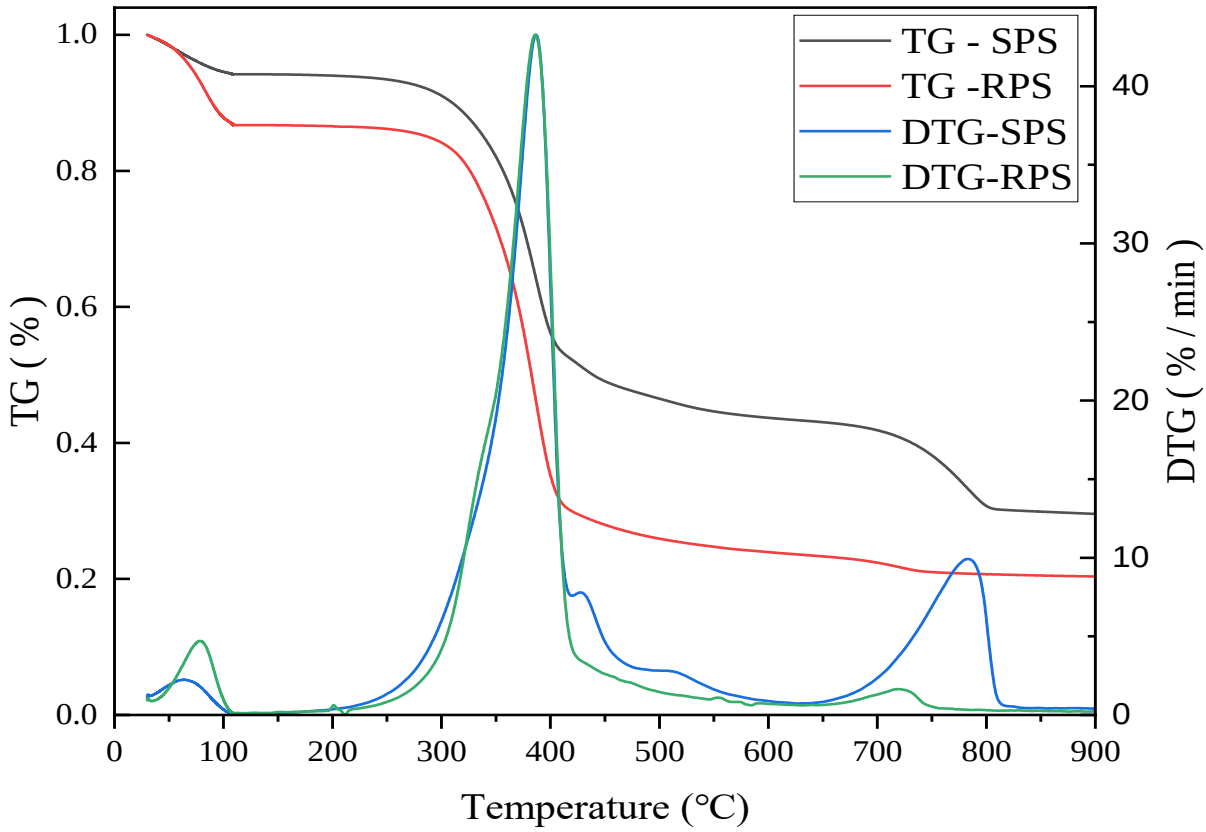

Figure 4. 1: Thermogravimetric (TG) and differential thermogravimetric (dTG) curves of SPS and RPS.X-ray diffraction

The feedstock and resultant biochar's structure and phase purity were analyzed by X-ray diffraction as shown in Figure 4.2 and appendix A. The results indicate that both the feedstock and biochar are amorphous characteristics of cellulose. The feedstock contains coating agents and fillers such as kaolinite, titanium dioxide, and calcium carbonite with kaolinite peaks at 2θ of 14º -14.5º and 2θ of 26º -29º, the peaks disappear after 400 ºC due to the decomposition of kaolinite into amorphous metakaolinite (Varga, 2007). Titanium dioxide is also used as a coating agent in recycled fiber mills, this is due to an observation of peaks at 2θ of 32º, and 65º it also observed that at carbonization temperatures above 550º C anatase is converted to more stable rutile which is also aided by the addition of Fe^{3+} during biochar synthesis (Loan *et al*, 2021). Calcium carbonate peaks were observed at 2θ of 34º, 46º, and 50.5 -52.5º with their intensity increasing with carbonization temperature, as a result of the formation of CaO during partial decomposition (Wang *et al*, 2021). However, for the magnetized biochar spectra, the peeks almost disappear due to the formation of $CaCl_3$ which is amorphous during the magnetization process. In recycled board mills. Talc is also used as an agent to smooth paper surfaces and the peak observed at 11º and 43º of talc is indicative of its use in the sample mill (Claverie *et al*, 2018).

The sharp strong peaks observed at 2θ of 35º, 42º, 51º, 66 º and 75º indicate well-crystalized magnetite on the surface of the impregnated biochar (Mohammadi *et al*, 2021) confirming the successful magnetization of RPWS biochar.

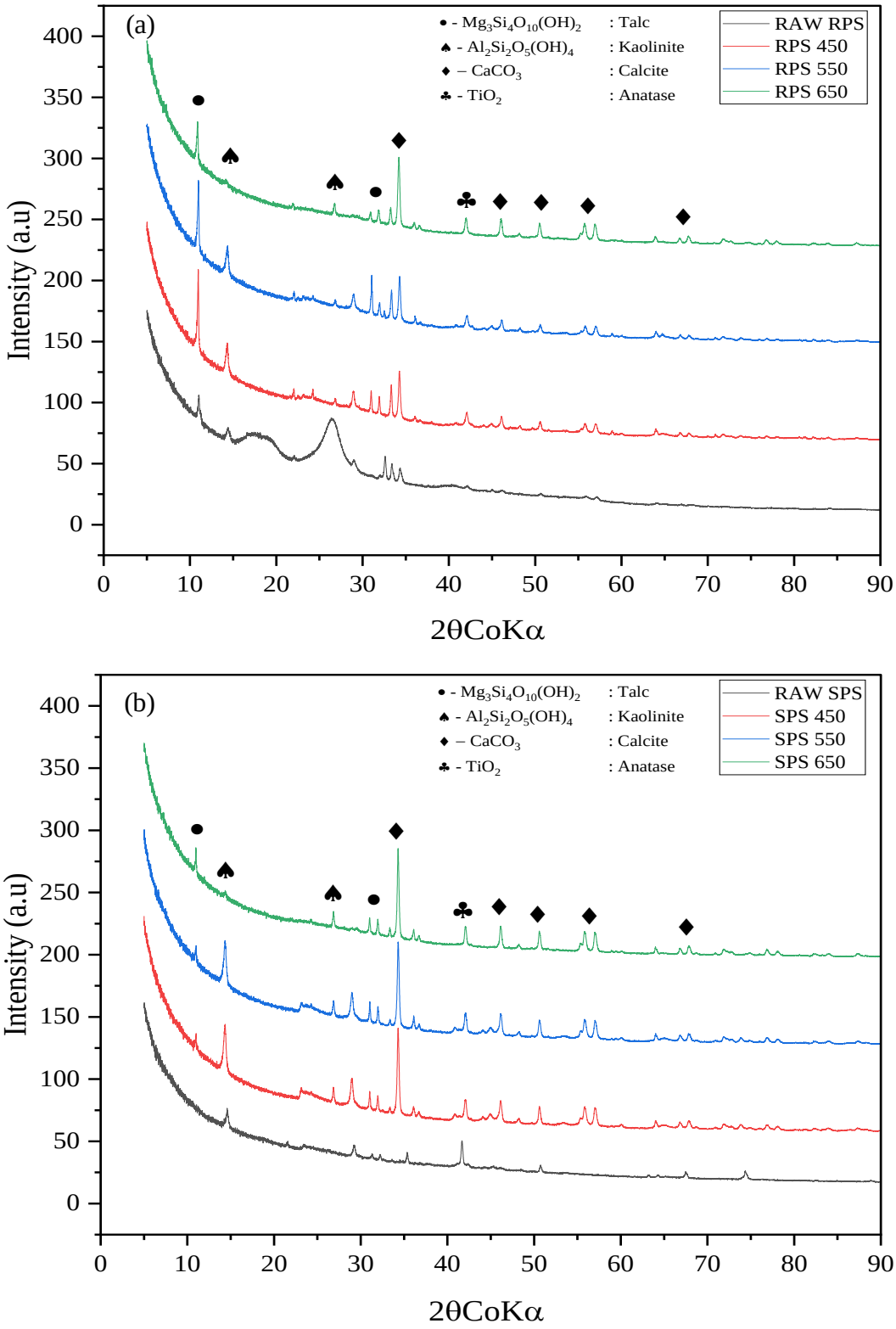

Figure 4. 2: XRD patterns for (a) RPS and (b) MBC SPS

4.2.2 X-ray fluorescence

The elemental composition of RPWS and both pristine and synthesized biochars were analyzed and reported in Table 4.3. The XRF results indicated the presence of clay and calcium carbonate in the feedstocks and subsequent biochars. This is primarily due to the usage of fillers and coating agents such as kaolin ($AlSi_2O_5[OH]_4$), titanium dioxide (TiO_2), and calcium carbonate ($CaCO_3$). During the production of the recycled board. It is evident that kaolin is the most used filler followed by calcium carbonate and to a lesser degree titanium dioxide and talc, findings similar to (Bundy & Ishley, 1991). It is observed that CaO wt.% is significantly reduced in the synthesized biochar 44 wt.% in RPS and 80 wt.% in SPS, the introduction of aqueous Ferrous and ferric chloride resulted in the formation of $CaCl_3$ thus the reduction in CaO. This observation is supported by the results of EDS section below in 4.2.7. The increased Fe_2O_3 is indicative of successful magnetization of biochars iron in the material is likely to undergo the following transformation:

$$FeCl_3 \rightarrow Fe(OH)_3 \rightarrow FeO(OH) \rightarrow 2Fe_3O_4$$

With H_2O, CO_2 and HCL are released as gases when temperatures increased (Li *et al*, 2016a)

Table 4. 3: Raw sample and biochar XRF results

Sample	SiO_2	Al_2O_3	MgO	Na_2O	Fe_2O_3	TiO_2	CaO	P_2O_5	SO_3	K_2O	LOI	Total
SPS	13.39	6.18	2.60	0.19	0.56	1.11	6.76	0.10	0.02	0.02	69.05	99.98
RPS	13.59	6.24	2.56	0.09	0.55	1.13	6.98	0.11	0.01	0.03	68.69	99.98
RPS 450	13.39	6.18	2.60	0.19	0.56	1.11	6.76	0.10	0.02	0.02	69.05	99.98
RPS 550	13.59	6.24	2.56	0.09	0.55	1.13	6.98	0.11	0.01	0.03	68.69	99.98
RPS 650	17.58	12.04	2.11	0.13	0.67	1.57	13.41	0.15	0.04	0.15	52.07	99.92
MBC-RPS 450	5.62	2.40	1.07	0.02	19.20	0.58	2.10	0.05	0.01	0.02	68.90	99.965
MBC-RPS 550	7.04	2.94	1.32	0.15	19.68	0.73	2.17	0.06	0.00	0.04	65.86	99.99
MBC-RPS 650	7.76	3.26	1.47	0.24	26.91	0.89	2.46	0.07	0.00	0.06	56.81	99.93
SPS 450	17.84	14.63	1.31	0.07	0.66	1.63	16.01	0.17	0.15	0.06	47.38	99.91
SPS 550	18.03	14.78	1.36	0.10	0.66	1.66	16.17	0.16	0.13	0.06	46.88	99.99
SPS 650	19.18	15.30	1.53	0.10	0.76	1.79	16.55	0.17	0.04	0.76	43.80	99.98
MBC-SPS 450	14.07	11.50	1.00	0.00	12.14	1.35	12.63	0.14	0.04	0.00	47.12	99.99
MBC-SPS 550	11.94	9.62	0.83	0.00	14.64	1.16	9.92	0.11	0.08	0.00	51.61	99.91
MBC-SPS 650	12.14	9.79	0.90	0.07	12.46	1.15	11.10	0.11	0.04	0.01	52.19	99.96

4.2.3 Fourier transform infrared spectroscopy

Fourier-transform infrared spectroscopy (FTIR) was carried out on the raw, pristine and synthesized biochar. Figure 4.3and appendix B shows the spectra of RPS, SPS, MBC-RPS, and MBC- SPS which are typical of cellulose structure (Méndez *et al*, 2009). Magnetic biochar exhibits similar bands with the loss of some peaks, Calcium carbonate presence is associated with both narrow 870 cm^{-1} and wide 1,410 cm^{-1} peaks. The peaks disappear in the impregnated MBC-denoted biochars due to the dissolution of $CaCO_3$ and the formation of calcium chloride $CaCl_3$ during the impregnation of raw samples (Xu *et al*, 2021).

The wideband at 3400 cm^{-1} is associated with stretching of the hydroxyl (-OH) functional group due to water molecule adsorption and or structural hydroxyl groups of organics contained in RPWS (Wang *et al*, 2021). The peaks lose their intensity due to the loss of (-OH) group during dehydration and organics carbonation as the temperature was raised (Devi & Saroha, 2015). The band at 2800 cm^{-1} - 300 cm^{-1} is associated with the asymmetric stretching of the aliphatic functional group (C-H). The band at 1,600 cm^{-1} is attributed to kaolinite in the samples which is converted to metakaolinite as carbonization temperature increased beyond 400°C (Varga, 2007).

Similarly, the bands at 1300 cm^{-1} -1700 cm^{-1} are associated with amines (CH_x) functional groups in RPWS. As the carbonization temperature increased, the peak between 950 cm^{-1} - 1110 cm^{-1} representing the stretching vibration of the C-O-C group reduced (Wang *et al*, 2020b). The bands at 1430 cm^{-1}, 910 cm^{-1} and 880 cm^{-1} are associated with $CaCO_3$ which decreased gradually with temperature increase due to partial decomposition and the formation of CaO (Wang *et al*, 2021).

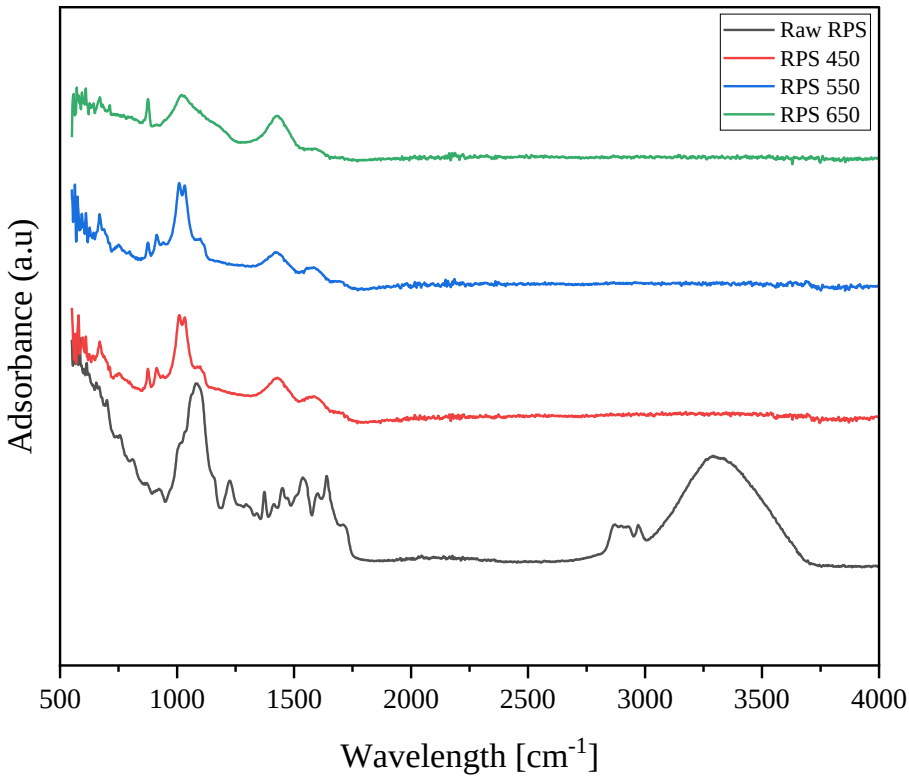

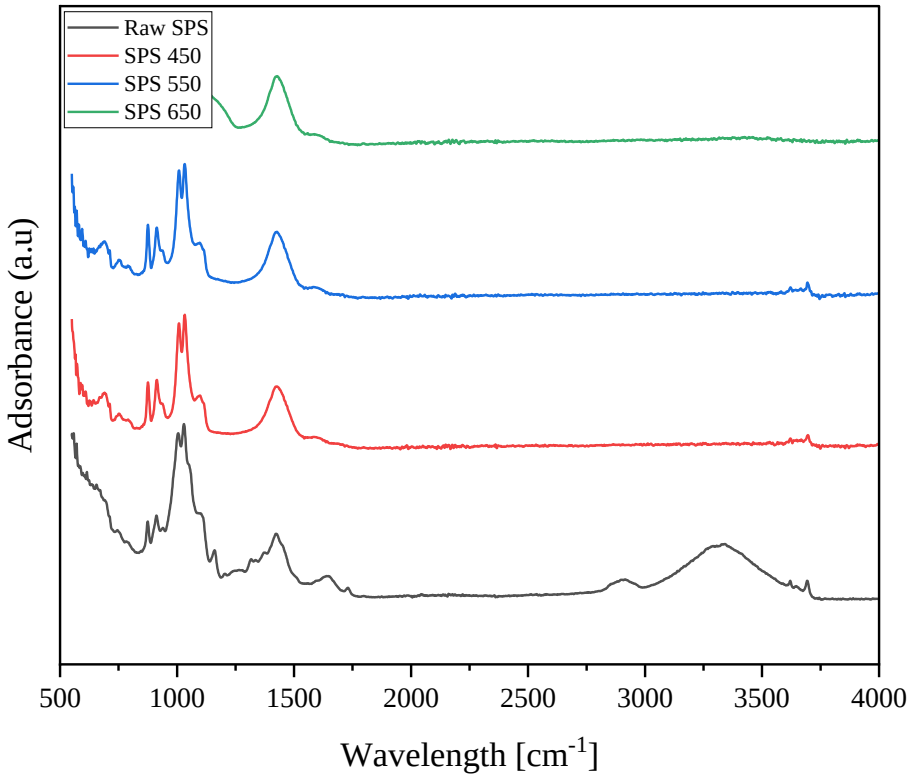

Figure 4. 3: FTIR spectra of (a) RPS and (b) MBC-SPS

4.2.4 Brunauer-Emmett-Teller analysis specific surface area

A Brunauer-Emmet and Teller analysis was performed to correlate surface area and carbonization temperature. The resultant biochar with the highest surface area was found to be RPS at 650 °C, as shown in Table 4.3. It is observed that the surface area increased with carbonization temperature (Devi & Saroha, 2015), due to thermal degradation of biomass organic matter and release of volatiles which encourages pore formation (Sahoo *et al*, 2021).

The resultant synthesized char after carbonization is characterized by relatively low surface areas when compared to pristine biochar, this is primarily due to the added formations of magnetite nanoparticles and amorphous $CaCl_2$ coating the surface (Chen *et al*, 2011; Mu *et al*, 2022). The (S_{BET}) analysis revealed an average 90 % reduction in surface area of 90 % at 450 °C, 42 % at 550 °C, and 46 % at 650 °C in the synthesized samples compared to pristine chars for both SPS and RPS. The observed results are much lower when compared to activated carbon due to the filler, coating and magnetic particles on the surface of the biochar (Sun *et al*, 2018).

Table 4. 4: Brunauer-Emmet and teller analysis results

Sample	Raw Sample	450 °C (m^2/g)	550 °C (m^2/g)	650 °C (m^2/g)
SPS	1.42	26.29	31.89	109.64
RPS	0.19	15.47	21.67	135.28
MBC-SPS	0.00	1.69	9.67	55.17
MBC-RPS	0.00	2.21	18.41	76.81

4.2.5 Scanning electron microscopy (SEM)

SEM images of RPWS and resultant pristine and synthesized biochar samples are shown in Figure 4.4, RPWS fibrous morphology of feedstock with clays present which is consistent with XRF and XRD findings. Flaky morphology is observed on the image of SPS and RPS is characterized by short tangled fibers with the presence of clumps of clays as well. SPS fibers are clumped together with CaO, TiO_2 and Kaolin. The quantities of CaO, TiO_2 and Kaolin are expected to be less in RPS due to washing during the pulping process.

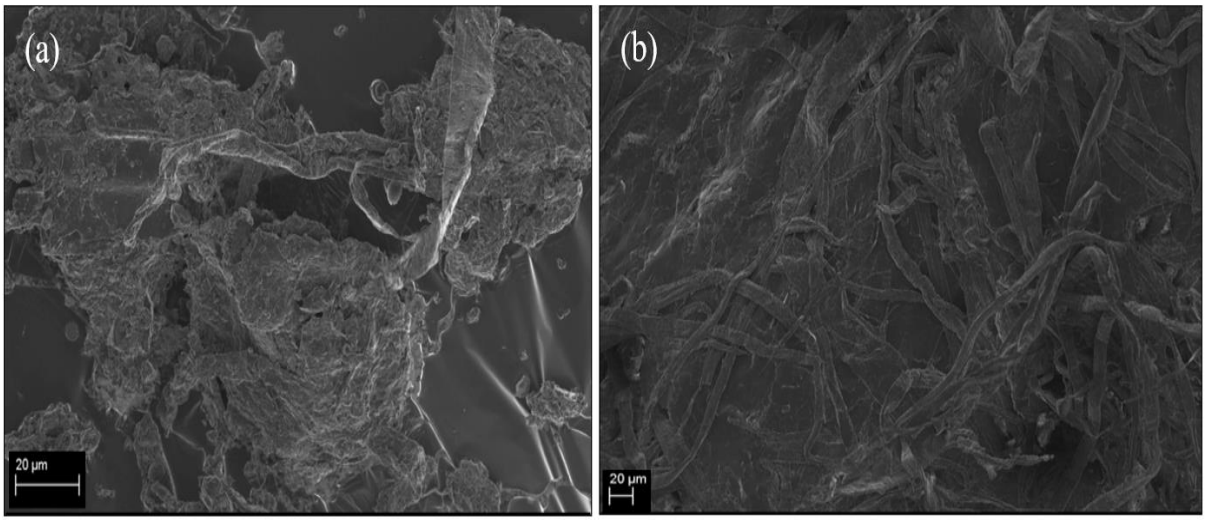

Figure 4. 4: SEM images RPWS variants at 20µ magnification (a) SPS and (b) RPS.

In Figure 4.5 - 4.6 the resultant pristine chars after carbonization at 450 ºC of both SPS and RPS are shown together with zoomed images of the surfaces. Pore development on the fibers and clays is observed due to devolatisation and continued dehydration. SPS pore development is observed to be more advanced than RPS and the fragmentation of filler and coating agent particles on the surface is more than that of RPS. The clays form smooth surface aggregates that are attached to the fibers.

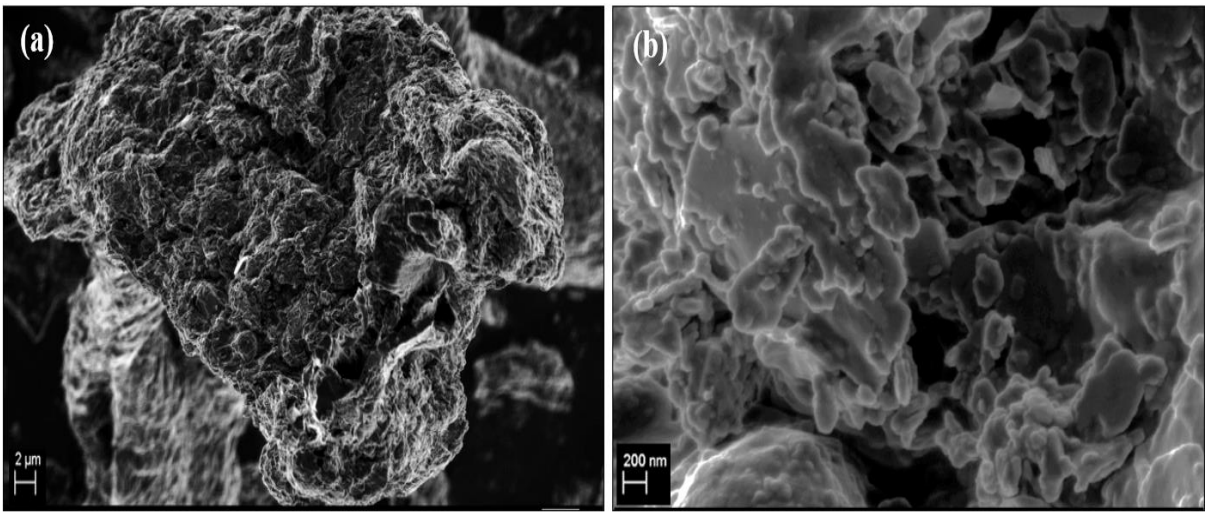

Figure 4. 5: SEM images of resultant SPS 450ºC pristine biochar (a) 2µ magnification and (b) 200µ magnification.

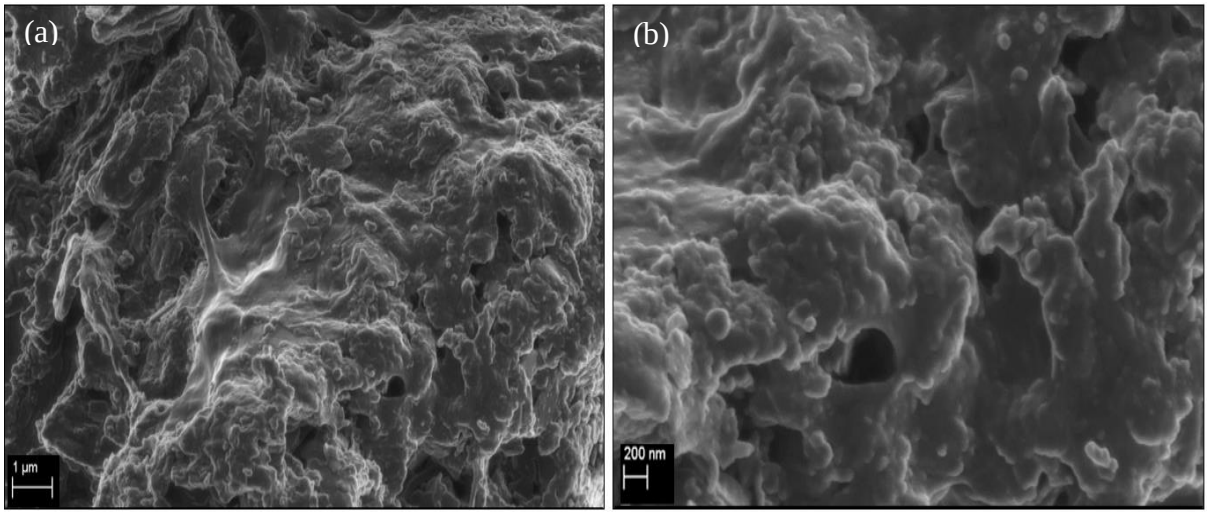

Figure 4. 6: SEM images of resultant RPS 450ºC synthesized biochar (a) 2µ magnification and (b) 200µ magnification.

The morphology of the synthesized biochar as shown in appendix C is observed to be similar to the pristine biochar, with the observed difference being the presence of nanoparticles coating the surface of the chars. Nanoparticles appear on the surface and in between pores, this observation is consistent with XRD findings of crystalline magnetite, $CaCO_3$, and $CaCl_2$ in the biochar matrix. The micrographs are also characteristic of kaolin in the matrix (Bundy & Ishley, 1991). The observed morphology of pristine and synthesized SPS and RPS biochar carbonized at 550 ºC as shown in Appendix C indicate further pore development and fragmentation of smaller clay and filler deposits on the surface of biochars, due to continued devolatisation and dehydration when carbonization temperature was increased, similar results were observed as shown in appendix D with biochar produced at 650 ºC due to the continuation in devolatisation and dehydration.

Synthesized char is observed to be coated with nanoparticles that are attached to the surface, an indication of successful impregnation. The oxides observed in XRF findings are consistent with this observation due to the presence of iron oxides in the biochar matrix. It is expected that $CaCO_3$, TiO_2, $CaCl_2$, and $AlSi_2O_5(OH)_4$ deposits will also form part of the matrix. The coating of these chars by nanoparticles explains the lower BET surface area due to pore blockages (Hong *et al*, 2020).

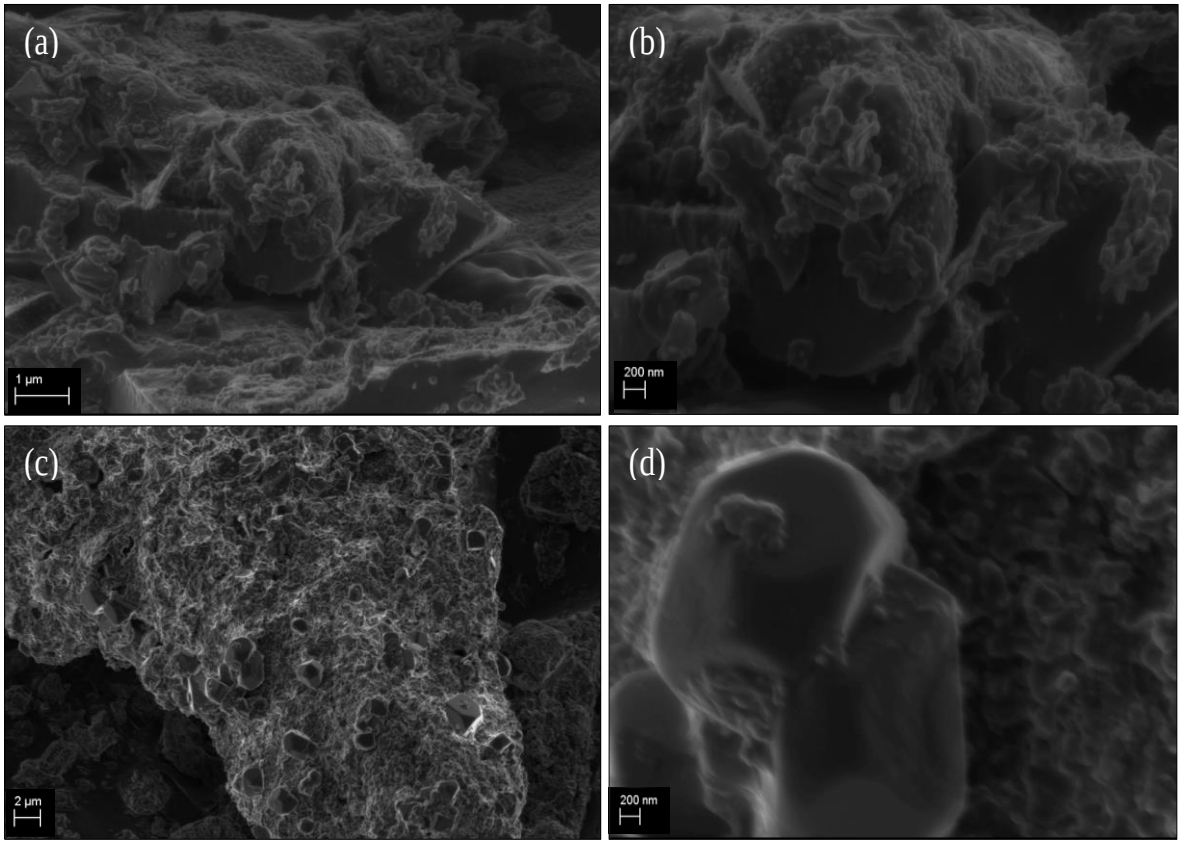

Figure 4. 7: SEM images of resultant 650 ºC synthesized biochar (a) RPS at 2µ magnification, (b) RPS at 200µ magnification, (c) SPS at 2µ magnification, (d) SPS at 200µ magnification.

4.2.6 Energy dispersive x-ray spectroscopy and elemental mapping

The spectra of RPWS as per displayed in Appendix D1 and Table 4.5 indicate the dominance of O and Ca elements on the surface of the biochar which is consistent with XRF findings on the oxides found within the matrix. The presence of Al, Si and Ti are due to the presence of fillers and coating agents in the fiber matrix which is consistent with SEM micrograph observations.

Table 4. 5: Elemental Analysis of raw SPS and RPS (wt.%, d.b)

Sample	S	Mg	Al	Si	Ca	Fe	Cl	Ti	O	Total
SPS	1.04	0.00	13.97	15.04	22.24	1.51	0.20	3.35	42.66	100.00
RPS	3.55	0.00	12.26	13.33	21.28	1.47	0.46	4.38	43.26	100.00

Calcium species has been used in the impregnation of biochar for adsorption studies and its presence has the potential to increase the adsorption capacity of resultant biochars (Feng *et al*, 2021a; Wang *et al*, 2021). Kaolinite composite biochars have also been found to poses higher adsorption capacities when compared to pristine biochars derived from the same materials (Gao & Goldfarb, 2021). (Cai *et al*, 2018) found titanium dioxide loaded biochars were possessed good adsorptive and photocatalytic properties. These characteristics of the resultant biochar indicate good adsorption potential.

There was negligible variation observed in the elemental composition of pristine biochar produced at 450 ºC, 550 ºC, and 650 ºC as observed in Table 4.6. elemental mapping and spectra are shown in Appendix D. It is observed that the only reactions that occurred were the coking of cellulose, hemicellulose, and lignin as observed by the slight increase in oxygen content.

Table 4. 6: Elemental Analysis of pristine resultant biochar (wt.%, d.b).

Sample	S	Mg	Al	Si	Ca	Fe	Cl	Ti	O	Total
RPS 450	3.03	0.00	10.25	9.23	31.57	1.44	0.00	1.30	43.18	100.00
RPS 550	1.00	2.40	7.90	11.90	12.70	0.00	0.00	2.90	61.20	100.00
RPS 650	1.17	1.36	10.36	12.23	28.49	1.44	0.63	2.80	41.52	100.00
SPS 450	0.00	0.00	13.10	14.20	18.30	0.80	0.00	2.70	50.90	100.00
SPS 550	1.00	1.00	13.20	14.40	24.80	1.40	0.00	2.60	41.60	100.00
SPS 650	0.24	0.72	13.71	15.58	22.32	1.18	0.11	3.06	43.08	100.00

Elemental spectra and mapping as per Appendix D2 confirm $CaCO_3$ dominance as the specie coating the surface of the biochar, the micrographs also indicate advanced fragmentation of the clays on the char surface. Clear deposits of Ca, Al, Si and Ti are clearly visible on the surface of the resultant chars. It is observed the biochar potentially possesses multiple adsorption sites including the larger pores in the matrix. These findings are consistent with results from other researchers who used similar feedstocks and the clay materials contained within the observed biochar matrix (Ghosh & Bhattacharyya, 2002; Nguyen *et al*, 2020; Setthaya *et al*, 2017; Wang *et al*, 2021)

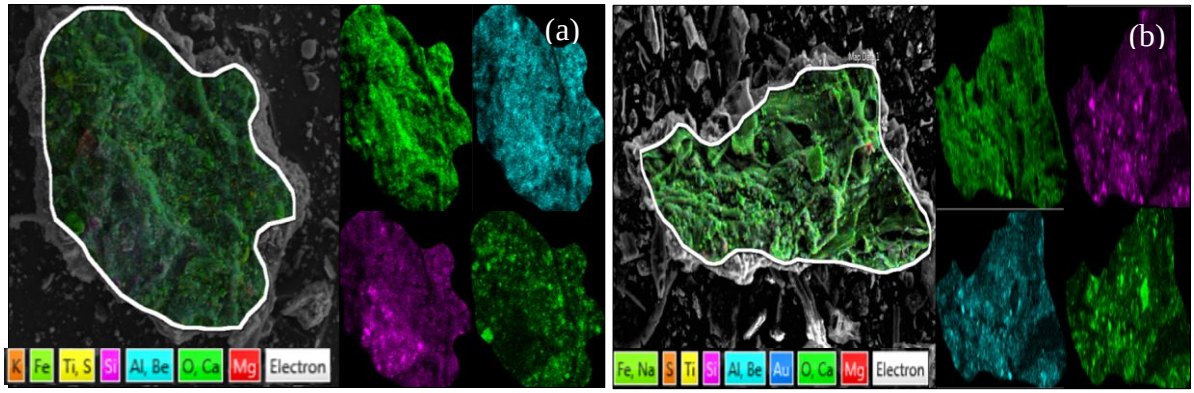

Figure 4.8: Elemental mapping of 550 ºC pristine biochar (a) SPS and (b) RPS.

Spectra produced by synthesized biochar as per appendix D3 and Table 4.7 is indicative of increased Fe, Cl in the mineral composition on the biochar surface, primarily due to impregnation. XRD plots indicated the presence of crystalline magnetite on the surface to confirm the successful magnetization of the resultant chars.

Table 4. 7: Elemental Analysis of synthesized resultant biochar (wt.%, d.b)

Sample	S	Mg	Al	Si	Ca	Fe	Cl	Ti	O	Total
MBC-SPS 450	0.40	0.00	8.83	8.62	8.63	27.27	14.47	1.33	30.41	99.96
MBC-RPS 450	0.33	3.42	6.60	11.32	1.61	25.48	17.23	2.74	31.28	100.01
MBC-SPS 550	0.00	0.62	6.29	6.09	12.34	28.31	19.25	0.67	26.43	100.00
MBC RPS 550	0.00	0.00	7.06	7.33	1.73	32.20	20.73	3.84	27.11	100.00
MBC-SPS 650	0.24	0.32	7.22	6.76	9.50	36.78	8.39	1.08	29.58	99.87
MBC-RPS 650	0.00	1.05	4.30	5.13	6.11	38.50	19.12	1.17	24.61	99.99

The biochar surface is constituted of Fe_3O_4 and $CaCl_2$, CaO which are evenly distributed on the surface while magnetite appears as deposits on the surface. Titanium dioxide and amorphous metakaolinite which forms at temperatures above 400 ºC were also observed on Figure 4.12.

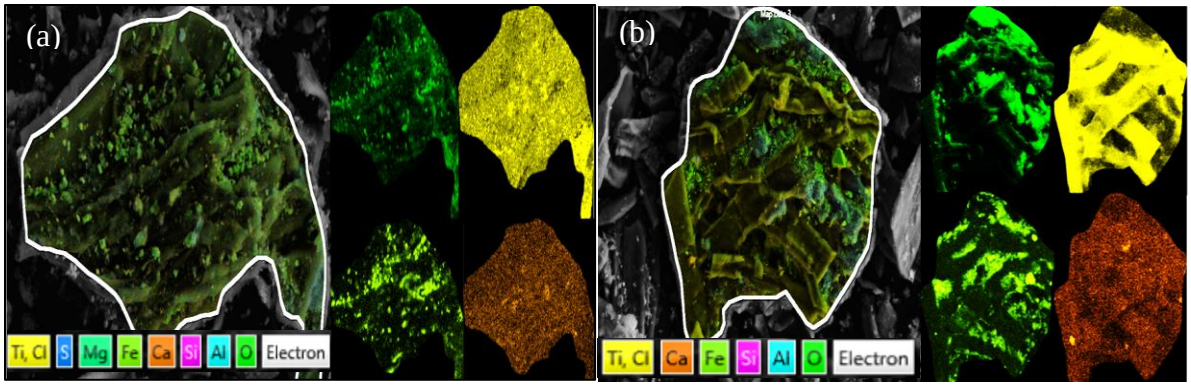

Figure 4.9: Elemental mapping of 650 ºC synthesized biochar (a) SPS and (b) RPS.

4.2.7 Transmission Electron Microscopy

TEM micrographs of the resultant pristine and magnetic biochar are shown on figure 4.13, the clear distinction between the two variants are the clearly visible nano particles on the biochar surfaces, the particles appear spherical and are distributed evenly without aggregation which potentially translates into excellent magnetic properties (Chen *et al*, 2011). The other variants micrographs can be seen in appendix E.

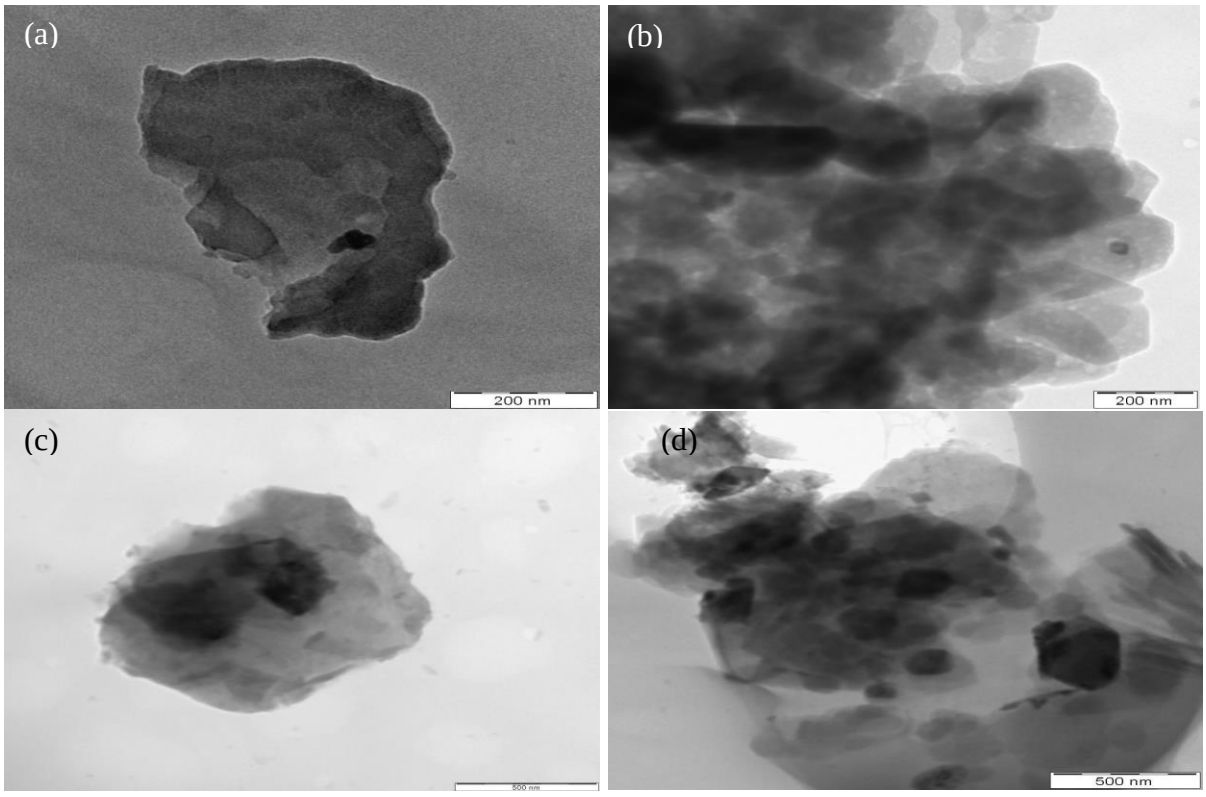

Figure 4.10: TEM Images of 450 ºC pristine and synthesized biochar (a) SPS, (b) RPS, (c) MBC SPS, and (d) MBC RPS.

Adsorption studies

5.1 Effect of carbonization temperature

5.1.1 Phosphorus removal

Figure 5.1 shows the adsorption of efficiencies of both pristine and magnetized biochars as a function of carbonization temperature. The results indicate high phosphorus removal efficiencies. The lowest observation was 89.70 % for RPS 450 and the highest at 99.88 % for the magnetized SPS variant. Carbonization temperature does affect Pristine biochar efficiency with observed marginal improvement of 4.65 % and 2.77 % for RPS and SPS biochar respectively when carbonization temperature is increased from 450 ºC to 650 ºC. higher SPS efficiencies were expected as it contains a higher amount of clays than RPS according to XRF results above. Higher adsorption efficiencies were observed for the magnetized variants primarily due to the presence of Fe_2O_4 nano formations on the surface of the synthesized biochars, similar results were reported by (Bhojappa, 2009; Chen *et al*, 2011).

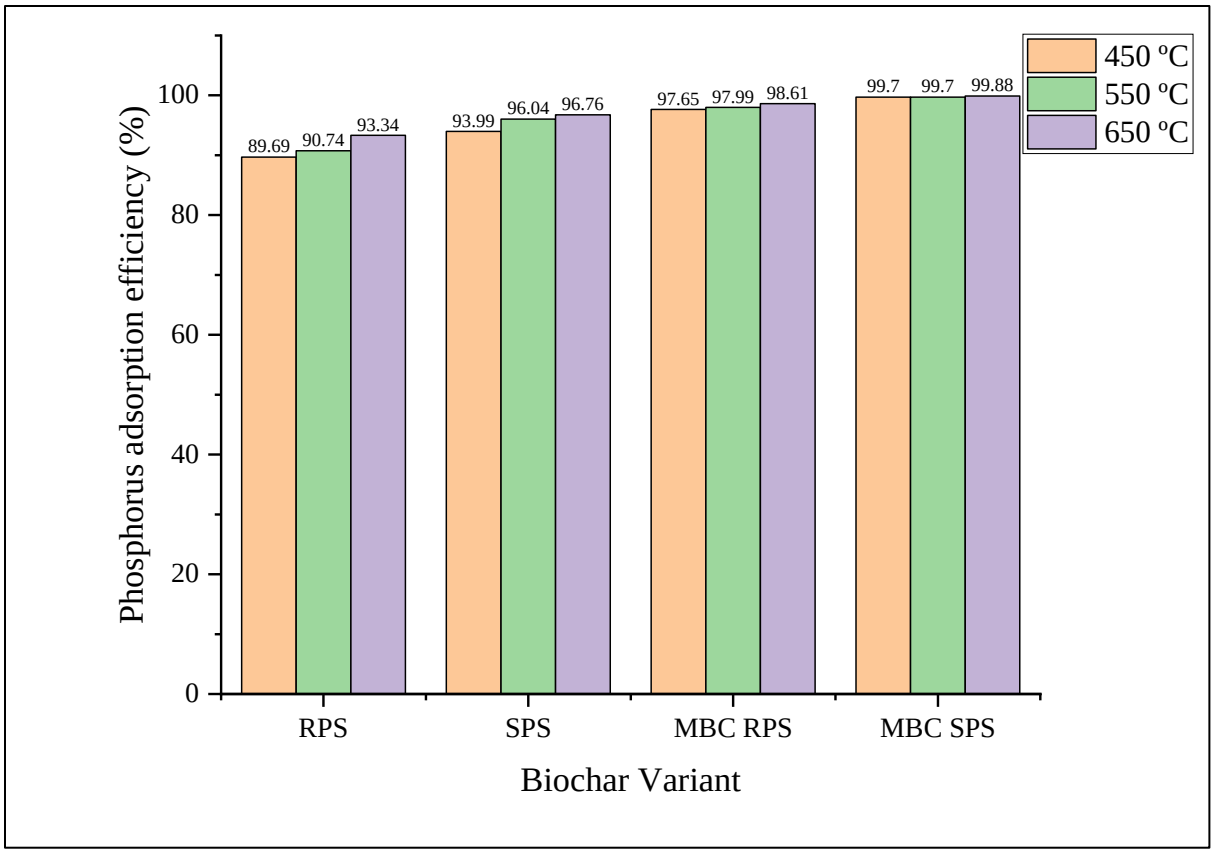

Figure 5. 1: Phosphorus Removal efficiencies of biochar.

MBC SPS variants produced higher efficiencies as expected due to higher mineral content as expected. similar observations in literature have been made by researchers such as (Chen *et al*, 2011; Cheng *et al*, 2021; Wang *et al*, 2021) who found similar mineral content to be highly beneficial in biochar composites. It is important to note that the 4.65 % improvement of efficiency can be primarily due to the increased available CaO and Ca^{2+} as $CaCO_3$ starts to decompose, there is an additional 7.2 % of available Ca in pristine SPS biochar when compared RPS (Wang *et al*, 2021).

Thermogravimetric results indicated the complete decomposition of the fiber between 400 ºC–450 ºC. The highest removal efficiencies were observed from the magnetized biochar, with all the chars achieving 97 % - 100 % adsorption of phosphorus from the solution. The initial; concentration was 110 mg/L and residual phosphorus concentration at the end of 24 h was observed to be below the 10 mg/L South African standard. The observed biochar efficiencies show the SPS variant as the more desirable adsorbent for phosphorus removal from an aqueous solution with the best adsorption efficiency.

5.1.2 Selenate removal

Selenate adsorption efficiencies are shown in Figure 5.2, lower adsorption efficiencies were observed in comparison to phosphorus, with the lowest efficiency observed at 73.26 % by pristine RPS 550 biochar and the highest efficiency observed at 84.86 % by the synthesized MBC SPS 450. Synthesized biochars were expected to have higher adsorption efficiency due to their affinity for $Se_2O_4^{2-}$, moreover, the basic nature of the Fe_3O_4 on the surface of the biochars increases the adsorption of the more basic $Se_2O_4^{2-}$ (Wei *et al*, 2021).

The observed biochar adsorption efficiencies indicate the synthesized biochars as the best performing adsorbate with MBC-RPS having the highest efficiencies. It is hypothesized that Ca^{2+} and Mg^{2+} ions also significantly increase the adsorption efficiency of $Se_2O_4^{2-}$; this assertion is consistent with results by (Guo *et al*, 2021). (Yamani *et al*, 2014) also reported excellent results using a characteristically similar material.

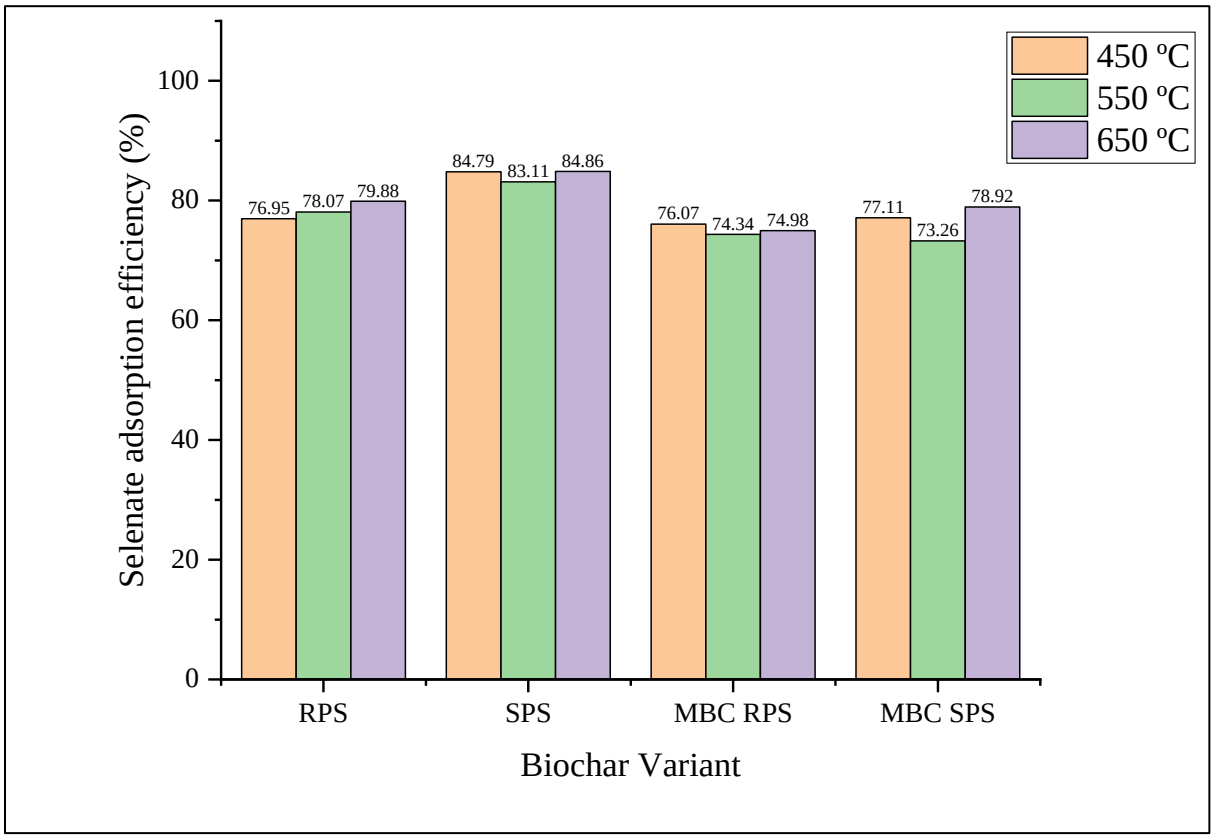

Figure 5. 2: Selenate Removal efficiencies of biochar.

5.1.3 Methylene blue removal

Methylene blue exhibited high adsorption efficiencies across all biochar variants as shown in Figure 5.3. This can be attributed to the high surface area, abundant pore structure, volume, and strong adsorption affinity of the biochars, similar results were reported by (Gao & Goldfarb, 2021; Mu *et al*, 2022). The presence of clay mineral composites such as kaolinite enhances the adsorption of methylene blue by the biochars due to synergic effects of various interactions such as hydrogen bonding, ion exchange, π-π interaction, and surface adsorption (Ghosh & Bhattacharyya, 2002; Mouni *et al*, 2018). kaolinite was found to present excellent adsorption efficiencies of methylene blue and the presence of TiO_2 further demonstrated enhanced photocatalytic degradation of methylene blue (Setthaya *et al*, 2017). The highest adsorption efficiencies were observed to be by MBS SPS 650 (98.72 %) while the lowest efficiencies were observed for RPS 450 (85.40 %), pristine biochar adsorption efficiency is observed to be lower than that of synthesized biochar, these results are similar to findings by (Mak & Chen, 2004) (Mubarak *et al*, 2015; Zhang *et al*, 2020).

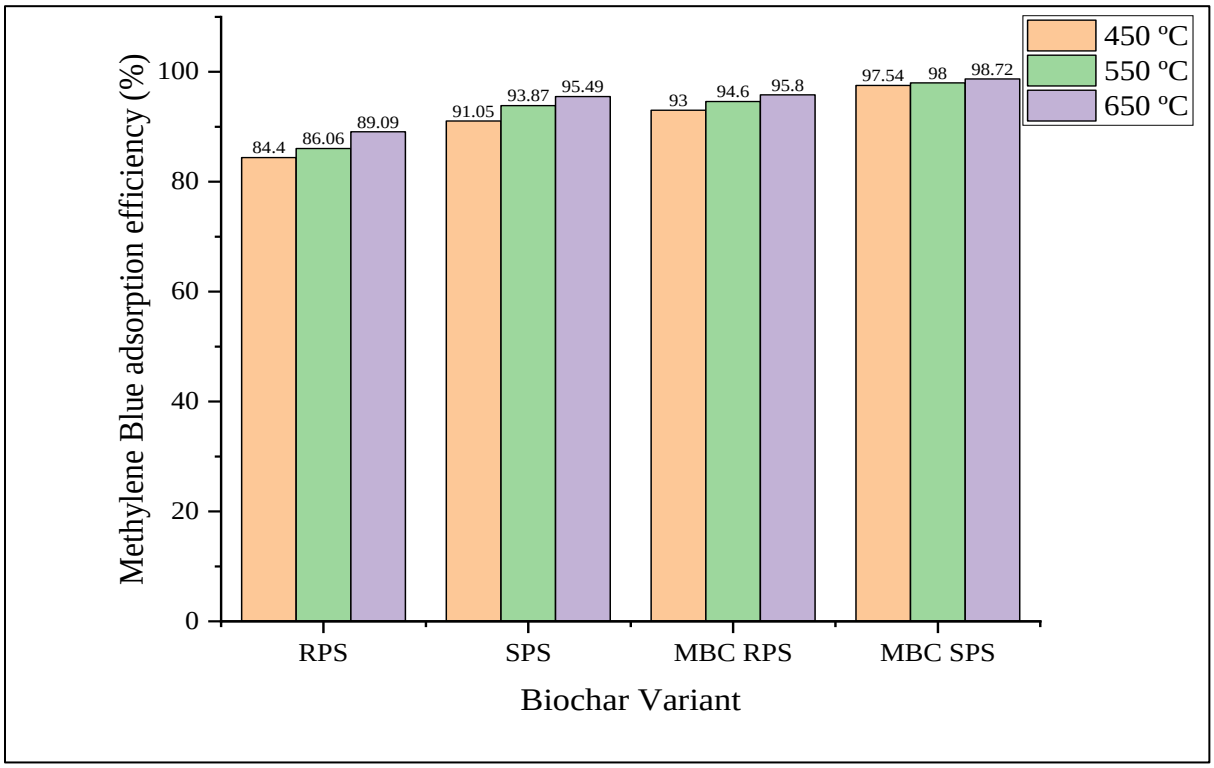

Figure 5. 3: **Methylene blue Removal efficiencies of biochar.**

MBC-SPS 450 was chosen as the primary adsorbent for further experiments due to high adsorption efficiency across the three adsorbates and the requirement of less energy of production translating into lower production cost.

5.2 Effect of adsorbent loading

5.2.1 Phosphorus

Figure 5.4 shows the phosphorus, selenium, and methylene blue adsorption of efficiencies as a function of adsorbent loading. For phosphorus, a 4.37 % increase in efficiency was observed when loading was increased from 2.5g/L to 5g/L and no further increases when further increased to 10 g/L and 20 g/L respectively. 9 The observation on phosphorus adsorption as a function of loading is that as the increased loading presented additional active sites and functional groups which translated into additional adsorption sites, an increase in loading over a certain limit can reduce the available active sites for adsorption although the dispersion is uniform (Tabana *et al*, 2020). 5 g/L was selected as the optimum loading and used in subsequent experiments for Phosphorus.

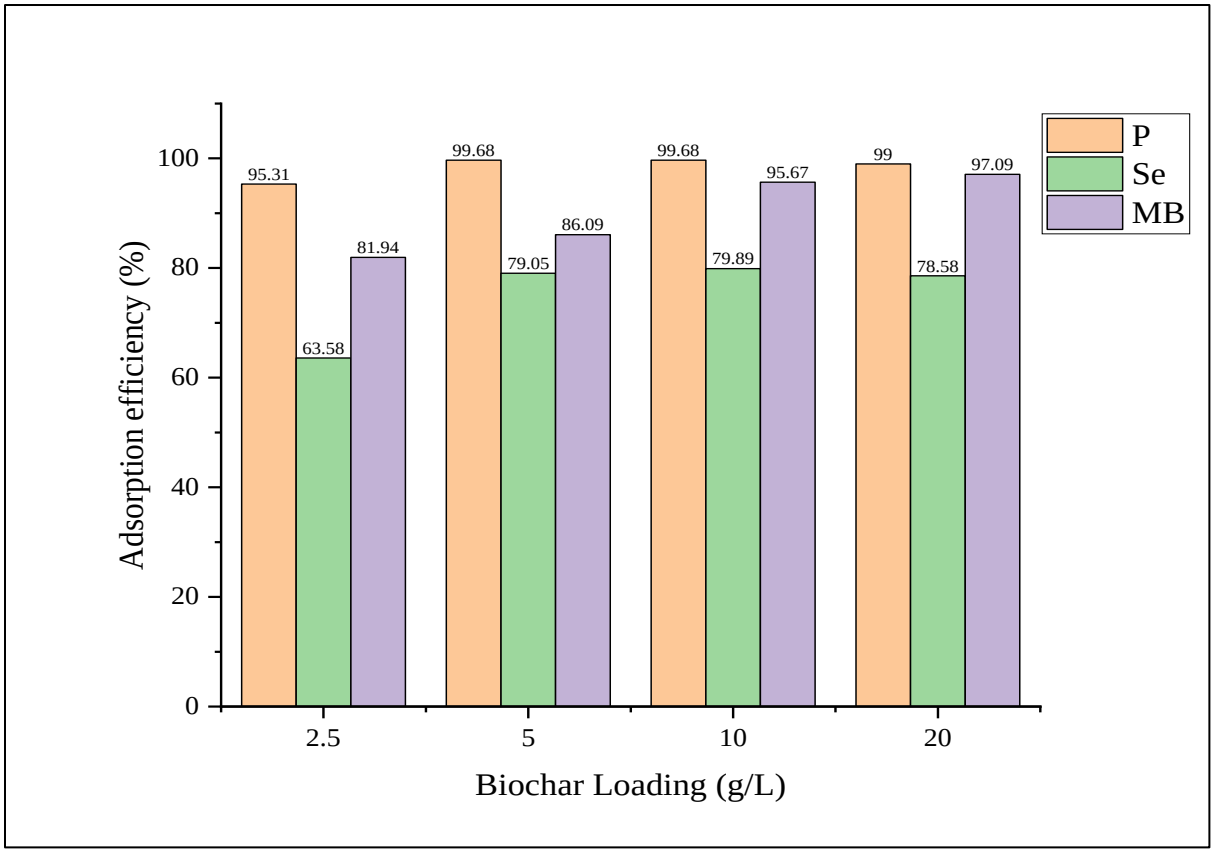

Figure 5. 4: Effect of biochar loading on adsorption efficiencies for P, Se, and MB.

5.2.2 Selenium

Selenium adsorption efficiencies largely increased by 15 % when loading was increased from 2.5 g/L to 5 g/L and a marginal increase was observed when further increased from 5 g/L to 10 g/L. The efficiency then reduced by 1.31 % when loading was increased to 20 g/L results that are consistent with an observation similar to findings by (Lee *et al*, 2021). The optimum loading for selenate given the results is 5 g/L and as such the loading was used in subsequent experiments.

5.2.3 Methylene blue

Methylene blue adsorption efficiencies followed a similar trend to that of phosphorus and selenate where a higher loading translated into higher efficiencies, the lowest efficiency was 81.94 % at 2.5 g/L and the highest was observed as 97.09 % when the loading was increased to 20 g/L, this can be attributed to more adsorption sites available for the dye when increasing the loading, results which are similar to findings by (Mubarak *et al*, 2015; Zhang *et al*, 2020).

Efficiency can significantly improve as optimum loading is reached and significantly reduce due to loading beyond the optimum loading (Cheng *et al*, 2021); from these observations, the optimum loading was selected as 5 g/L which was used in subsequent experiments.

5.3Effect of pH and contact time

5.3.1 Phosphorus

The influence of contact time and initial wastewater pH is significant for efficient adsorbate removal. Phosphorus adsorption efficiencies observed at various initial pH of the solution are shown in Figure 5.5. The dominant phosphorus ion is completely dependent on pH and the major forms of phosphorus at different pH values is as follows; H_3PO_4 (pH <2.16), $H_2PO_4^-$ (pH = 2.16 – 7.21), HPO_4^{2-} (pH = 7.21-12.31) and PO_4^{3-} (pH > 12.32) (Wang *et al*, 2021). During this study, the applicable forms of phosphorus were $H_2PO_4^-$ and HPO_4^{2-}(Wang *et al*, 2021). During the studies, available calcium species reacted in solution with water to release Ca^{2+} and OH^- thereby slightly increasing the reaction pH. When the solution pH was fixed at 5 the resultant pH after the addition of biochar was 6.92, pH 7 increased 8.8 while solution pH 9 ended at 11.02. Therefore, the expected that the dominant phosphate ion was $H_2PO_4^{2-}$.

The lower removal efficiency at pH 5 is attributed to the existence of $H_2PO_4^-$ which could not complex and precipitate with Ca^{2+} in the form of $CaHPO_4.2H_2O$ nor bind to the magnetite nanoparticles on the surface of the char. As pH was increased the efficiency also increased by 6.41 % and 0.7 % from pH 7 to 9 respectively. It is observed that the performance variability was negligible due to the abundant species available on the surface of the biochar. This indicates the availability of sorption sites for the dominant P species across a wide range of Ph values. These results further support the non- demineralization of the feedstock as these filer and coating agent oxides contribute to this observed efficiency. It can be seen that the reaction reaches equilibrium within an hour with marginal increases in efficiency after that, the biochar performs exceptionally when in varying conditions is an excellent characteristic as it can be applied to effectively sorb phosphorus in varying pH conditions.

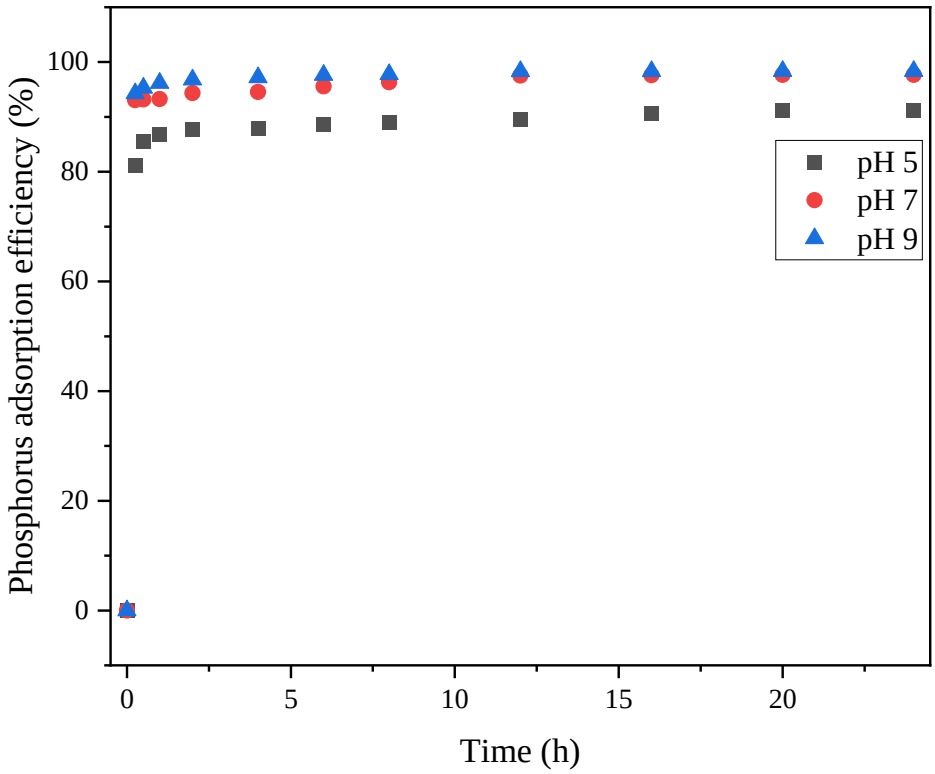

Figure 5. 5: Effect of pH and time on phosphorus adsorption efficiency.

5.3.2 Selenium

The influence of pH on selenate adsorption is depicted on Figure 5.6. As the pH was increased from 5 to 9, the removal efficiency marginally changed. SeO_4^{2-} is the dominant ion in an aqueous system at a pH range of 3 to 11 (Hong *et al*, 2020). Due to the abundance of positively charged species in the biochar matrix electrostatic attractions are created between SeO_4^{2-} and positively charged ions (Godlewska *et al*, 2020). Adsorption as a function of time indicates that equilibrium was reached within an hour with marginal increases at 16h. The results are not consistent with (Bhojappa, 2009; Lee *et al*, 2021) whose findings indicated that at as pH is increased selenate removal efficiency would be expected to reduce, it is hypothesized that the effect of available clay minerals negated this effect.

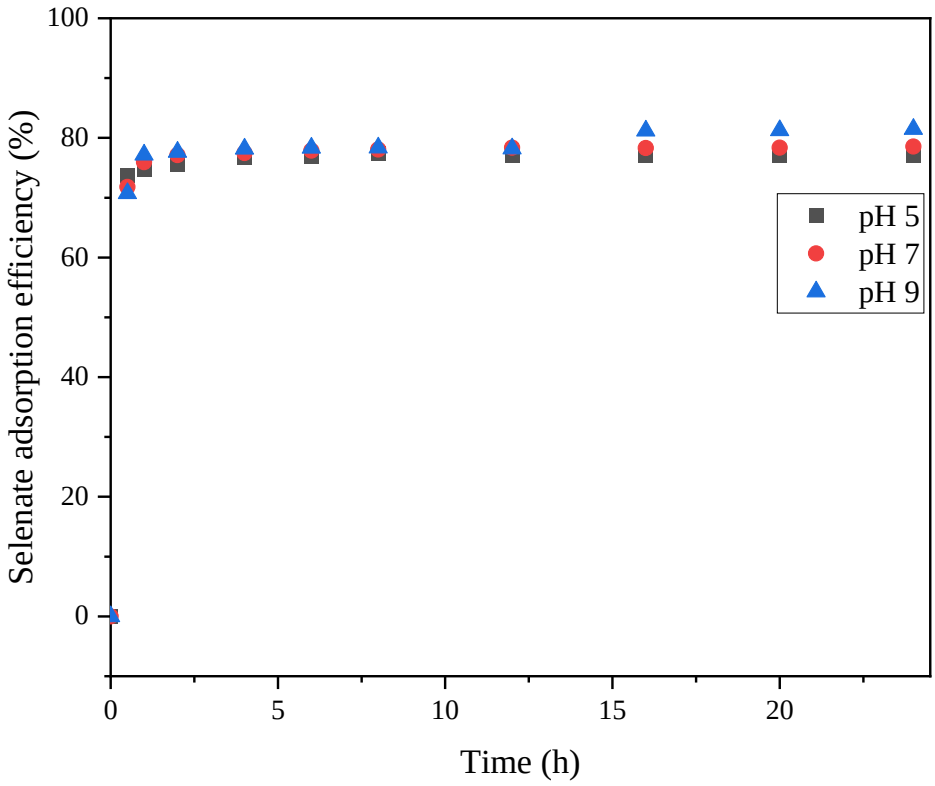

Figure 5. 6: Effect of pH and time on selenate adsorption efficiency.

5.3.3 Methylene Blue

Methylene blue's highest removal efficiency was observed at pH 5 and 9. An increase in pH value decreases the density of the dye's surface charge subsequently decreasing the electrostatic repulsion between the biochar and cationic methylene blue. The high adsorption efficiency at a lower pH value is due to the dye replacing OH^- on the biochar surface (Mubarak *et al*, 2015). Equilibrium is reached within an hour and marginally increases with time and stabilizes with marginal change afterward, similar results were reported by (Mak & Chen, 2004; Mubarak *et al*, 2015).

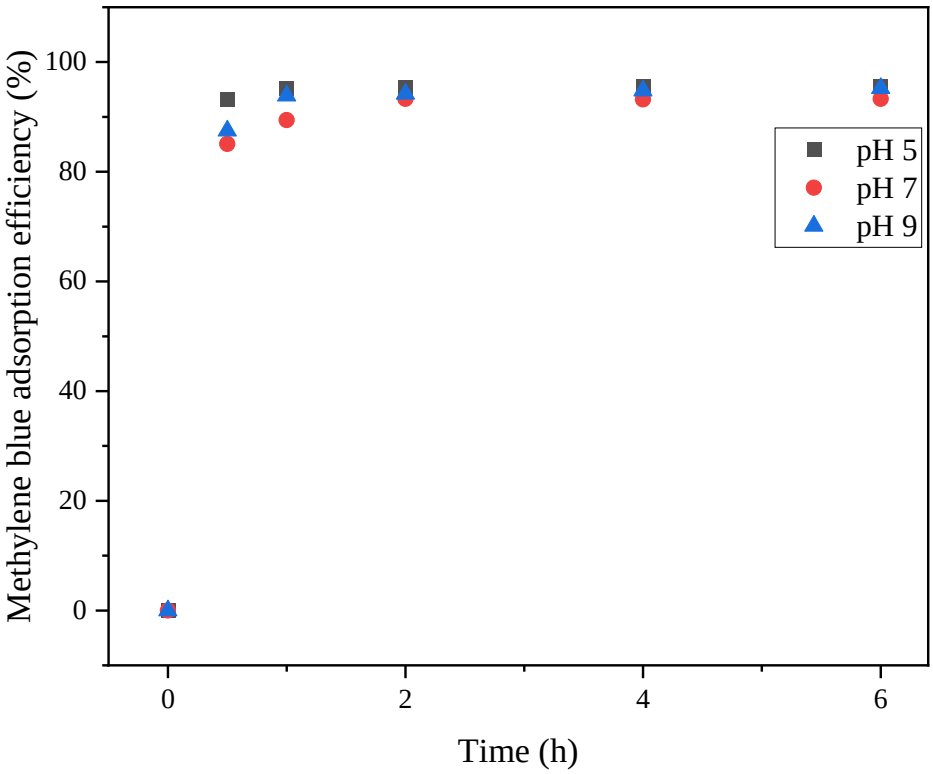

Figure 5. 7: Effect of pH and time on methylene blue adsorption efficiency.

5.4 Adsorption mechanism

To thoroughly understand the possible adsorption mechanism of phosphorus, selenium, and methylene blue, complementary characterization was performed on the biochar.

5.4.1 Selenium

For selenate the adsorption mechanism with magnetite containing biochars is surface complexation which can be classified as an outer and inner sphere, Al, Si, and Fe oxides on the surface of materials are the dominant sorption mechanism for selenate through the outer sphere complexation. XRF results do not indicate a change in the oxides present except CaO which was reduced by 73 %. The outer sphere dominated at pH>8 while the inner sphere dominated at pH<7 (Benis *et al*, 2022; Hong *et al*, 2020). The availability of released Ca^{2+} and Mg^{2+} is also effective in the removal of SeO_4^{2-} by precipitation via the inner sphere coordination, results which are similar to findings by (Guo *et al*, 2021).

Table 5. 1: XRF analysis of neat and spent biochar.

Sample	SiO_2	Al_2O_3	MgO	Na_2O	Fe_2O_3	TiO_2	CaO	P_2O_5	SO_3	K_2O	LOI	Total
MBC SPS 450	14.07	11.50	1.00	0.00	12.14	1.35	12.63	0.14	0.04	0.00	47.12	99.99
MS Se	16.93	14.06	1.01	0.00	15.98	1.76	3.32	1.15	0.00	0.13	46.65	99.99

The presence of Calcium-Silicate-Hydrate (C-S-H) phases and Al/Si oxides seems to also be an important mechanism for SeO_4^{2-} adsorption as per EDS elemental Mapping and quantification, C-S-H phases with higher calcium content were found to be good adsorbent through surface complexation of SeO_4^{2-}, the results are indicative of complexation on the surface of the biochar, further supported by the reduction in the elemental concentration of kaolinite in the matrix, a similar phenomenon was reported by (Missana *et al*, 2019; Tian *et al*, 2021).

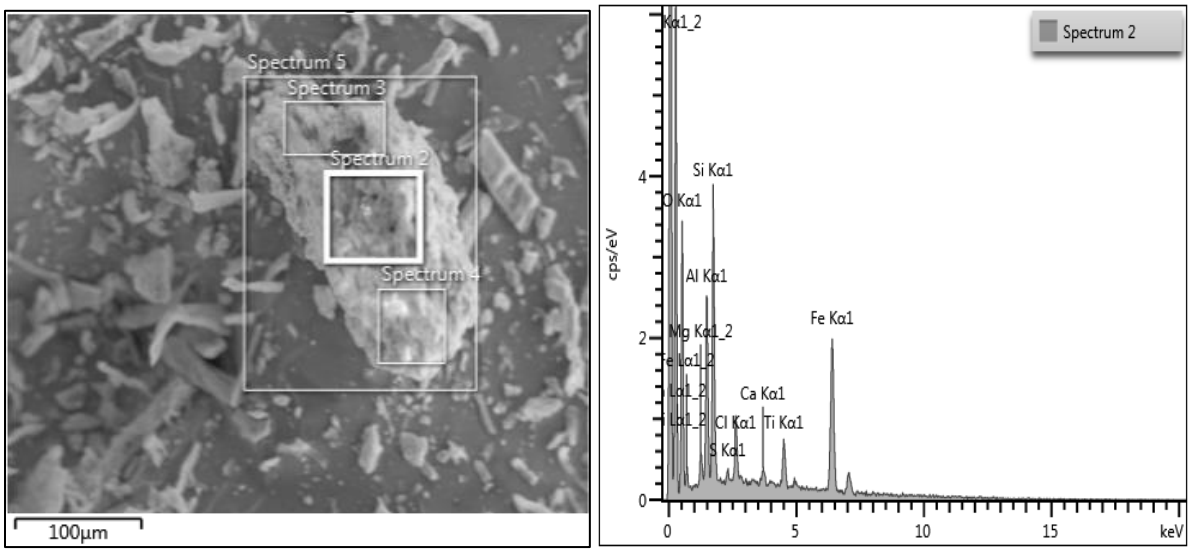

Figure 5. 8: EDS elemental mapping of Spent Biochar after selenate adsorption.

Table 5. 2: Elemental analysis of spent biochar after selenate adsorption (wt.%)(d.b)

Sample	O	P	Al	Si	Ca	Fe	Cl	Ti	S	Total
MBC SPS 450	30.41	0.00	8.83	8.62	8.63	27.27	14.47	1.33	0.40	100
MS Se	31.26	1.75	3.92	4.94	3.71	38.42	14.51	0.84	0.64	100

XRD results as shown in Figure 5.9 do not indicate a difference in the phase purity of the spent biochar used for selenate adsorption, as observed above with EDS elemental mapping, only the elemental concentration of the phases was reduced with the structure.

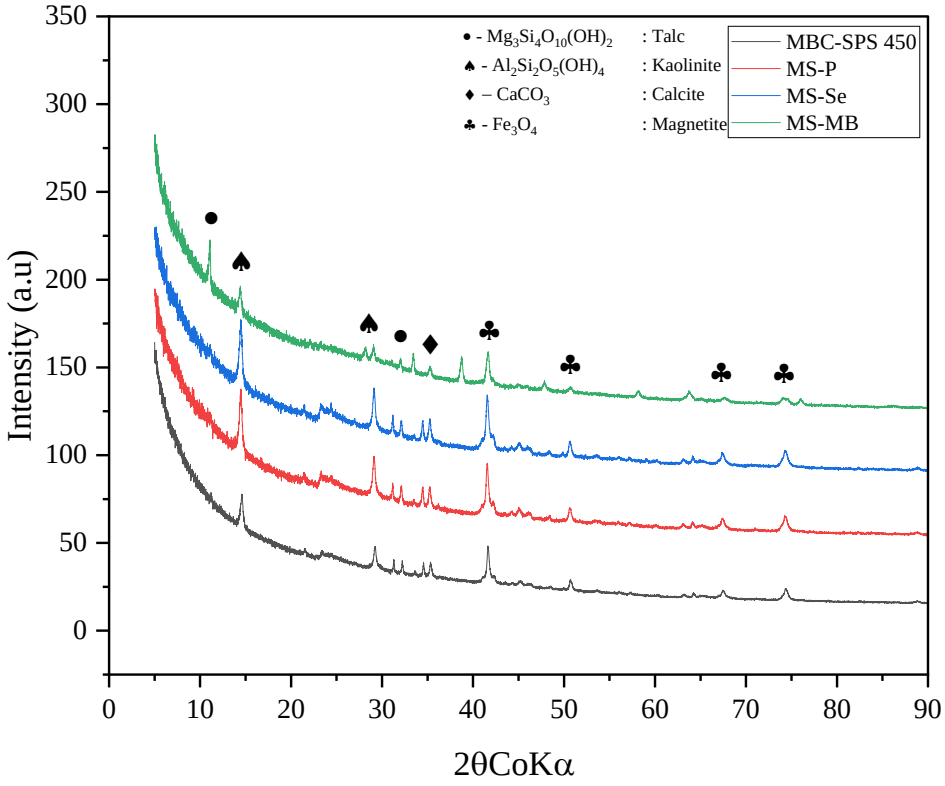

Figure 5. 9: XRD plots for neat and spent biochar.

5.4.2 Phosphorus

Phosphorous sorption is a complex process involving complexation, ligand exchange, electrostatic attraction, precipitation, and other mechanisms (Pei *et al*, 2021). For phosphorus, the adsorption mechanism was chemisorption with the positively charged Mg^{2+}, $Ca^{2+,}$ and magnetite on the surface of the biochar offering abundant adsorption sites. The dissolution of calcium species also contributed to the removal of phosphorus ions $H_2PO_4^-$ and HPO_4^{2-} in the pH 6-11 range. The release of calcium and OH^- species due to the reaction of active calcium species with water increased original solution pH and precipitated phosphorus, an observation consistent with findings by (Wang *et al*, 2021) who used a similar feedstock without magnetite.

Table 5. 3: XRF analysis of neat and spent biochar after phosphorus adsorption.

Sample	SiO_2	Al_2O_3	MgO	Na_2O	Fe_2O_3	TiO_2	CaO	P_2O_5	SO_3	K_2O	LOI	Total
MBC-SPS 450	14.07	11.50	1.00	0.00	12.14	1.35	12.63	0.14	0.04	0.00	47.12	99.99
MS P	16.47	13.88	1.01	0.00	14.61	1.65	4.97	0.82	0.01	0.22	46.34	99.99

Similar to Selenite above, precipitation and adsorption $H_2PO_4^{2-}$ onto the biochar surface did not significantly affect the oxides present in the matrix, with the exception of CaO which released Ca^{2+} to further complex and precipitate with phosphorus as per Equation 5.1 – 5.3. XRD results also indicate no structural changes to the biochar matrix's phase purity.

The dominant chemical precipitation of phosphorus due to released Mg^{2+}, Ca^{2+} is described by the mechanism is as follows:

$$CaO + H_2O \rightarrow Ca^{2+} + 2OH^- \quad (5.1)$$

$$Ca^{2+} + HPO_4^{2-} \rightarrow CaHPO_4 \quad (5.2)$$

$$3HPO_4^{2-} + 5Ca^{2+} + 4OH^- \rightarrow Ca_5(PO_4)_3(OH) + 3H_2O \quad (5.3)$$

Elemental mapping results as per Figure 5.10 and Table 5.4 indicate the presence of Phosphorus on the surface of the chars. This is due to the complexation on the magnetite nanoparticles a result which is consistent with findings by other researchers (Bhojappa, 2009) (Li *et al*, 2016b). The clear distinctive absence of Ca on the surface of the biochar matrix also confirms the hypothesis that phosphorus is complexed with Ca^{2+} and precipitated out of solution, other researchers reported similar findings (Feng *et al*, 2021a; Wang *et al*, 2021).

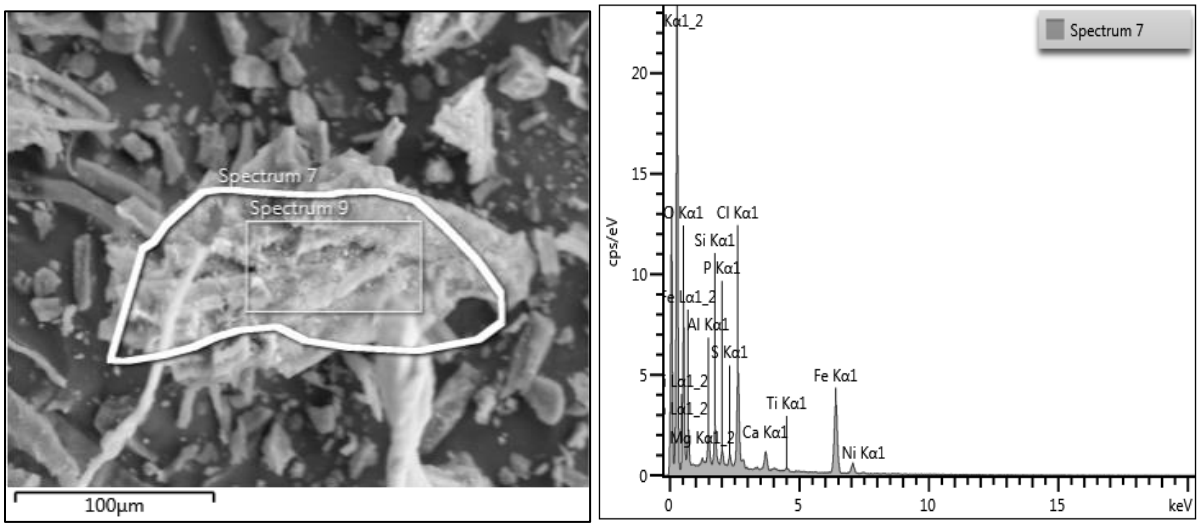

Figure 5. 10: EDS elemental mapping of Spent Biochar after phosphorus adsorption.

Table 5. 4: Elemental analysis of spent biochar after phosphorus adsorption (wt.%, d.b)

Sample	O	P	Al	Si	Ca	Fe	Cl	Ti	S	Total
MBC-SPS 450	30.41	0.00	8.83	8.62	8.63	27.27	14.47	1.33	0.40	100
MS-P	41.02	1.63	3.90	4.29	2.86	30.81	13.54	0.87	1.10	100

5.4.3 Methylene Blue

Physisorption is the main adsorption mechanism for methylene blue onto magnetite, due to hydrogen bonding, π-π interactions, and electrostatic attractions (Mu *et al*, 2022). It is also observed on the EDS mapping as per Figure 5.11 that Methylene blue occupied the abundant active sites on the biochar surface results consistent with findings by (Mu *et al*, 2022; Zhang *et al*, 2020) who found π-π interaction, electrostatic attraction, and Hydrogen bonding to be the dominant adsorption mechanisms between magnetite and methylene blue.

Table 5. 5: XRF analysis of neat and spent biochar after methylene blue adsorption.

Sample	SiO_2	Al_2O_3	MgO	Na_2O	Fe_2O_3	TiO_2	CaO	P_2O_5	SO_3	K_2O	LOI	Total
MBC-SPS 450	14.07	11.50	1.00	0.00	12.14	1.35	12.63	0.14	0.04	0.00	47.12	99.99
MS MB	7.82	3.53	1.53	0.12	15.38	0.90	1.28	0.07	0.00	0.04	69.17	99.99

TiO_2 and kaolinite containing LDH clays have proven to be efficient in the removal of methylene blue from solution (Mouni *et al*, 2018; Rida *et al*, 2013). The excellent adsorption efficiency of methylene blue by MBC-SPS is supported by these findings which are reported by (Asuha *et al*, 2020; Ghosh & Bhattacharyya, 2002) who found kaolin to present excellent adsorption capacities for methylene blue, which is further supported by the observed XRF results as per Table 5.5 indicate reduced kaolin oxides on the biochar surface and XRD Plots where only Kaolin's peak reduction is distinctively reduced.

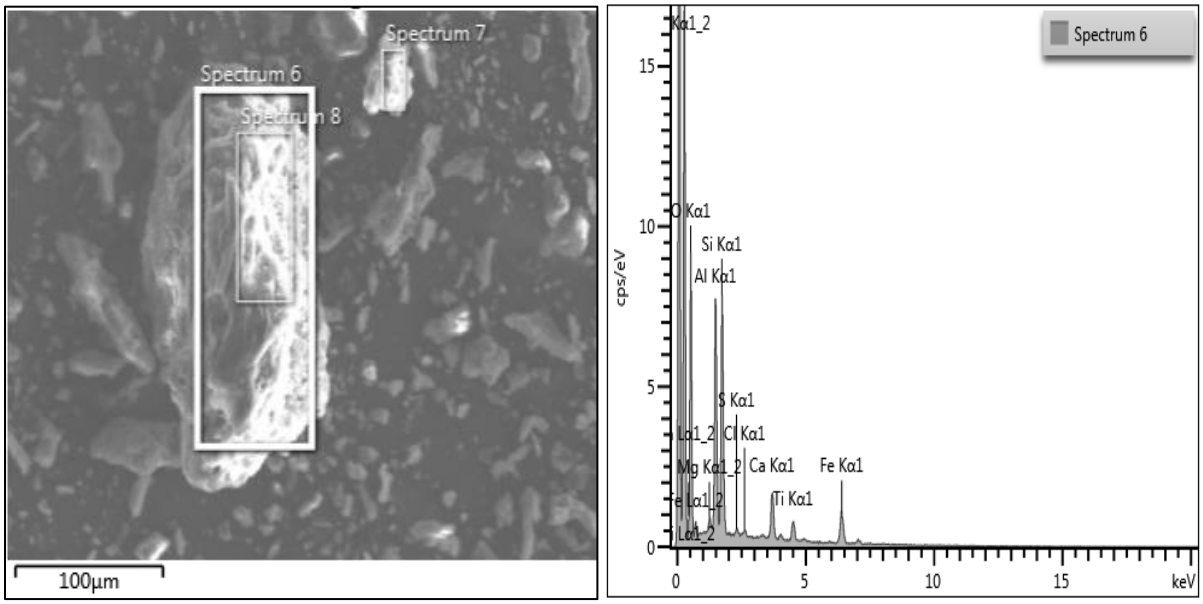

Figure 5. 11: EDS elemental mapping of Spent Biochar after methylene blue adsorption.

Table 5. 6: Elemental analysis of spent biochar after methylene blue adsorption.

Sample	O (% d.b)	Mg (% d.b)	Al (% d.b)	Si (% d.b)	Ca (% d.b)	Fe (% d.b)	Cl (% d.b)	Ti (% d.b)	S (% d.b)	Total
MBC-SPS 450	30.41	0.00	8.83	8.62	8.63	27.27	14.47	1.33	0.40	100
MS-MB	35.92	0.75	11.47	12.16	5.36	29.77	0.64	3.05	0.88	100

5.5 Adsorption Isotherms

To further understand the form and nature of interactions between the biochar and adsorbate solutions, obtained experimental data were fitted to the Langmuir, Freundlich, and Sips isotherm models. Langmuir isotherm model is empirical and assumes homogeneous monolayer adsorption in which adsorption occurs at identical and equivalent definitive localized sites where the rate of adsorption and desorption is equal. Freundlich isotherm model on the hand describes reversible and non-ideal multi-layer adsorption process which is not restricted like the monolayer formation. Sips isotherm model combines both the Langmuir and Freundlich isotherm models, it was deduced to predict the heterogenicity of the adsorption process as well as to circumvent the limitations associated with increased concentrations of the adsorbate of the Freundlich model (Al-Ghouti & Da'ana, 2020).

5.5.1 Phosphorus

Figure 5.12, appendix F-1 and Table 5.7 show the relationship between the equilibrium phosphorus concentration and the biochar adsorption capacity, the adsorption parameters were calculated using equations 2.2 - 2.8. The adsorption capacity change was negligible when pH was increased from pH 5 to pH 7 and ultimately pH 9 averaging 43.67 mg/g, when Phosphorus concentration was increased from 49.88 mg/L to 220.47 mg/L indication good variability of the adsorbent due to the biochar matrix.

The adsorption of phosphorus by biochar was found to be well described using the Freundlich isotherm model. The coefficient of determination (R^2) was higher for Freundlich than Langmuir isotherm model, indicative of a heterogenous biochar adsorption surface. The slope (1/n) is favorable for adsorption at pH 7 and 9 while the results indicate unfavorable adsorption at pH 5, these could be due to the different mechanisms at play because of the different oxides within the biochar matrix (Al-Ghouti & Da'ana, 2020).

Table 5. 7: Phosphorus adsorption isotherm parameters.

	Freundlich				**Langmuir**			**Sips**		
pH	K_F (L/g)	N	R 2	1/n	q_m (mg/g)	R 2	b	β_s	K_s	α_s
5	6.865	0.492	0.929	0.49	-19.12	0.983	-0.289	0.100	2.160	0.855
7	3.675	0.380	0.780	0.38	-11.468	0.633	-0.319	0.088	1.944	0.865
9	12.95	0.231	0.999	0.23	-5.605	0.972	-0.686	0.276	1.791	0.884

Based on the data MBC SPS was found to have phosphorus adsorption capacity comparable to and better than other similar biomass-derived biochars, paper waste sludge (calcium-containing) (Wang *et al*, 2021) Orange peel (Fe^{3+}/Fe^{2+} co-precipitation) (Chen *et al*, 2011) wood chips (Fe impregnation) (Micháleková-Richveisová *et al*, 2017)Acid mine drainage (Bhojappa, 2009) Sugarcane harvest (MgO impregnated) (Li *et al*, 2016a).

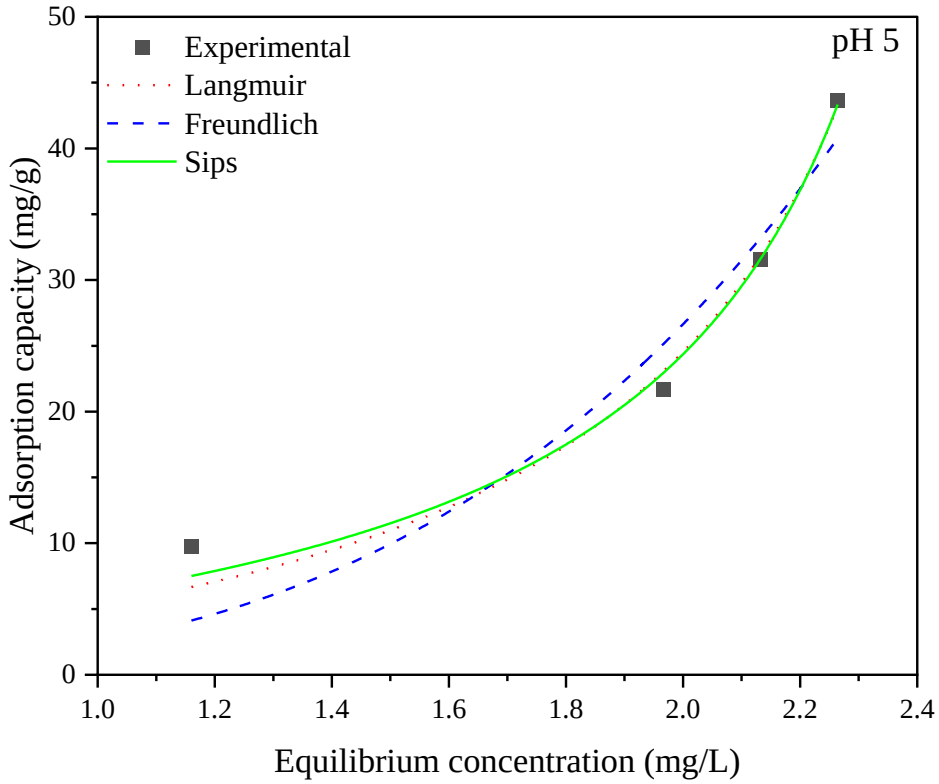

Figure 5. 12: Phosphorus adsorption isotherms at pH 5

5.5.2 Selenate

Langmuir, Freundlich, and Sips isotherm models we also used to characterize adsorption processes at equilibrium, the relationship between final selenate concentration and adsorption capacity of MBC SPS is indicated in Figure 5.13 and appendix F-2, the adsorption process fits the Langmuir isotherm model at pH 5 and Freundlich isotherm model at pH 7 and 9. Its parameters are shown on Table 5.8. The adsorption capacity was also negligible when pH was increased from pH 5 to pH 7 and ultimately pH 9 averaging 57.63 mg/g when selenate concentration was increased from 91.743 mg/L to 366.97 mg/L. The coefficient of determination (R^2) was also higher for Freundlich than the Langmuir isotherm model, indicative of a heterogenous biochar surface, the variability of the adsorbent is observed to be excellent across the pH range tested. The slope (1/n) is favorable for adsorption across the entire pH range, these could be due to the different mechanisms at play because of the different oxides within the biochar matrix (Al-Ghouti & Da'ana, 2020).

Table 5. 8: Selenate adsorption isotherm parameters.

	Freundlich				Langmuir			Sips		
pH	K_F (L/g)	N	R 2	1/n	q_m (mg/g)	R 2	b	β_s	K_s	α_s
5	2.120	0.899	0.923	1.11	-98.03	0.901	-0.006	0.023	1.984	0.865
7	2.527	1.395	0.761	0.72	384.62	0.690	0.003	0.016	10.751	0.708
9	1.811	1.225	0.975	0.82	333.33	0.986	0.003	0.021	1.703	0.884

Based on the data MBC SPS was found to have phosphorus adsorption capacity comparable to and better than other similar biomass-derived biochars: cattle manure (Fe impregnation) (Lee *et al*, 2021), rice straw (grafted chitosan composite) (Zhang *et al*, 2021a), food waste (Fe impregnated) (Hong *et al*, 2020).

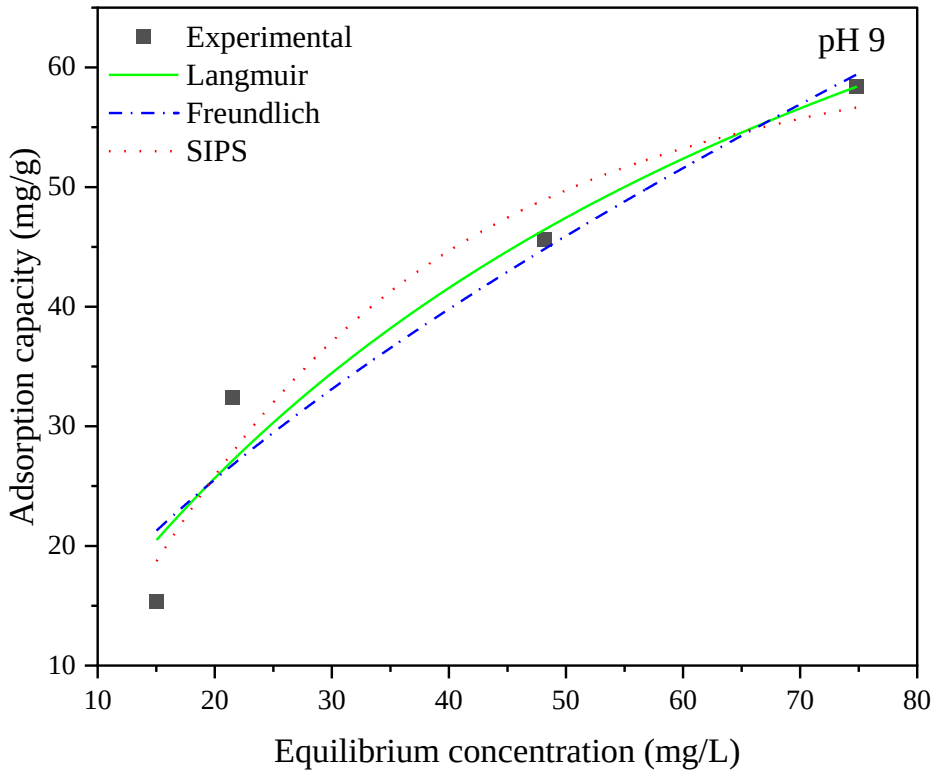

Figure 5. 13: Selenate adsorption isotherms at pH 9

The adsorption of phosphorus by biochar was found to be well described using the Freundlich isotherm model, indicative of a heterogenous biochar adsorption surface.

Table 5. 9: Selenate adsorption isotherm parameters.

	Freundlich			Langmuir			Sips		
pH	K_F (L/g)	N	R 2	q_m (mg/g)	R 2	b	β_s	K_s	α_s
7	1.017	-0.527	0.917	0.964	0.977	-2.856	-0.62	0.456	0.857

5.5.3 Methylene Blue

For methylene blue. The isotherm data points do not exactly follow a linear model as per Figure 5.14, primarily due to multiple sites adsorbing methylene blue, kaolin (Mouni *et al*, 2018; Setthaya *et al*, 2017), TiO_2 (Cai *et al*, 2018; Setthaya *et al*, 2017), Magnetite(Mubarak *et al*, 2015; Yao *et al*, 2020), Biochar functional groups (Ahmed *et al*, 2019; Sun *et al*, 2015) are good adsorbents of methylene blue from solution, hence the isotherm model indicates a complex matrix of adsorption sites on the biochar surface for methylene blue.

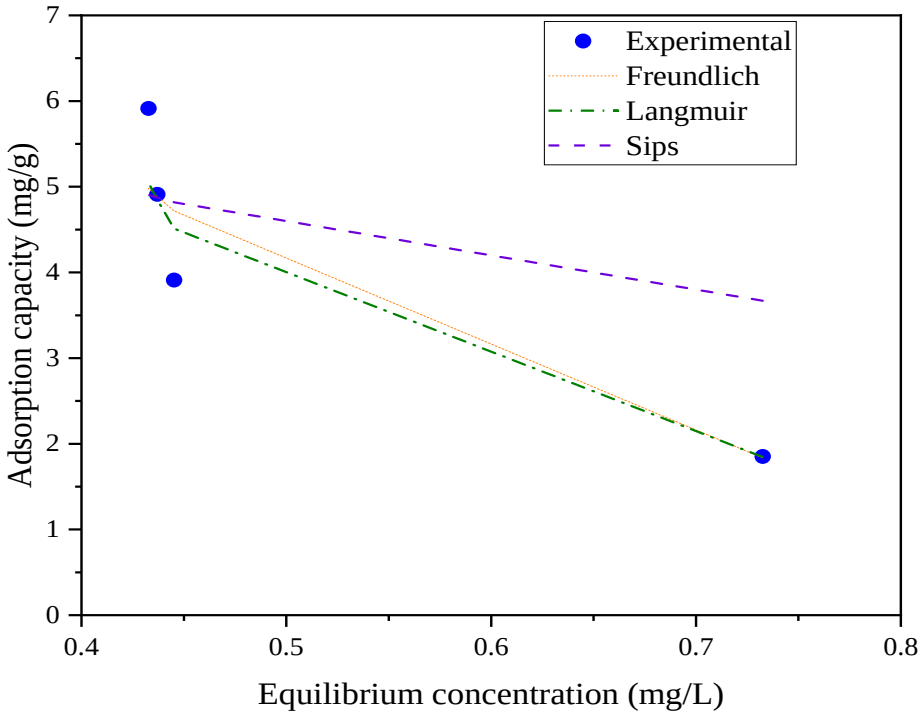

Figure 5. 14: Methylene blue adsorption isotherms

5.6 Adsorption kinetics

Phosphorus, Selenium, and methylene blue adsorption kinetics are plots are shown in Figure 5.15 – 5.17, and the corresponding parameters are indicated in Table 5.10. the kinetics were

found to be best fitted on the Pseudo-Second order model. The adsorption rate constants were found be P- 1.32 x 10^{-3}, Se- 1.29 x 10^{-3} and MB- 57.79 x 10^{-3}. The additional kinetic data and parameters can be found in Appendix F.

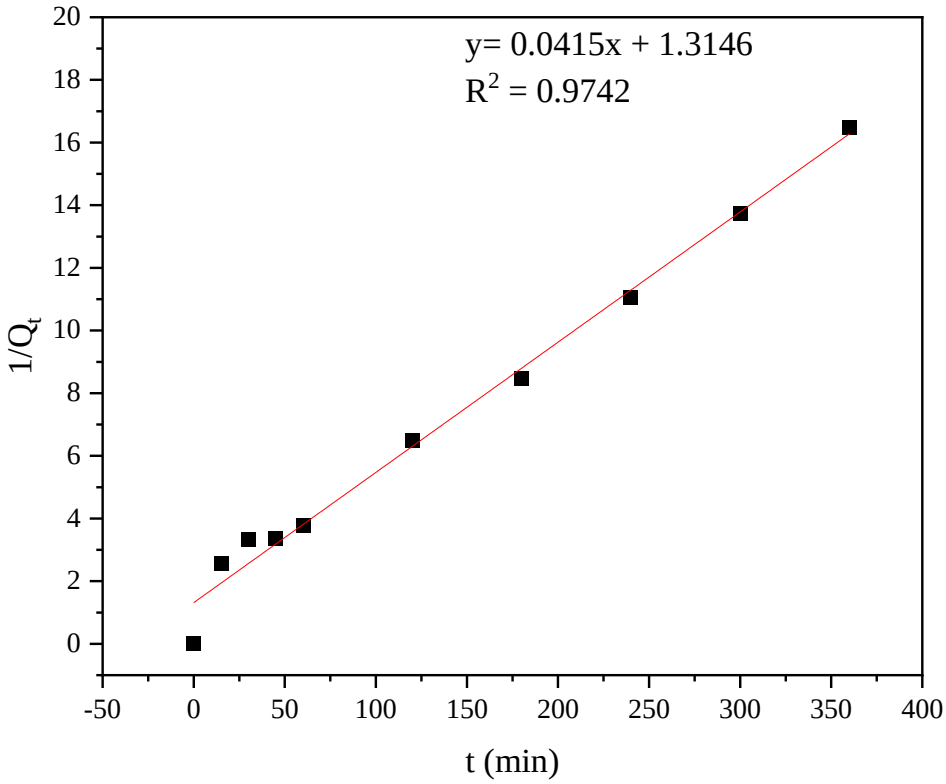

Figure 5. 15: Phosphorus adsorption kinetics (pH 7)

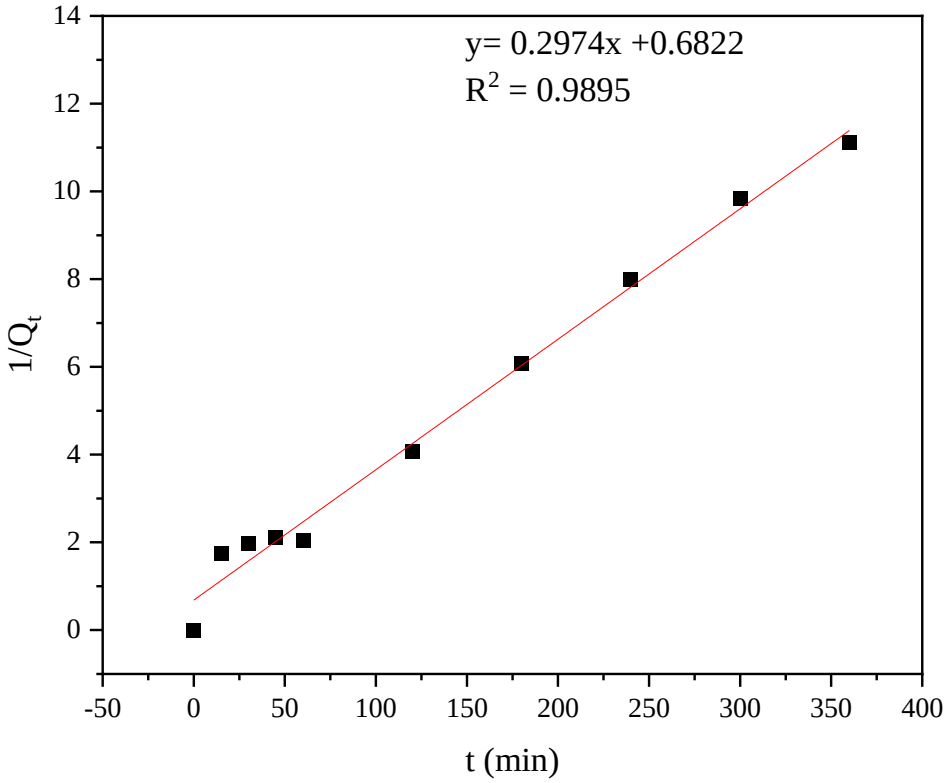

Figure 5. 16: Selenium adsorption kinetics (pH 7)

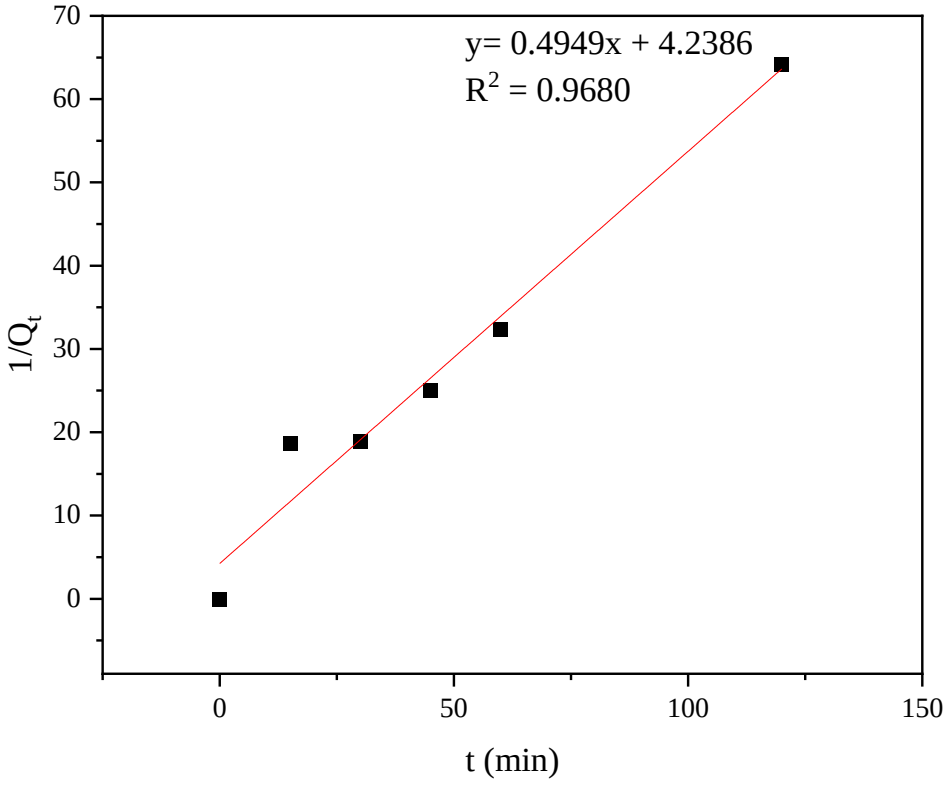

Figure 5. 17: Methylene blue adsorption kinetics (pH 7)

Table 5. 10: Adsorption kinetic model parameters

Adsorbate		Pseudo-First Order			Pseudo-Second Order		
	pH	q_e (L/g)	$K_1 \times 10^{-3}$ (min^{-1})	R 2	q_e (mg/g)	$K_2 \times 10^{-3}$ (g $min^{-1}min^{-1}$)	R 2
P	7	6.220	-0.0183	0.933	24.05	1.32	0.987
Se	7	1.019	3.920	0.913	33.40	1.29	0.99
MB	7	1.310	79.99	0.814	2.02	57.79	0.968

5.7 Regeneration and reusability of Biochar

The emphasis of using RPWS biochar as an adsorbent is to assess its feasibility for use as an adsorbent in wastewater treatment, being part of the recycling process already RPWS derived biochar's reusability is an important measure of its potential. The observed phosphorus adsorption efficiencies for spent biochar after regeneration are encouraging with an efficiency reduction of 13.54 from the first to the third cycle, the fourth cycle efficiencies dropped significantly, this could be due to the loss of Ca^{2+} species and the remaining Fe-P complexes on the magnetite surface.

Selenate efficiencies were reduced by 10.21 % from the first cycle to the third, indicating similar results for phosphorus removal. Methylene blue exhibited a higher reduction of efficiency between the first and third cycle with a reduction of 26.19 % due to the loss of adsorption capacity of kaolin reducing after repeated thermal treatments (Ghosh & Bhattacharyya, 2002). These results show that MBC_SPS biochar can be regenerated and used for three cycles and achieve high efficiencies for phosphorus removal.

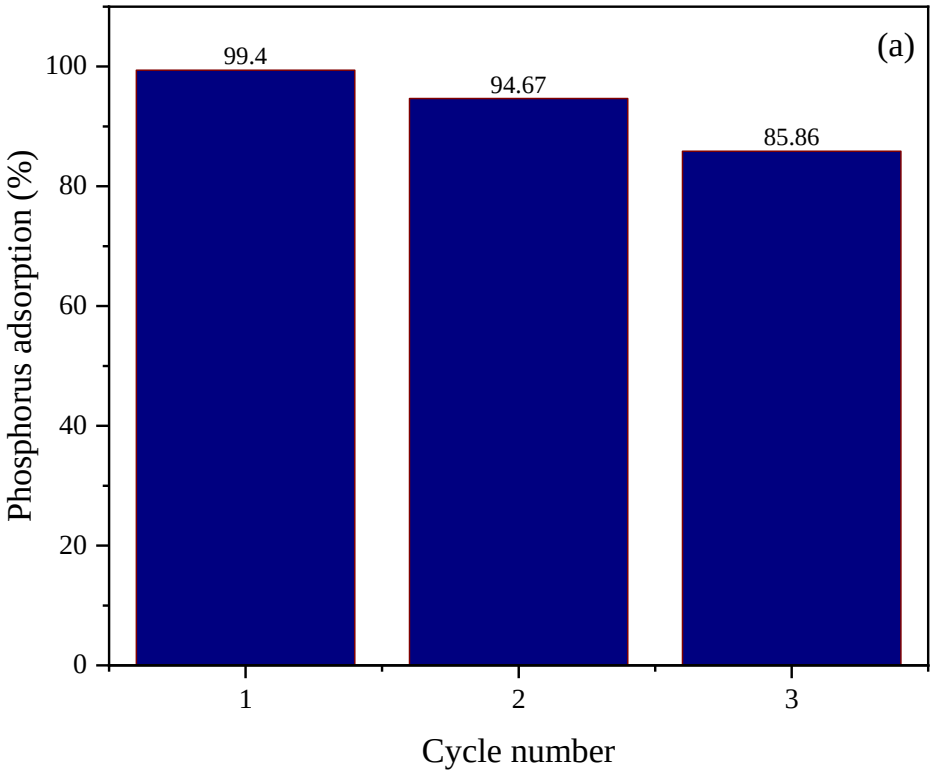
(a)
Phosphorus adsorption (%)
100
80
60
40
20
0
99.4
94.67
85.86
1
2
3
Cycle number

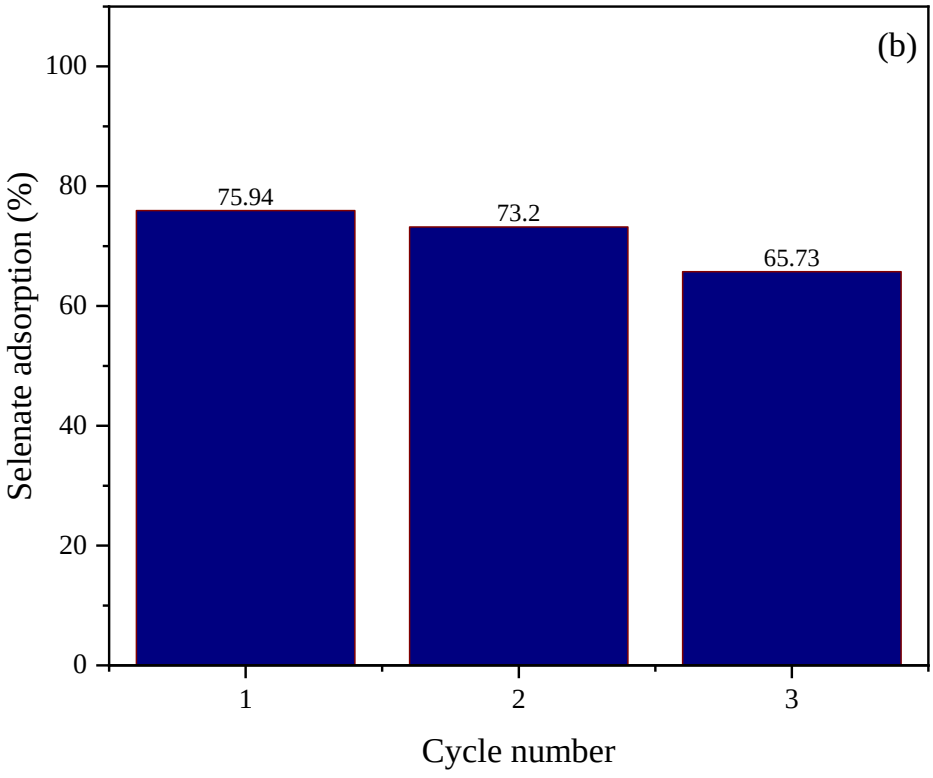
(b)
Selenate adsorption (%)
100
80
60
40
20
0
75.94
73.2
65.73
1
2
3
Cycle number

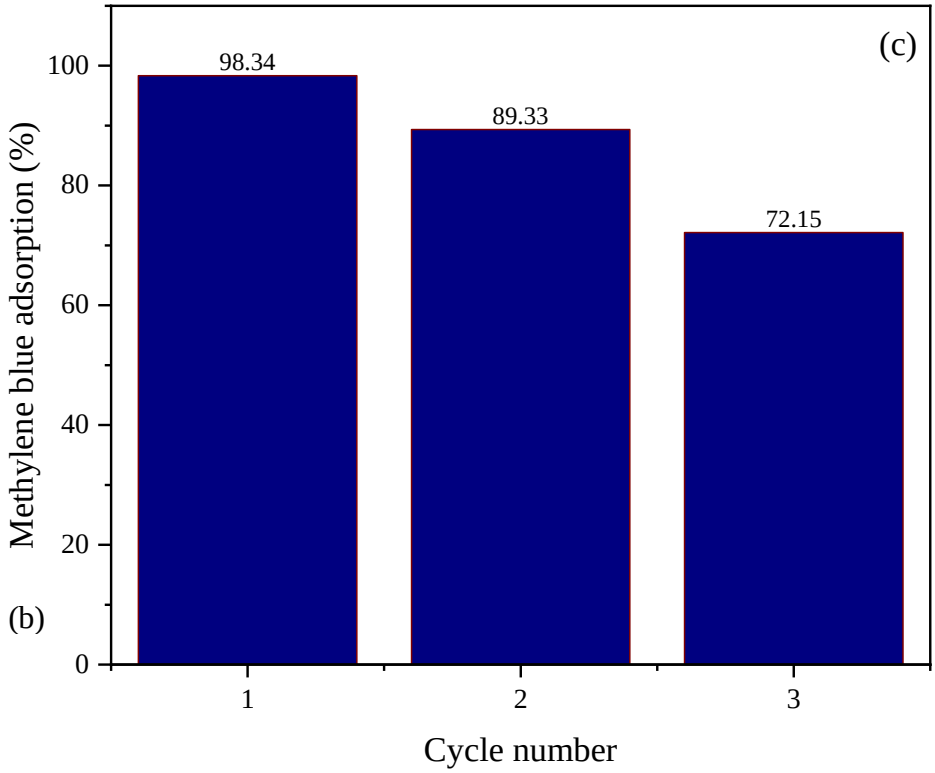

Figure 5. 18: Adsorption efficiencies on regenerated biochar (a) phosphorus, (b) Selenate and (c) Methylene Blue

5.7 Effect of competing ions

The effect of ions competing for sites is an important measure to actively assess an adsorbents usability in practical operations. The results indicate that phosphorus has a higher affinity to the adsorbent surface matrix which resulted in its occupation of more adsorption sites followed by methylene blue and lastly selenate where adsorption efficiency was negligible. The observed efficiencies of $H_2PO_4^{2-}$ (97.54 %) > $C_{16}H_{18}ClN_3S$ (96.36 %) > SeO_4^{2-}(5.96 %) are consistent with studies conducted by (Lee *et al*, 2021; Wei *et al*, 2021) (Yamani *et al*, 2014).

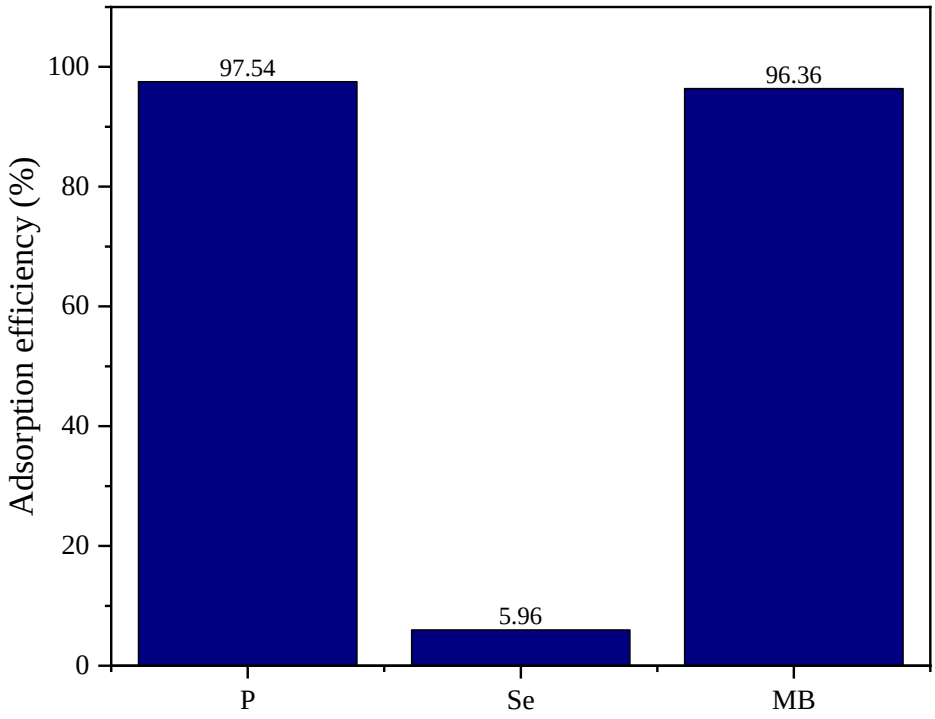

Figure 5. 19: Effect of competition for adsorption sites

Conclusions and recommendations

In this study, the potential of two variants of non-demineralized recycled paper waste sludge (RPWS) as a low-cost alternative adsorbent to activated carbon was assessed for the removal of phosphorus, selenium, and methylene blue. Both variants of the RPWS; Raw paper sludge (RPS) and secondary paper sludge (SPS) were carbonized at 450 °C, 550 °C and 650 °C in an inert environment, an additional step was added to magnetize the resultant biochars by impregnating the feedstock with a 1:1 mol solution of Fe^{2+} and Fe^{3+} and co-pyrolysis. To assess the potential of the resultant pristine and magnetized biochars, several experiments were carried out; such as the characterization of both feedstocks and resultant biochars, phosphorus, selenium, and methylene blue adsorption studies and their kinetics. Determinations of the optimum carbonization temperature and loading were also conducted.

RPS biochar yields were significantly lower than SPS due to the high volatile content in RPS. X-ray diffraction (XRD) analytical technique was used to identify the phases, purity, and crystallinity of the biochars and metal oxides present in the matrix, the results indicated the presence of kaolinite, calcite, talc, and titanium dioxide within the biochar matrix. Clays which other researchers have used as synthesis agents for biochar in adsorption studies, their presence indicating good adsorption potential for the biochar. Well-crystallized magnetite was also identified on the surfaces of these resultant biochars. X-ray fluorescence (XRF) analytical technique was also used to determine the oxides present in the biochar matrix, XRF indicated that the pristine biochars contained on average 16.6 0%, 11.53 %, 1.91 %,12.49 %, and 1.48 %, wt.% of Silica (Si), Aluminum (Al), Magnesium (Mg), Calcium (Ca) and Titanium (Ti) respectively while the magnetized biochars contained an additional 17.46% wt.% Iron (Fe).

Brunauer-Emmet Teller (BET) analytical technique was used to determine the specific surface areas of the resultant biochars, the pristine biochars exhibited higher surface areas while the magnetized variants were 50 % and 56 % lower for SPS and RPS respectively. Scanning Electron Microscopy (SEM) analytical technique was used to assess the morphology of the feedstock and resultant biochars, the biochars exhibited flaky morphology with pore development on the surfaces. The magnetized biochars had clear deposits of magnetite attached to the surfaces, this was further confirmed when Energy Dispersive X-ray Spectroscopy (EDS) and elemental mapping were conducted, the results clearly defined the deposits as well-crystallized magnetite on the surface and in-between the biochar pores.

Transmission Electron Microscopy (TEM) was also performed to Assess the biochar matrix and distribution of the magnetite, results which were consistent with the observations made on SEM that the magnetite was deposited in both the outer surface and in between the pores. The resultant biochar produced promising adsorption efficiencies with MBC SPS chosen as the desirable adsorbent due to its lower cost and high efficiencies when considering upscaling its production. For phosphorus equilibrium was reached within 8h, selenium 12h and methylene blue 6 h with equilibrium best fitting the Freundlich isotherm model for all adsorbates. The maximum adsorption capacities were determined to be 48.83 mg/g, 58.43 mg/g, and 5.92 mg/g for phosphorus, selenium, and methylene blue respectively, capacities which are comparable with other similar adsorbents. Initial solution pH did not affect adsorption capacities, it was hypothesized that this could be due to the presence of clay minerals within the biochar matrix.

The adsorption mechanisms for phosphorus were hypothesized to be complex with complexation, ligand exchange, electrostatic attraction, and precipitation taking part due to the oxides present in the matrix. For selenium the mechanism was hypothesized to be complexation on the surface of the biochar and with kaolinite within the matrix, this was evident in the EDS elemental mapping where Si dominated in the internal sphere and Fe on the outer sphere. The presence of calcium-Silicate-hydrate(C-S-H) phases seemed to dominate the distribution when EDS elemental mapping was performed. Physisorption was hypothesized to be the dominant adsorption mechanism of methylene blue due to hydrogen bonding, π-π interactions, and electrostatic attractions, EDS elemental mapping micrographs indicated the presence of methylene blue on all active sites on the surface of the biochar. The rates of adsorption were determined during a kinetic study and found to be 1.32×10^{-3}, $1.29 \times 10^{-3,}$ and 57.79×10^{-3} for phosphorus, selenium, and methylene blue respectively. The regeneration and reusability study produced good results for three cycles the adsorbent as efficiency only dropped by 10% between runs, this was primarily due to complexes found on the surface of the biochar. The results indicate good adsorption capabilities of RPWS magnetized biochar which has the potential to be upscaled for industrial applications and recycling of nutrients for use in other industries like agriculture.

For future work; it would be important to assess the effect of each individual coating agent (Kaolinite, Titanium dioxide, Calcium Carbonate, and talc) on the adsorption efficiency of RPWS, the recovery of adsorbates is also important when considering the reusability of the biochar. Furthermore, the applicability of spent biochar in soils for condition improvement is another area where spent RPWS biochar could produce positive results.

References

Ahmed, MJ, Okoye, PU, Hummadi, EH, and Hameed, BH (2019), "High-performance porous biochar from the pyrolysis of natural and renewable seaweed (Gelidiella acerosa) and its application for the adsorption of methylene blue" *Bioresource Technology*, 278159-164.

Al-Ghouti, MA, and Da'ana, DA (2020), "Guidelines for the use and interpretation of adsorption isotherm models: A review" *Journal of Hazardous Materials*, 393122383.

Alley, ER (2007), CHEMICAL TREATMENT. *Water Quality Control Handbook, Second Edition*. 2nd ed. New York: McGraw-Hill Education.

Almanassra, IW, McKay, G, Kochkodan, V, Ali Atieh, M, and Al-Ansari, T (2021), "A state of the art review on phosphate removal from water by biochars" *Chemical Engineering Journal*, 409128211.

Almanassra., IW, McKay., G, Kochkodan., V, Ali Atieh., M, and Al-Ansari., T (2021), "A state of the art review on phosphate removal from water by biochars" *Chemical Engineering Journal*, 409.

American Water Works, A, and James, E (2011), ADSORPTION OF ORGANIC COMPOUNDS BY ACTIVATED CARBON. 6th ed. New York: McGraw-Hill Education.
Assis, EI, and Chirwa, EM (2021), "Physicochemical Characteristics of Different Pulp and Paper Mill Waste Streams for Hydrothermal Conversion" *Chemical Engineering Transactions*, 86607-612.

Asuha, S, Fei, F, Wurendaodi, W, Zhao, S, Wu, H, and Zhuang, X (2020), "Activation of kaolinite by a low-temperature chemical method and its effect on methylene blue adsorption" *Powder Technology*, 361624-632.

Bajpai, P (2018), Wood and Fiber Fundamentals. *Biermann's Handbook of Pulp and Paper*.
Balaman, SY (2018), Decision-Making for Biomass-Based Production Chains : The Basic Concepts and Methodologies, Elsevier Science & Technology, San Diego, UNITED STATES.

Basu, P (2018), Biomass Gasification, Pyrolysis and Torrefaction : Practical Design and Theory, Elsevier Science & Technology, San Diego, United States.

Benis, KZ, McPhedran, KN, and Soltan, J (2022), "Selenium removal from water using adsorbents: A critical review" *Journal of Hazardous Materials*, 424127603.

Bhaskar, T, Pandey, A, Mohan, SV, Lee, D-J, and Khanal, SK (2018), Waste Biorefinery : Potential and Perspectives, Elsevier, San Diego, NETHERLANDS, THE.

Bhojappa, S (2009), Removal of phosphorus/selenium from aqueous solutions by adsorption processes, West Virginia University,

Breeze, P (2017), Energy from Waste, Elsevier Science & Technology, London, UNITED KINGDOM.

Brown, LJ, Collard, F-X, and Görgens, J (2017), "Pyrolysis of fibre residues with plastic contamination from a paper recycling mill: Energy recoveries" *Energy Conversion and Management*, 133110-117.

Brown, RC (2019), Thermochemical processing of biomass : conversion into fuels, chemicals and power. Second edition. ed. Hoboken, NJ: John Wiley & Sons Ltd.

Brown, RC, and Wang, K (2014), 1.1 Introduction. *Fast Pyrolysis of Biomass - Advances in Science and Technology*. Royal Society of Chemistry.

Brown, RC, and Wang, K (2017), Fast Pyrolysis of Biomass - Advances in Science and Technology. Royal Society of Chemistry.

Bundy, WM, and Ishley, JN (1991), "Kaolin in paper filling and coating" *Applied Clay Science*, 5(5), 397-420.

Cai, X, Li, J, Liu, Y, Yan, Z, Tan, X, Liu, S, Zeng, G, Gu, Y, Hu, X, and Jiang, L (2018), "Titanium dioxide-coated biochar composites as adsorptive and photocatalytic degradation materials for the removal of aqueous organic pollutants" *Journal of Chemical Technology & Biotechnology*, 93(3), 783-791.

Chen, B, Chen, Z, and Lv, S (2011), "A novel magnetic biochar efficiently sorbs organic pollutants and phosphate" *Bioresour Technol*, 102(2), 716-723.

Chen, YD, Bai, S, Li, R, Su, G, Duan, X, Wang, S, Ren, NQ, and Ho, SH (2019), "Magnetic biochar catalysts from anaerobic digested sludge: Production, application and environment impact" *Environ Int*, 126302-308.

Cheng, N, Wang, B, Feng, Q, Zhang, X, and Chen, M (2021), "Co-adsorption performance and mechanism of nitrogen and phosphorus onto eupatorium adenophorum biochar in water" *Bioresource Technology*, 340125696.

Christensen, ML, Cvitanich, C, Quist-Jensen, CA, Thau, M, and Malmgren-Hansen, B (2021), "Precipitation and recovery of phosphorus from the wastewater hydrolysis tank" *Science of The Total Environment*, 151875.

Ciuta, S, Tsiamis, D, and Castaldi, MJ (2017), Gasification of Waste Materials : Technologies for Generating Energy, Gas, and Chemicals from Municipal Solid Waste, Biomass, Nonrecycled Plastics, Sludges, and Wet Solid Wastes, Elsevier Science & Technology, San Diego, UNITED STATES.

Claverie, M, Dumas, A, Carême, C, Poirier, M, Micoud, P, Martin, F, and Aymonier, C (2018), "Synthetic talc and talc-like structures: preparation, features and applications" *Chemistry-A European Journal*, 24(3), 519-542.

de Azevedo, ARG, Alexandre, J, Pessanha, LSP, Manhaes, R, de Brito, J, and Marvila, MT (2019), "Characterizing the paper industry sludge for environmentally-safe disposal" *Waste Manag*, 9543-52.

Devi, P, and Saroha, AK (2015), "Effect of pyrolysis temperature on polycyclic aromatic hydrocarbons toxicity and sorption behaviour of biochars prepared by pyrolysis of paper mill effluent treatment plant sludge" *Bioresource Technology*, 192312-320.

Dhyani, V, and Bhaskar, T (2019), Pyrolysis of Biomass. *Biofuels: Alternative Feedstocks and Conversion Processes for the Production of Liquid and Gaseous Biofuels.*

Dufour, A (2016), Thermochemical Conversion of Biomass for the Production of Energy and Chemicals, John Wiley & Sons, Incorporated, Hoboken, UNITED STATES.

Fan, Z, Zeng, W, Meng, Q, Liu, H, Liu, H, and Peng, Y (2021), "Achieving enhanced biological phosphorus removal utilizing waste activated sludge as sole carbon source and simultaneous sludge reduction in sequencing batch reactor" *Science of The Total Environment*, 799149291.

Faubert, P, Barnabé, S, Bouchard, S, Côté, R, and Villeneuve, C (2016), "Pulp and paper mill sludge management practices: What are the challenges to assess the impacts on greenhouse gas emissions?" *Resources, Conservation and Recycling*, 108107-133.

Feng, Y, Luo, Y, He, Q, Zhao, D, Zhang, K, Shen, S, and Wang, F (2021a), "Performance and mechanism of a biochar-based Ca-La composite for the adsorption of phosphate from water" *Journal of Environmental Chemical Engineering*, 9(3), 105267.

Feng, Z, Yuan, R, Wang, F, Chen, Z, Zhou, B, and Chen, H (2021b), "Preparation of magnetic biochar and its application in catalytic degradation of organic pollutants: A review" *Sci Total Environ*, 765142673.

Gao, L, and Goldfarb, JL (2021), "Characterization and adsorption applications of composite biochars of clay minerals and biomass" *Environmental Science and Pollution Research*, 1-11.
Gent, S, Twedt, M, Gerometta, C, and Almberg, E (2017), Theoretical and Applied Aspects of Biomass Torrefaction : For Biofuels and Value-Added Products, Elsevier Science & Technology, Oxford, UNITED STATES.

Ghosh, D, and Bhattacharyya, KG (2002), "Adsorption of methylene blue on kaolinite" *Applied Clay Science*, 20(6), 295-300.

Godlewska, P, Bogusz, A, Dobrzyńska, J, Dobrowolski, R, and Oleszczuk, P (2020), "Engineered biochar modified with iron as a new adsorbent for treatment of water contaminated by selenium" *Journal of Saudi Chemical Society*, 24(11), 824-834.

Guo, B, Tian, Q, Oji, T, Wang, L, and Sasaki, K (2021), "Effects of Mg compounds in hydroxylated calcined dolomite as an effective and sustainable substitute of lime to precipitate as ettringite for treatment of selenite/selenate in aqueous solution" *Colloids and Surfaces A: Physicochemical and Engineering Aspects*, 610125782.

Han, H, Rafiq, MK, Zhou, T, Xu, R, Mašek, O, and Li, X (2019), "A critical review of clay-based composites with enhanced adsorption performance for metal and organic pollutants" *Journal of Hazardous Materials*, 369780-796.

Hernandez-Maldonado, A, and Blaney, L (2019), Contaminants of Emerging Concern in Water and Wastewater : Advanced Treatment Processes, Elsevier Science & Technology, San Diego, UNITED STATES.

Hong, S-H, Lyonga, FN, Kang, J-K, Seo, E-J, Lee, C-G, Jeong, S, Hong, S-G, and Park, S-J (2020), "Synthesis of Fe-impregnated biochar from food waste for Selenium(VI) removal from aqueous solution through adsorption: Process optimization and assessment" *Chemosphere*, 252126475.

Hornung, A (2014), Transformation of Biomass : Theory to Practice, John Wiley & Sons, Incorporated, New York, UNITED KINGDOM.

Lee, N, Hong, S-H, Lee, C-G, Park, S-J, and Lee, J (2021), "Conversion of cattle manure into functional material to remove selenate from wastewater" *Chemosphere*, 278130398.

Li, R, Wang, JJ, Zhou, B, Awasthi, MK, Ali, A, Zhang, Z, Lahori, AH, and Mahar, A (2016a), "Recovery of phosphate from aqueous solution by magnesium oxide decorated magnetic biochar and its potential as phosphate-based fertilizer substitute" *Bioresour Technol*, 215209-214.

Li, R, Wang, JJ, Zhou, B, Awasthi, MK, Ali, A, Zhang, Z, Lahori, AH, and Mahar, A (2016b), "Recovery of phosphate from aqueous solution by magnesium oxide decorated magnetic biochar and its potential as phosphate-based fertilizer substitute" *Bioresource Technology*, 215209-214.

Li, X, Xie, Y, Jiang, F, Wang, B, Hu, Q, Tang, Y, Luo, T, and Wu, T (2020), "Enhanced phosphate removal from aqueous solution using resourceable nano-CaO2/BC composite: Behaviors and mechanisms" *Science of The Total Environment*, 709136123.

Liu, H, Chen, P, and Chen, Z (2015), "Role of influent split ratio in a two-line BNR process performing denitrifying phosphorus removal" *Chemical Engineering Journal*, 267266-273.
Loan, TT, Huong, VH, Huyen, NT, Van Quyet, L, Bang, NA, and Long, NN (2021), "Anatase to rutile phase transformation of iron-doped titanium dioxide nanoparticles: The role of iron content" *Optical Materials*, 111110651.

Mak, S-Y, and Chen, D-H (2004), "Fast adsorption of methylene blue on polyacrylic acid-bound iron oxide magnetic nanoparticles" *Dyes and Pigments*, 61(1), 93-98.
Manuel, G-P (2010), Biomass Pyrolysis and Bio-Oil Refineries. New York: McGraw-Hill Education.

Manya, JJ (2012), "Pyrolysis for biochar purposes: a review to establish current knowledge gaps and research needs" *Environ Sci Technol*, 46(15), 7939-7954.

Marche, T, Schnitzer, M, Dinel, H, Paré, T, Champagne, P, Schulten, HR, and Facey, G (2003), "Chemical changes during composting of a paper mill sludge–hardwood sawdust mixture" *Geoderma*, 116(3), 345-356.

Méndez, A, Fidalgo, JM, Guerrero, F, and Gascó, G (2009), "Characterization and pyrolysis behaviour of different paper mill waste materials" *Journal of Analytical and Applied Pyrolysis*, 86(1), 66-73.

Michálešková-Richveisová, B, Frišták, V, Pipíška, M, Ďuriška, L, Moreno-Jimenez, E, and Soja, G (2017), "Iron-impregnated biochars as effective phosphate sorption materials" *Environmental Science and Pollution Research*, 24(1), 463-475.

Missana, T, García-Gutiérrez, M, Mingarro, M, and Alonso, U (2019), "Selenite Retention and Cation Coadsorption Effects under Alkaline Conditions Generated by Cementitious Materials: The Case of C–S–H Phases" *ACS Omega*, 4(8), 13418-13425.

Miyazato, T, Nuryono, N, Kobune, M, Rusdiarso, B, Otomo, R, and Kamiya, Y (2020), "Phosphate recovery from an aqueous solution through adsorption-desorption cycle over thermally treated activated carbon" *Journal of Water Process Engineering*, 36101302.

Mohammadi, H, Nekobahr, E, Akhtari, J, Saeedi, M, Akbari, J, and Fathi, F (2021), "Synthesis and characterization of magnetite nanoparticles by co-precipitation method coated with biocompatible compounds and evaluation of in-vitro cytotoxicity" *Toxicology Reports*, 8331-336.

Mohammed, I, Afagwu, CC, Adjei, S, Kadafur, IB, Jamal, MS, and Awotunde, AA (2020), "A review on polymer, gas, surfactant and nanoparticle adsorption modeling in porous media" *Oil & Gas Science and Technology–Revue d'IFP Energies nouvelles*, 7577.

Monte, MC, Fuente, E, Blanco, A, and Negro, C (2009), "Waste management from pulp and paper production in the European Union" *Waste Manag*, 29(1), 293-308.

Morrissey, A (2020), Treatment and Recycling of Domestic and Industrial Wastewater. *In:* Hashmi, S, and Choudhury, IA (eds.) *Encyclopedia of Renewable and Sustainable Materials.* Oxford: Elsevier.

Mouni, L, Belkhiri, L, Bollinger, J-C, Bouzaza, A, Assadi, A, Tirri, A, Dahmoune, F, Madani, K, and Remini, H (2018), "Removal of Methylene Blue from aqueous solutions by adsorption on Kaolin: Kinetic and equilibrium studies" *Applied Clay Science*, 15338-45.

Mozaffari Majd, M, Kordzadeh-Kermani, V, Ghalandari, V, Askari, A, and Sillanpää, M (2021), "Adsorption isotherm models: A comprehensive and systematic review (2010–2020)" *Science of The Total Environment*, 151334.

Mu, Y, Du, H, He, W, and Ma, H (2022), "Functionalized mesoporous magnetic biochar for methylene blue removal: Performance assessment and mechanism exploration" *Diamond and Related Materials*, 121108795.

Mubarak, NM, Fo, YT, Al-Salim, HS, Sahu, JN, Abdullah, EC, Nizamuddin, S, Jayakumar, NS, and Ganesan, P (2015), "Removal of Methylene Blue and Orange-G from Waste Water Using Magnetic Biochar" *International Journal of Nanoscience*, 14(04), 1550009.

Mussoline, W, Esposito, G, Lens, P, Spagni, A, and Giordano, A (2013), "Enhanced methane production from rice straw co-digested with anaerobic sludge from pulp and paper mill treatment process" *Bioresource Technology*, 148135-143.

Naushad, M, and Al-Othman, ZA (2013), A book on ion exchange, adsorption and solvent extraction. Hauppauge, New York: Nova Science Publishers, Incorporated.

Nguyen, LH, Van, HT, Chu, THH, Nguyen, THV, Nguyen, TD, Hoang, LP, and Hoang, VH (2020), "Paper waste sludge-derived hydrochar modified by iron (III) chloride for enhancement of ammonium adsorption: An adsorption mechanism study" *Environmental Technology & Innovation*.

Ok, YS, Tsang, DCW, Bolan, N, and Novak, JM (2018), Biochar from Biomass and Waste : Fundamentals and Applications, Elsevier, San Diego, UNITED STATES.
Pamsa (2019), "2019 PAMSA-Annual-report".

Pandey, A, Bhaskar, T, Stöcker, M, and Sukumaran, RK (2015), 1.3.2 Components of Lignocellulosic Biomass. *Recent Advances in Thermochemical Conversion of Biomass*. Elsevier.

Pandey, A, Larroche, C, Gnansounou, E, Khanal, SK, Dussap, C-G, and Ricke, S (2019), Biomass, Biofuels, Biochemicals : Biofuels: Alternative Feedstocks and Conversion Processes for the Production of Liquid and Gaseous Biofuels, Elsevier Science & Technology, San Diego, UNITED STATES.

Pei, L, Yang, F, Xu, X, Nan, H, Gui, X, Zhao, L, and Cao, X (2021), "Further reuse of phosphorus-laden biochar for lead sorption from aqueous solution: Isotherm, kinetics, and mechanism" *Science of The Total Environment*, 792148550.

Perez-Mercado, L, Lalander, C, Berger, C, and Dalahmeh, S (2018), "Potential of Biochar Filters for Onsite Wastewater Treatment: Effects of Biochar Type, Physical Properties and Operating Conditions" *Water*, 10(12).

Ragauskas, AJ (2014), Materials for Biofuels, World Scientific Publishing Co Pte Ltd, Singapore, UNITED STATES.

Rida, K, Bouraoui, S, and Hadnine, S (2013), "Adsorption of methylene blue from aqueous solution by kaolin and zeolite" *Applied Clay Science*, 83-8499-105.

Ridout, AJ, Carrier, M, Collard, F-X, and Görgens, J (2016), "Energy conversion assessment of vacuum, slow and fast pyrolysis processes for low and high ash paper waste sludge" *Energy Conversion and Management*, 111103-114.

Ridout, AJ, Carrier, M, and Görgens, J (2015), "Fast pyrolysis of low and high ash paper waste sludge: Influence of reactor temperature and pellet size" *Journal of Analytical and Applied Pyrolysis*, 11164-75.

Sahoo, SS, Vijay, VK, Chandra, R, and Kumar, H (2021), "Production and characterization of biochar produced from slow pyrolysis of pigeon pea stalk and bamboo" *Cleaner Engineering and Technology*, 3100101.

Setthaya, N, Chindaprasirt, P, Yin, S, and Pimraksa, K (2017), "TiO2-zeolite photocatalysts made of metakaolin and rice husk ash for removal of methylene blue dye" *Powder Technology*, 313417-426.

Singh, RK, Ruj, B, Sadhukhan, AK, and Gupta, P (2019), "Impact of fast and slow pyrolysis on the degradation of mixed plastic waste: Product yield analysis and their characterization" *Journal of the Energy Institute*, 92(6), 1647-1657.

Sinharoy, A, and Lens, PNL (2020), "Biological Removal of Selenate and Selenite from Wastewater: Options for Selenium Recovery as Nanoparticles" *Current Pollution Reports*, 6(3), 230-249.

Souza, R, Navarro, R, Grillo, AV, and Brocchi, E (2019), "Potassium alum thermal decomposition study under non-reductive and reductive conditions" *Journal of Materials Research and Technology*, 8(1), 745-751.

Strezov, V, Patterson, M, Zymla, V, Fisher, K, Evans, TJ, and Nelson, PF (2007), "Fundamental aspects of biomass carbonisation" *Journal of Analytical and Applied Pyrolysis*, 79(1-2), 91-100.

Sun, J, Liu, X, Duan, S, Alsaedi, A, Zhang, F, Hayat, T, and Li, J (2018), "The influential factors towards graphene oxides removal by activated carbons: Activated functional groups vs BET surface area" *Journal of Molecular Liquids*, 271142-150.

Sun, L, Chen, D, Wan, S, and Yu, Z (2015), "Performance, kinetics, and equilibrium of methylene blue adsorption on biochar derived from eucalyptus saw dust modified with citric, tartaric, and acetic acids" *Bioresource Technology*, 198300-308.

Tabana, L, Tichapondwa, S, Labuschagne, F, and Chirwa, E (2020), "Adsorption of phenol from wastewater using calcined magnesium-zinc-aluminium layered double hydroxide clay" *Sustainability*, 12(10), 4273.

Tawalbeh, M, Rajangam, AS, Salameh, T, Al-Othman, A, and Alkasrawi, M (2021), "Characterization of paper mill sludge as a renewable feedstock for sustainable hydrogen and biofuels production" *International Journal of Hydrogen Energy*, 46(6), 4761-4775.
Thakur, VK, Thakur, MK, and Kessler, MR (2017), Handbook of Composites from Renewable Materials, Nanocomposites : Science and Fundamentals, John Wiley & Sons, Incorporated, Somerset, UNITED STATES.

Tian, Q, Chen, C, Wang, M, Guo, B, Zhang, H, and Sasaki, K (2021), "Effect of Si/Al molar ratio on the immobilization of selenium and arsenic oxyanions in geopolymer" *Environmental Pollution*, 274116509.

Varga, G (2007), "The structure of kaolinite and metakaolinite" *Epitoanyag*, 59(1), 6-9.

Vedula, SS, and Yadav, GD (2022), "Wastewater treatment containing methylene blue dye as pollutant using adsorption by chitosan lignin membrane: Development of membrane, characterization and kinetics of adsorption" *Journal of the Indian Chemical Society*, 99(1), 100263.

Veluchamy, C, Raju, VW, and Kalamdhad, AS (2018), "Electrohydrolysis pretreatment for enhanced methane production from lignocellulose waste pulp and paper mill sludge and its kinetics" *Bioresource Technology*, 25252-58.

Wang, B, Xu, F, Zong, P, Zhang, J, Tian, Y, and Qiao, Y (2019a), "Effects of heating rate on fast pyrolysis behavior and product distribution of Jerusalem artichoke stalk by using TG-FTIR and Py-GC/MS" *Renewable Energy*, 132486-496.

Wang, J, Kou, L, Zhao, L, and Duan, W (2020a), "One-pot fabrication of sludge-derived magnetic Fe,N-codoped carbon catalysts for peroxymonosulfate-induced elimination of phenolic contaminants" *Chemosphere*, 248.

Wang, S, and Luo, Z (2016), 7. Pyrolysis of biomass. *Pyrolysis of Biomass*. De Gruyter.
Wang, S, Luo, Z, China Science, P, and Media Ltd, CS (2016a), Pyrolysis of Biomass, De Gruyter, Inc., Berlin/Boston, GERMANY.

Wang, S, Luo, Z, China Science, P, and Media Ltd, S (2016b), Pyrolysis of Biomass, De Gruyter, Inc., Berlin/Boston, GERMANY.

Wang, S, Shi, R, Li, H, Li, Y, Xu, Y, and Han, Z (2020b), "Effect of terminal temperature on the morphology and potentially toxic metals concentrations of biochars derived from paper and kitchen waste" *Waste Management*, 118445-451.

Wang, S, Zhao, M, Zhou, M, Zhao, Y, Li, YC, Gao, B, Feng, K, Yin, W, Ok, YS, and Wang, X (2019b), "Biomass facilitated phase transformation of natural hematite at high temperatures and sorption of Cd(2+) and Cu(2)" *Environ Int*, 124473-481.

Wang, Z, Miao, R, Ning, P, He, L, and Guan, Q (2021), "From wastes to functions: A paper mill sludge-based calcium-containing porous biochar adsorbent for phosphorus removal" *Journal of Colloid and Interface Science*, 593434-446.

Wei, X, Li, X, Tang, L, Yu, J, Deng, J, Luo, T, Liang, J, Chen, X, and Zhou, Y (2021), "Exploring the role of Fe species from biochar-iron composites in the removal and long-term immobilization of SeO42- against competing oxyanions" *Journal of Hazardous Materials*, 418126311.

Worch, E (2012), Adsorption Technology in Water Treatment : Fundamentals, Processes, and Modeling, De Gruyter, Inc., Berlin/Boston, GERMANY.

Xiang, W, Zhang, X, Chen, J, Zou, W, He, F, Hu, X, Tsang, DCW, Ok, YS, and Gao, B (2020), "Biochar technology in wastewater treatment: A critical review" *Chemosphere*, 252126539.

Xu, Z, Lin, Y, Lin, Y, Yang, D, and Zheng, H (2021), "Adsorption behaviors of paper mill sludge biochar to remove Cu, Zn and As in wastewater" *Environmental Technology & Innovation*, 23101616.

Yaashikaa, PR, Kumar, PS, Varjani, S, and Saravanan, A (2020), "A critical review on the biochar production techniques, characterization, stability and applications for circular bioeconomy" *Biotechnol Rep (Amst)*, 28e00570.

Yamani, JS, Lounsbury, AW, and Zimmerman, JB (2014), "Adsorption of selenite and selenate by nanocrystalline aluminum oxide, neat and impregnated in chitosan beads" *Water Research*, 50373-381.

Yang, H, Ye, S, Zeng, Z, Zeng, G, Tan, X, Xiao, R, Wang, J, Song, B, Du, L, Qin, M, Yang, Y, and Xu, F (2020), "Utilization of biochar for resource recovery from water: A review" *Chemical Engineering Journal*, 397.

Yao, X, Ji, L, Guo, J, Ge, S, Lu, W, Cai, L, Wang, Y, Song, W, and Zhang, H (2020), "Magnetic activated biochar nanocomposites derived from wakame and its application in methylene blue adsorption" *Bioresour Technol*, 302122842.

Zhang, L, Jiang, SC, and Guan, Y (2021a), "Efficient removal of selenate in water by cationic poly(allyltrimethylammonium) grafted chitosan and biochar composite" *Environmental Research*, 194110667.

Zhang, P, O'Connor, D, Wang, Y, Jiang, L, Xia, T, Wang, L, Tsang, DCW, Ok, YS, and Hou, D (2020), "A green biochar/iron oxide composite for methylene blue removal" *Journal of Hazardous Materials*, 384121286.

Zhang, R, Fan, Y, Wang, L, Li, J, Li, H, Shi, Y, and Pan, D (2021b), "Rapid adsorption of phosphorus at low concentration from water using a novel green organometallic material EGCG-Fe" *Journal of Environmental Chemical Engineering*, 9(5), 106242.

APPENDICES

Characterization

Appendix A: XRD patterns

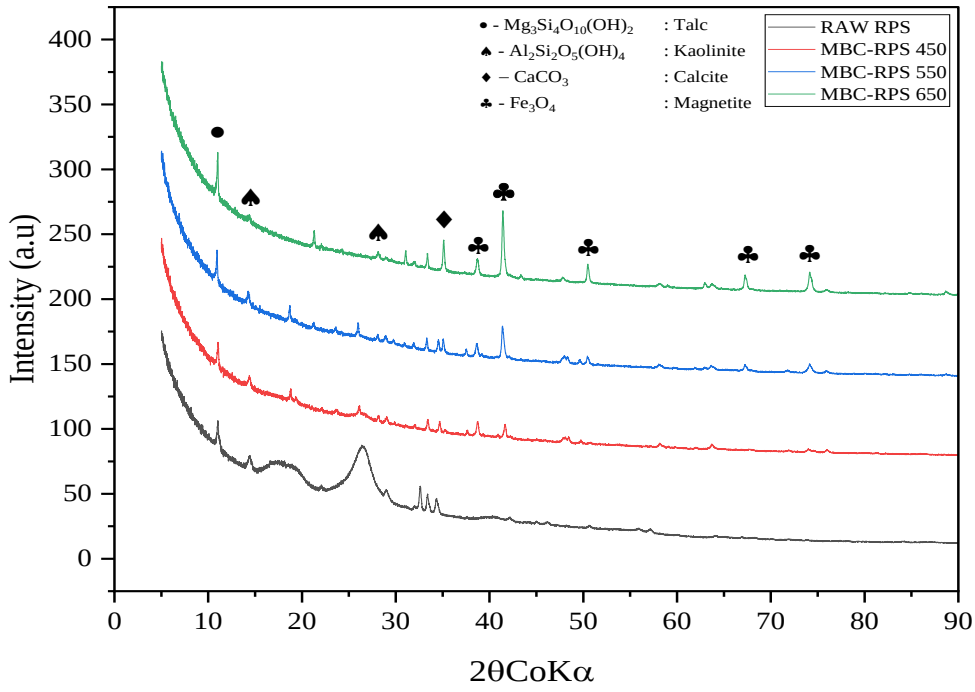

Appendix A- 1: XRD Plot MBC RPS

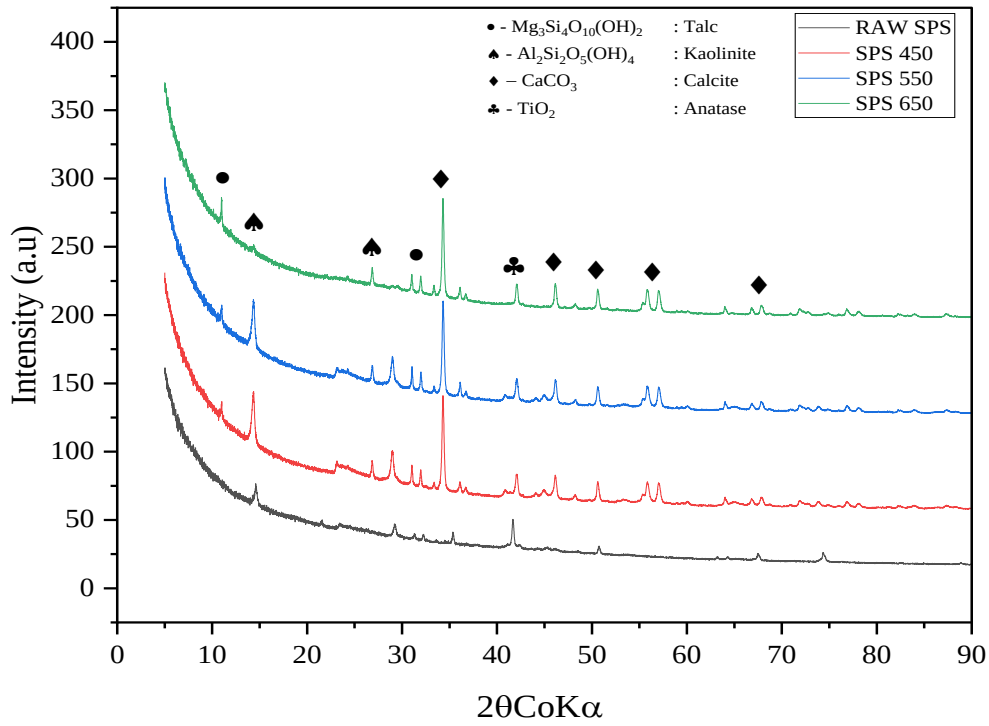

Appendix A- 2: XRD Plot SPS

Appendix B: FTIR Spectra

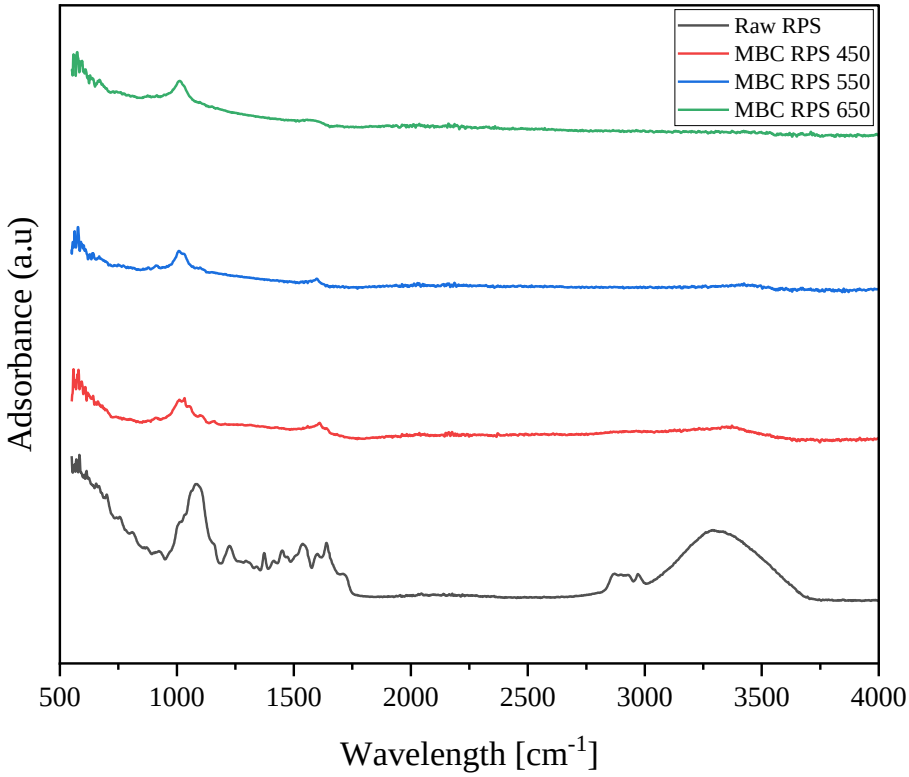

Appendix B- 1: FTIR spectra of MBC-RPS

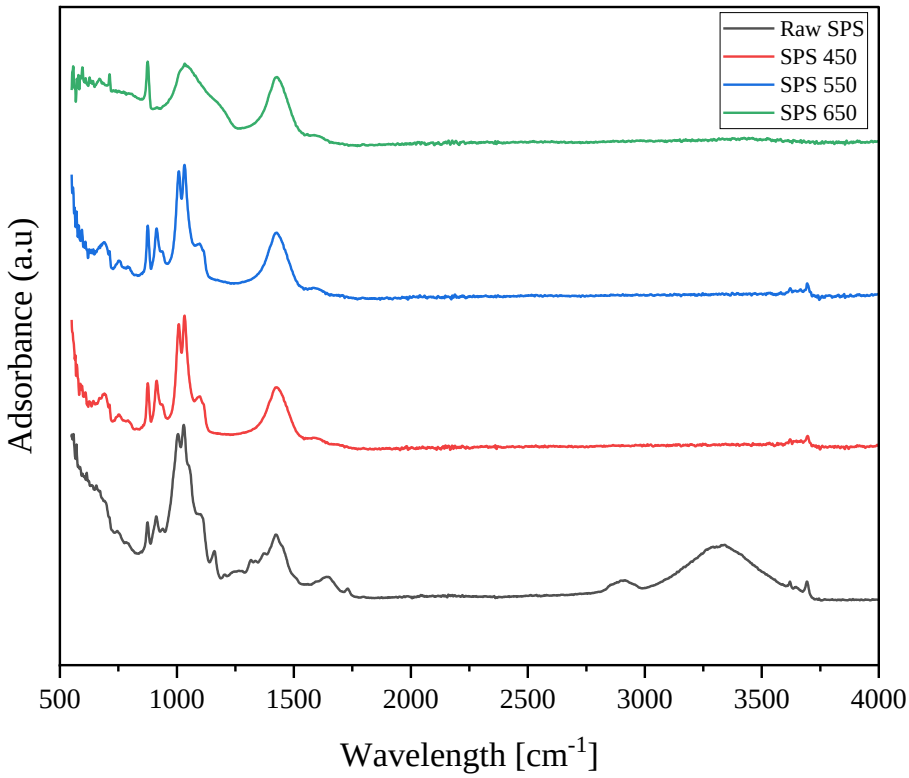

Appendix B- 2: FTIR spectra of SPS

Appendix C: SEM micrographs

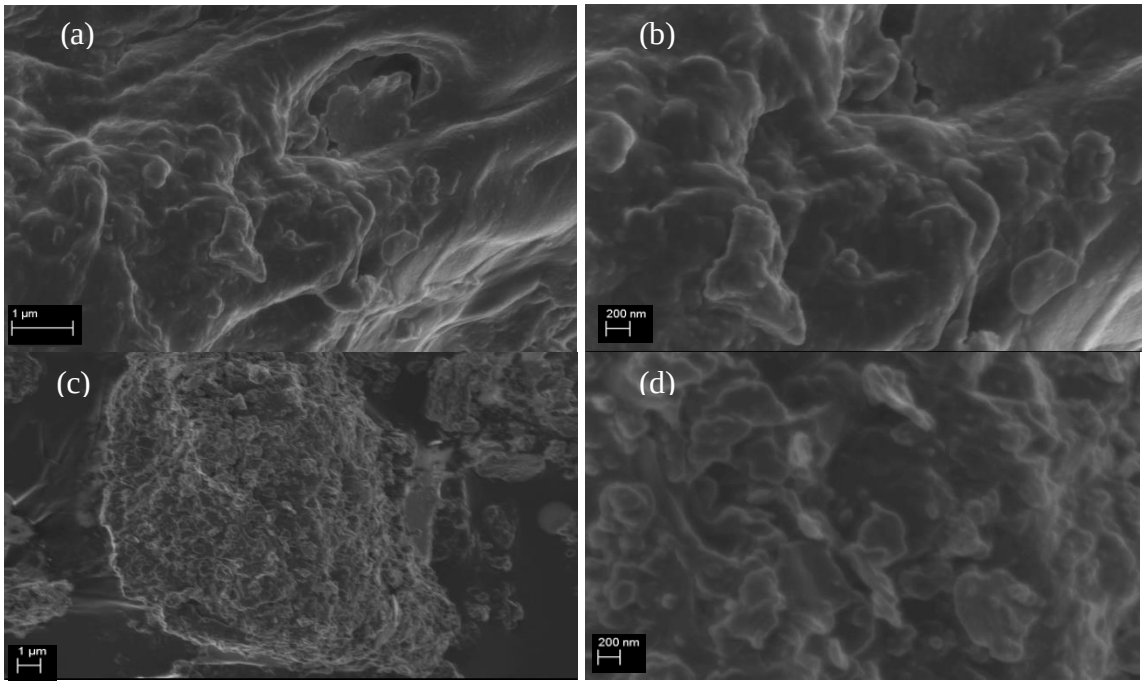

Appendix C- 1: SEM images of resultant synthesized 450ºC biochar (a) MBC-RPS at 2µ magnification, (b) MBC-RPS at 200µ magnification, (c) MBC-SPS at 2µ magnification, (d) MBC-SPS at 200µ magnification

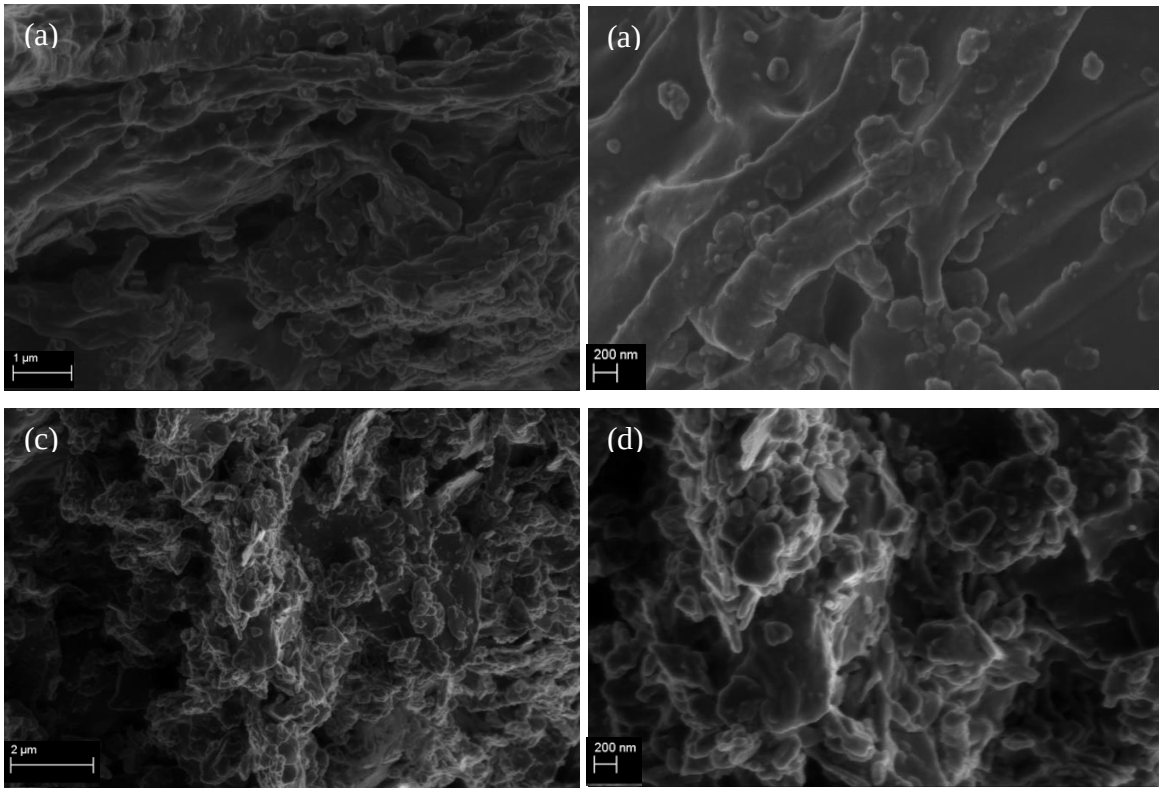

Appendix C- 2: SEM images of resultant 550ºC pristine biochar (a) RPS at 2µ magnification, (b) RPS at 200µ magnification, (c) SPS at 2µ magnification, (d) SPS at 200µ magnification

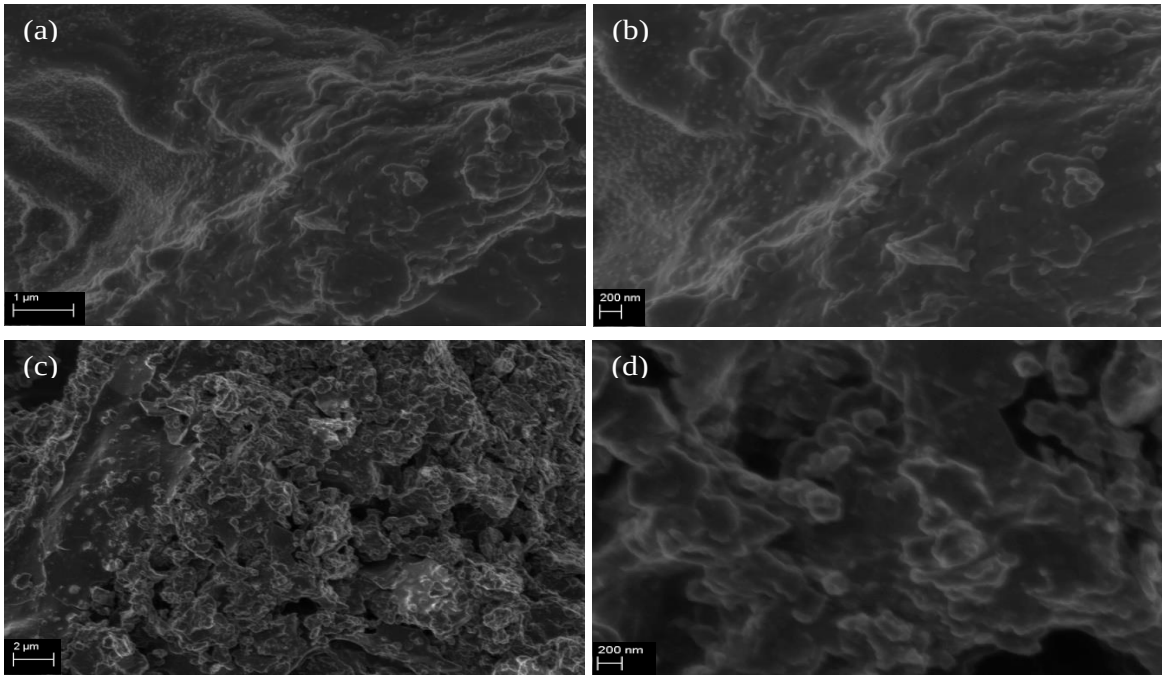

Appendix C- 3: SEM images of resultant 550°C synthesized biochar (a) RPS at 2µ magnification, (b) RPS at 200µ magnification, (c) SPS at 2µ magnification, (d) SPS at 200µ magnification

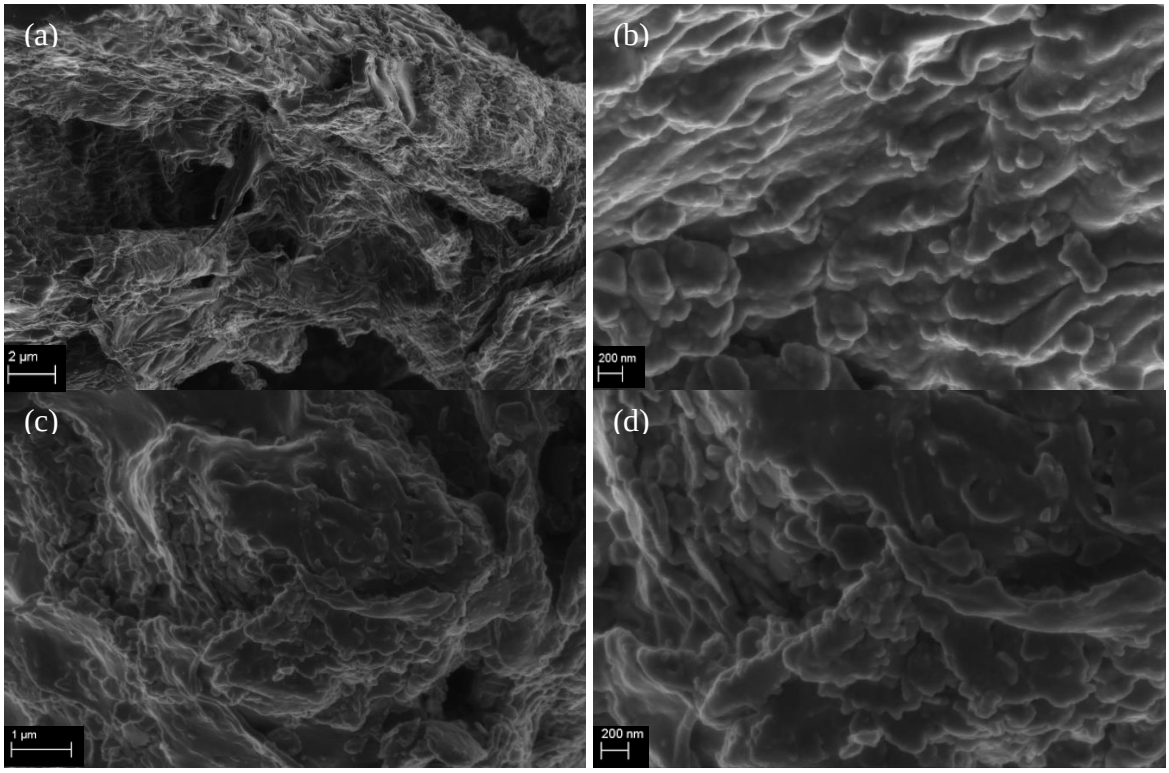

Appendix C- 4: SEM images of resultant 650°C pristine biochar (a) RPS at 2µ magnification, (b) RPS at 200µ magnification, (c) SPS at 2µ magnification, (d) SPS at 200µ magnification

Appendix D: EDS Spectra and elemental mapping

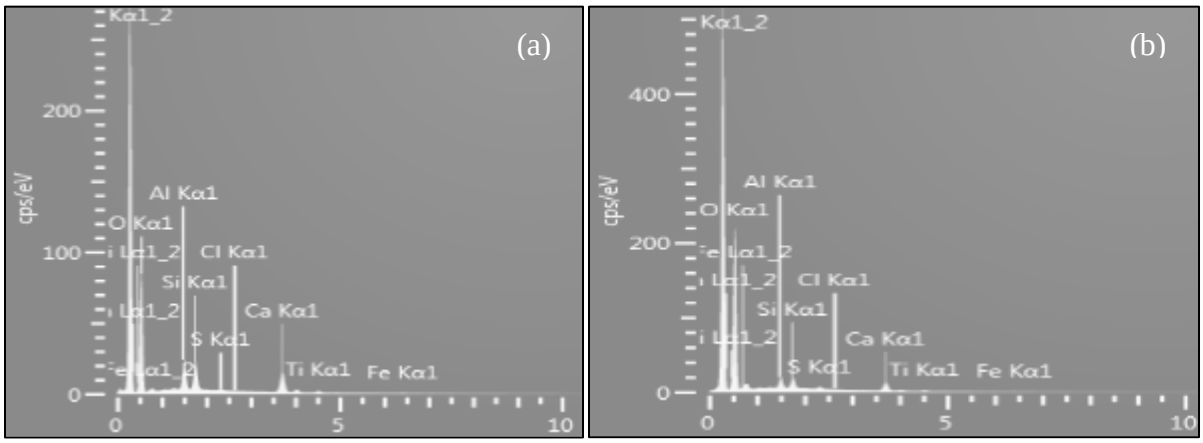

Appendix D - 1: EDS Spectra of RPWS (a) SPS and (b) RPS**.**

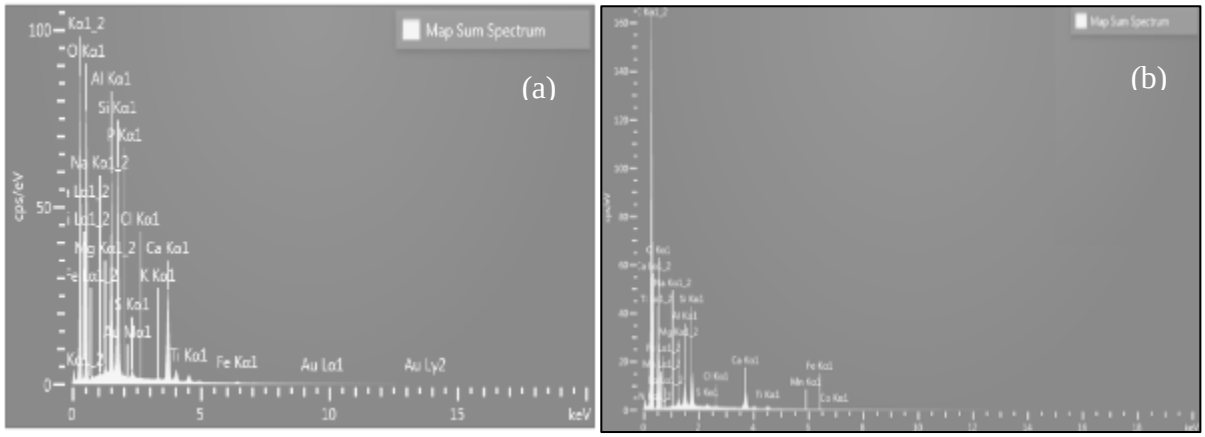

Appendix D - 2: EDS Spectra of 450 ºC pristine biochar (a) SPS and (b) RPS

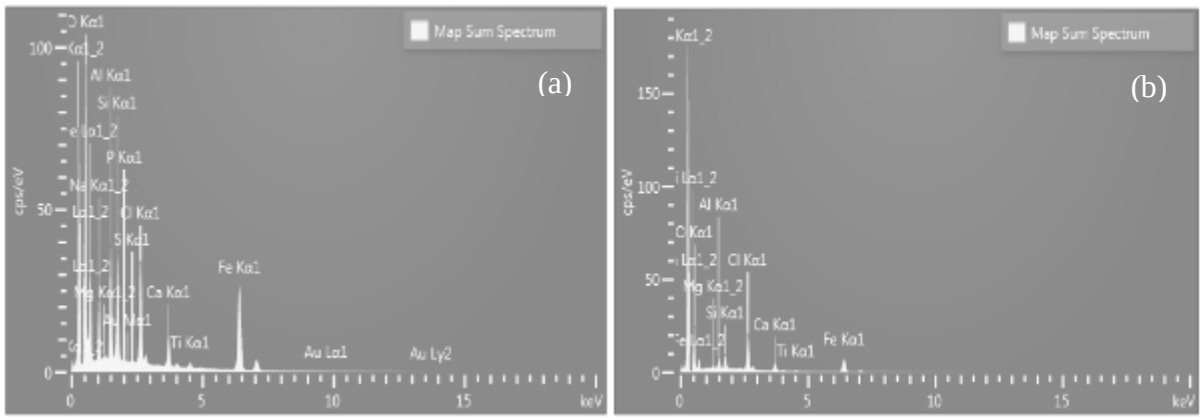

Appendix D - 3: Elemental mapping of 650 ºC synthesized biochar (a) SPS and (b) RPS.

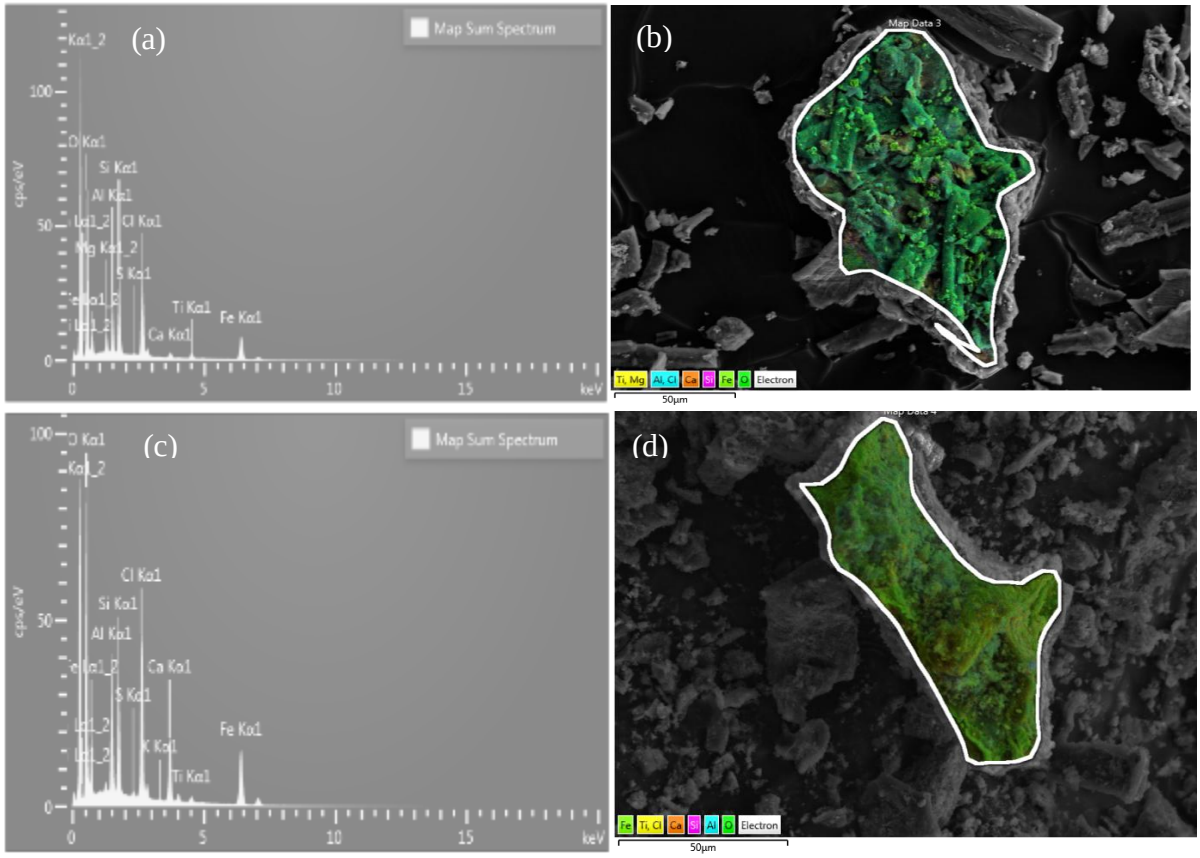

Appendix D - 4: EDS spectra and elemental mapping micrographs of resultant MBC 450ºC biochar (a) RPS spectra, (b) RPS elemental map, (c) SPS spectra, (d) SPS elemental map

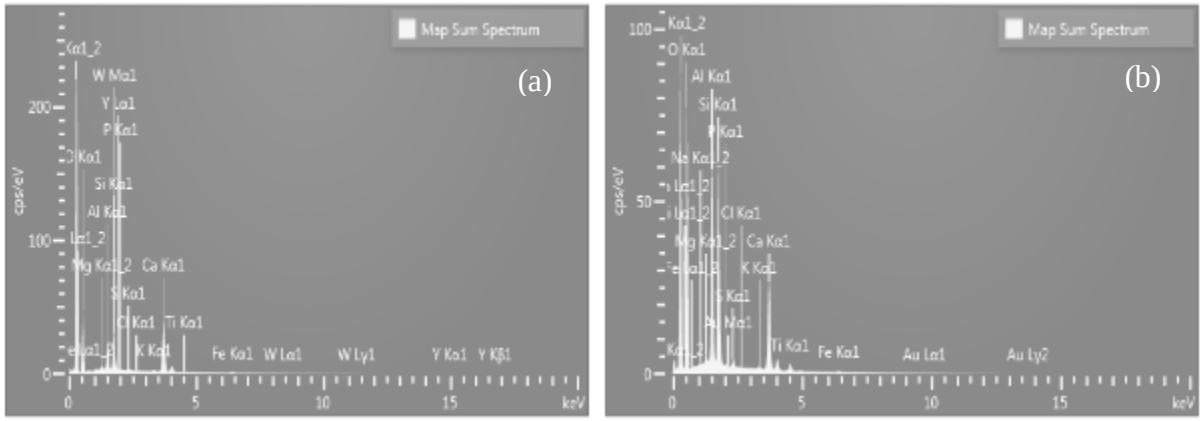

Appendix D - 5: EDS spectra of resultant pristine 550ºC biochar (a) RPS spectra and (b) SPS spectra

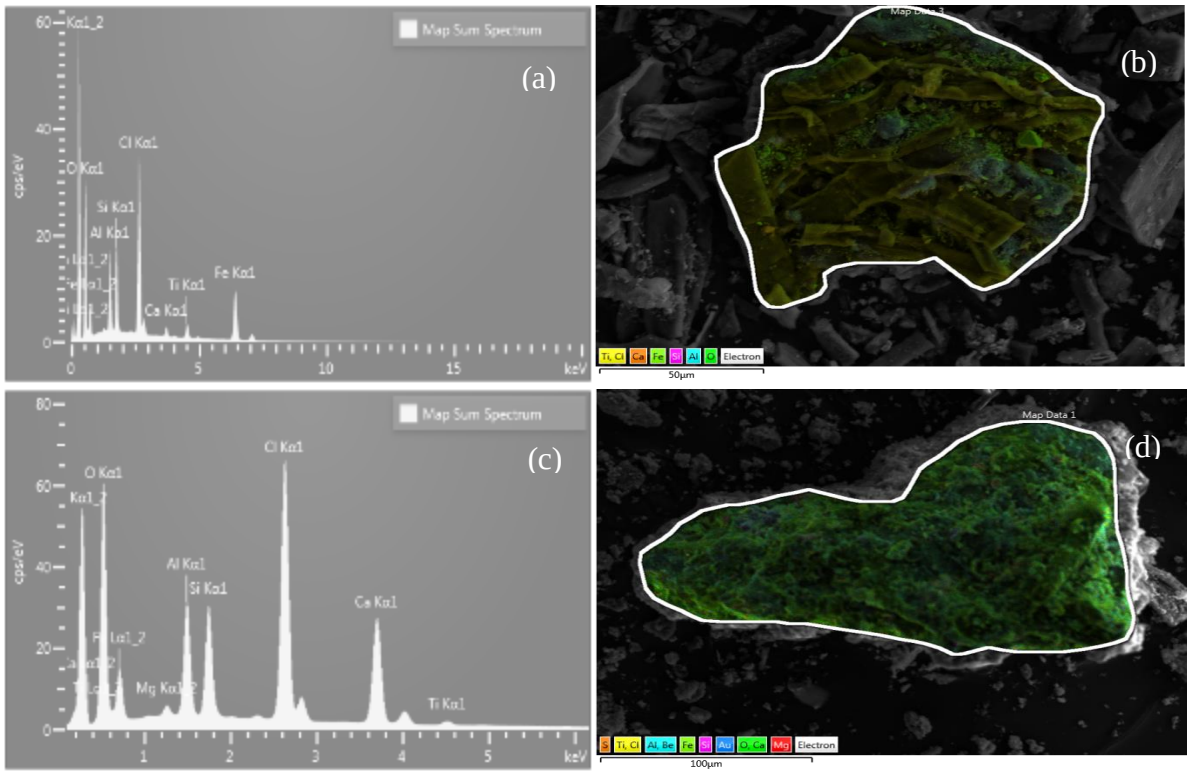

Appendix D - 6: EDS spectra and elemental mapping micrographs of resultant MBC 550ºC biochar (a) RPS spectra, (b) RPS elemental map, (c) SPS spectra, (d) SPS elemental map

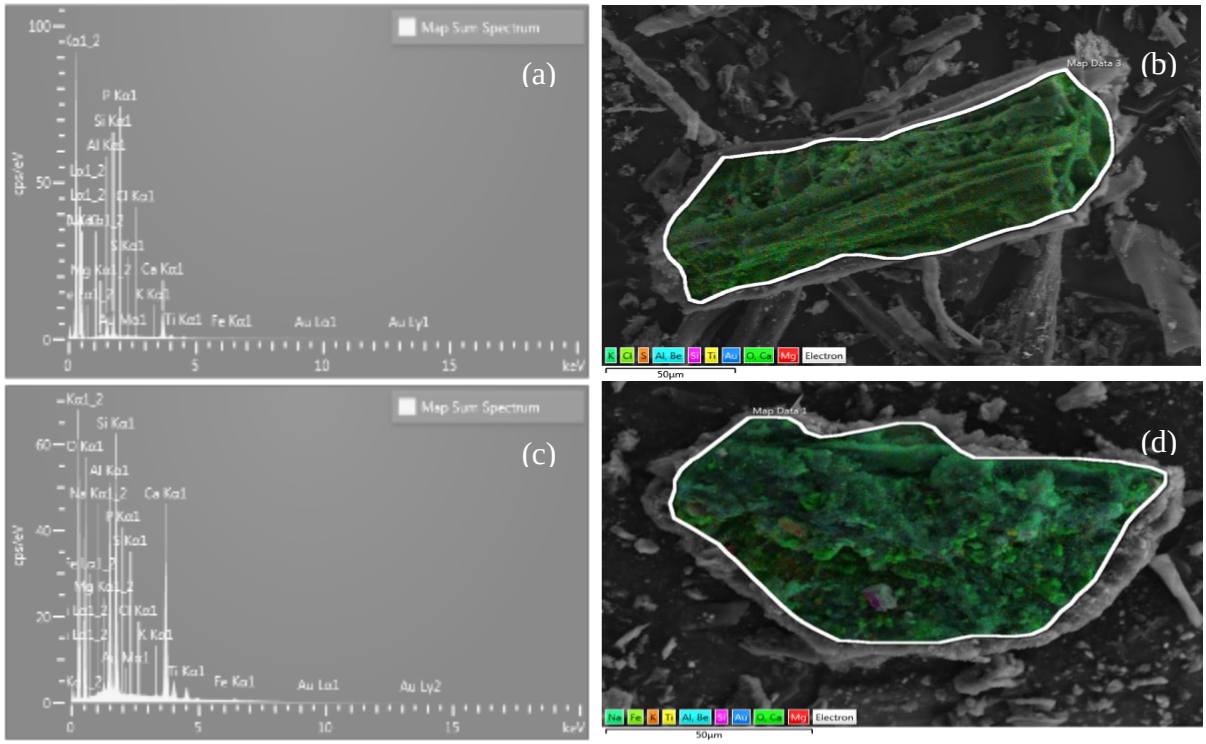

Appendix D - 7: EDS spectra and elemental mapping micrographs of resultant pristine 650ºC biochar (a) RPS spectra, (b) RPS elemental map, (c) SPS spectra, (d) SPS elemental map.

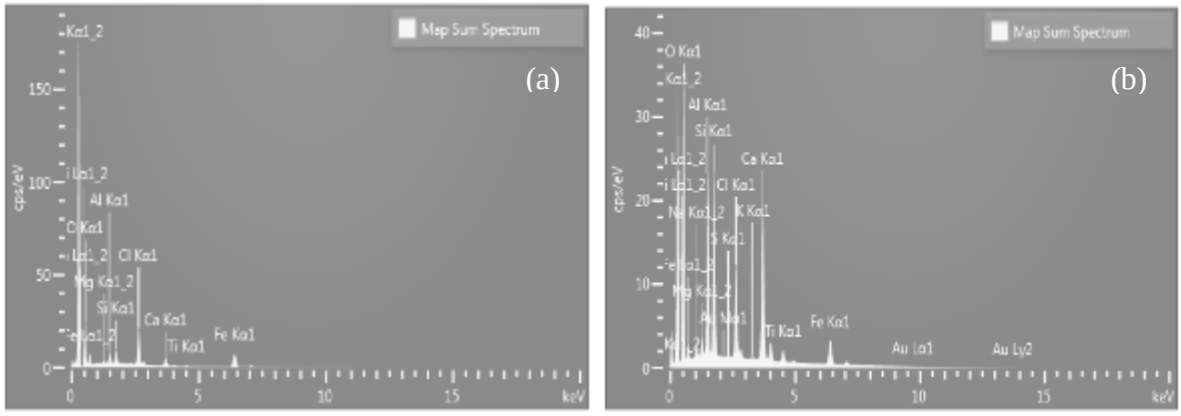

Appendix D - 8: EDS spectra of resultant MBC 650ºC biochar (a) RPS spectra and (b) SPS spectra

Appendix E: TEM micrographs of pristine and synthesized biochar.

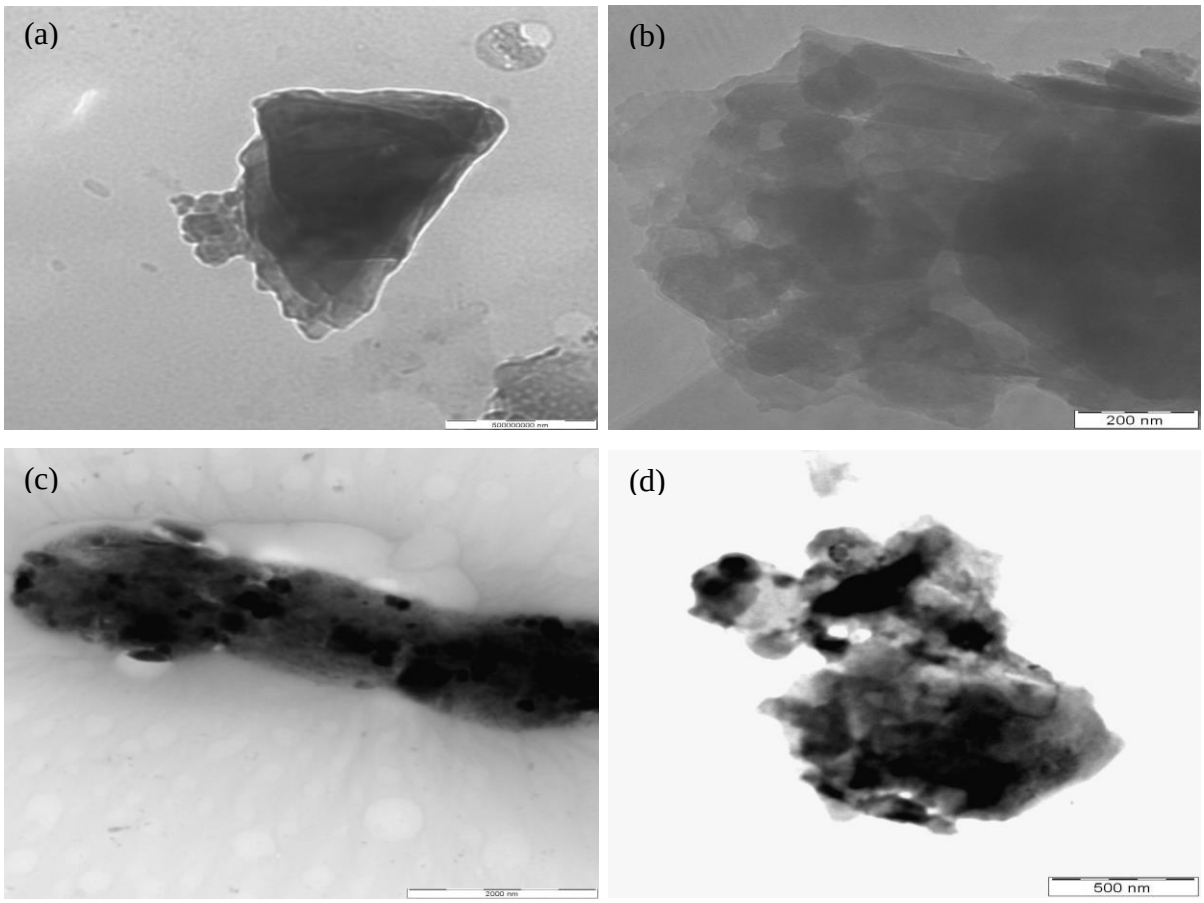

Appendix E- 1: TEM micrographs of resultant pristine and magnetic 550ºC biochar (a) SPS, (b) RPS, (c) MBC SPS, (d) MBC RPS

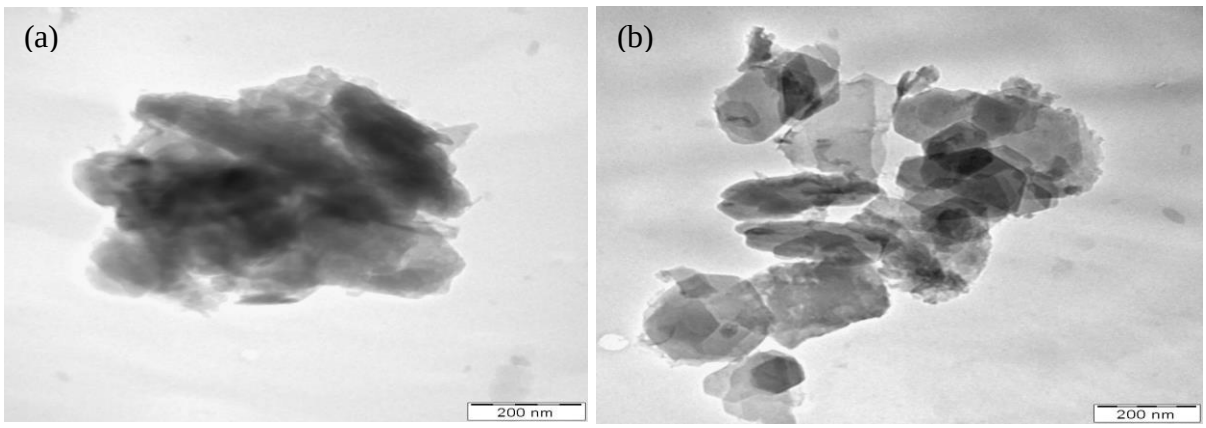

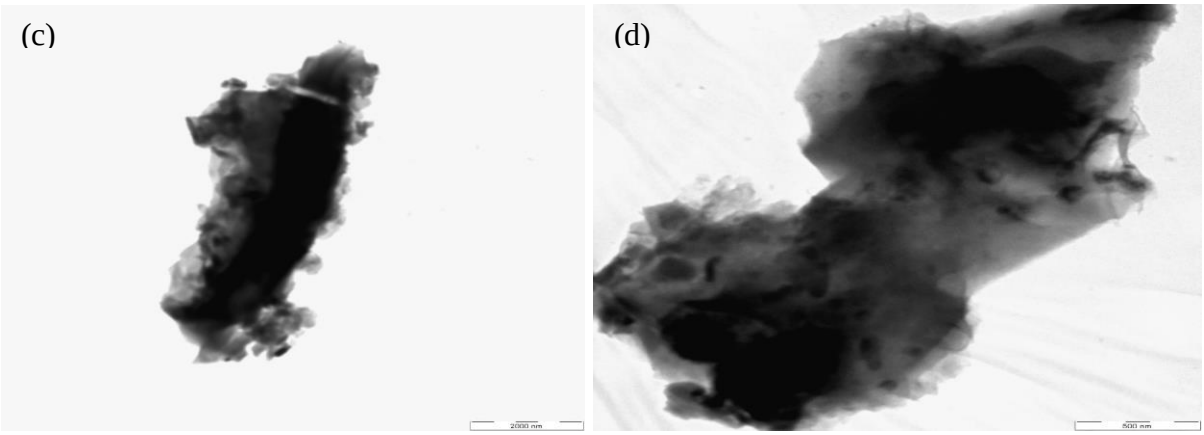

Appendix E- 2: TEM micrographs of resultant pristine and magnetic 650°C biochar (a) SPS, (b) RPS, (c) MBC SPS, (d) MBC RPS

Adsorption

Appendix F: Adsorption isotherms.

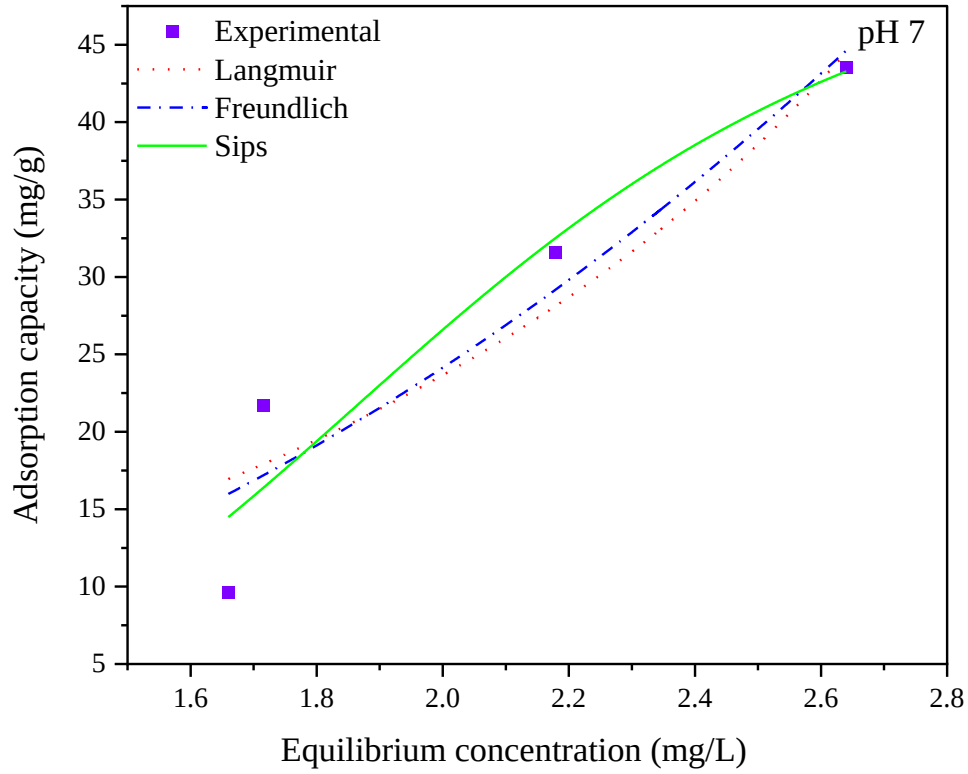

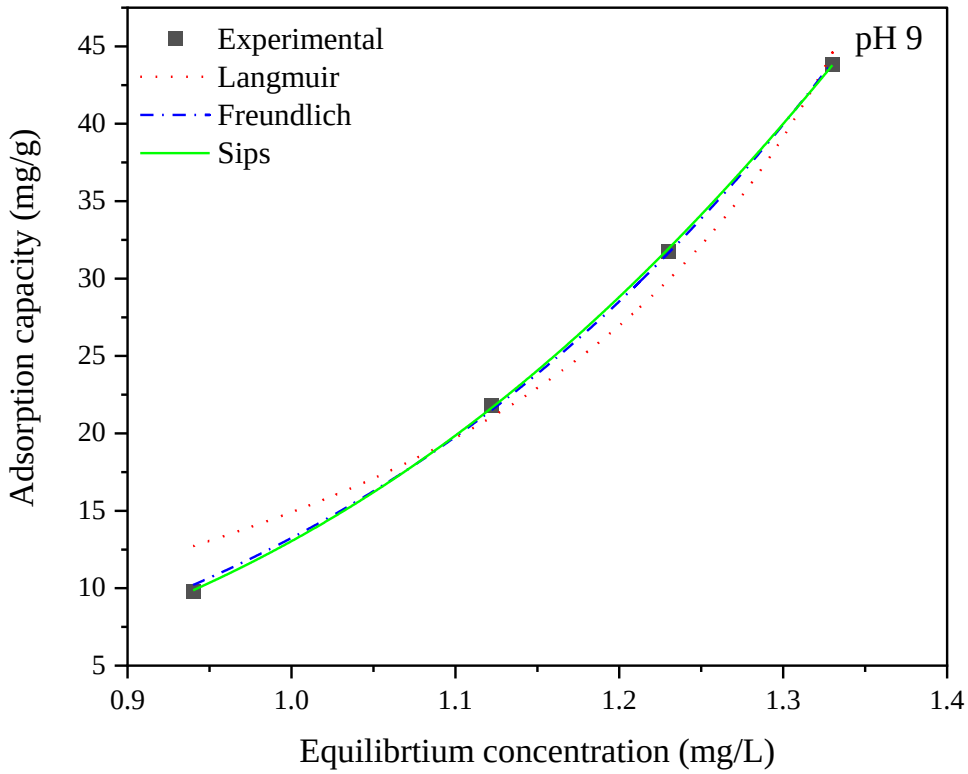

Appendix F - 1: Phosphorus adsorption isotherms at (a) pH 7 and (b) pH 9

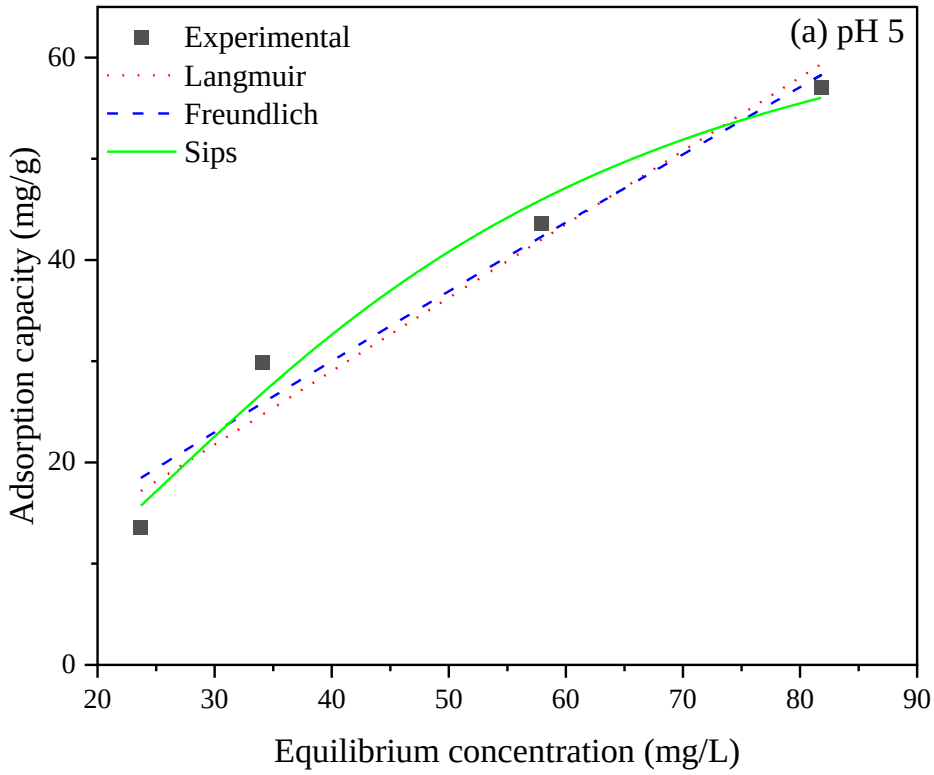

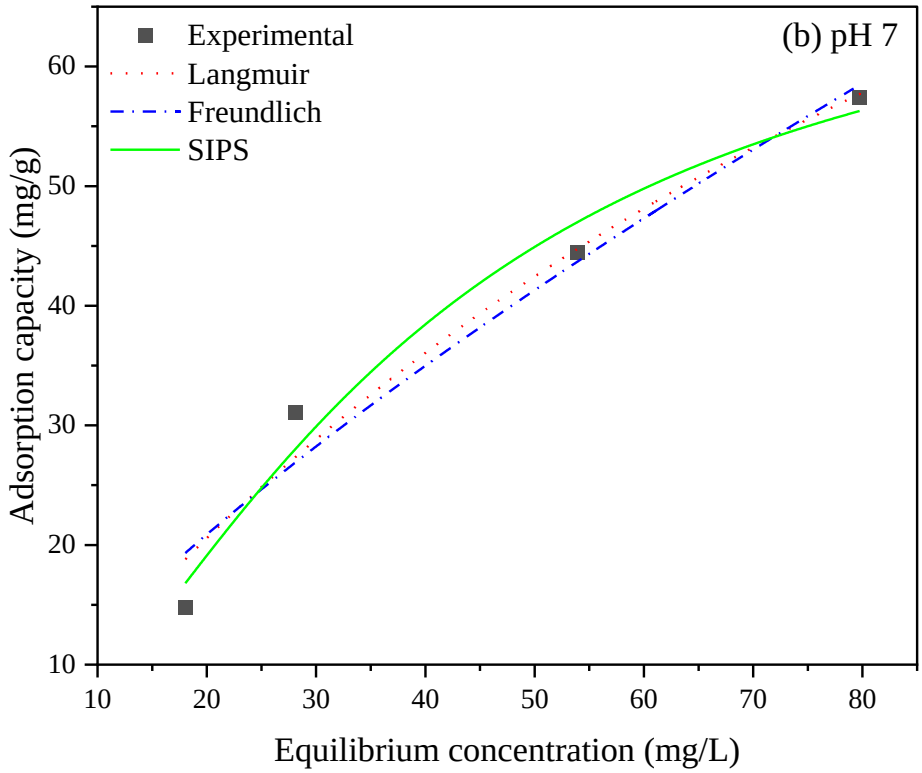

Appendix F - 2: Selenate adsorption isotherms at (a) pH 5 and (b) pH 7

Appendix G: Adsorption kinetic plots and parameters.

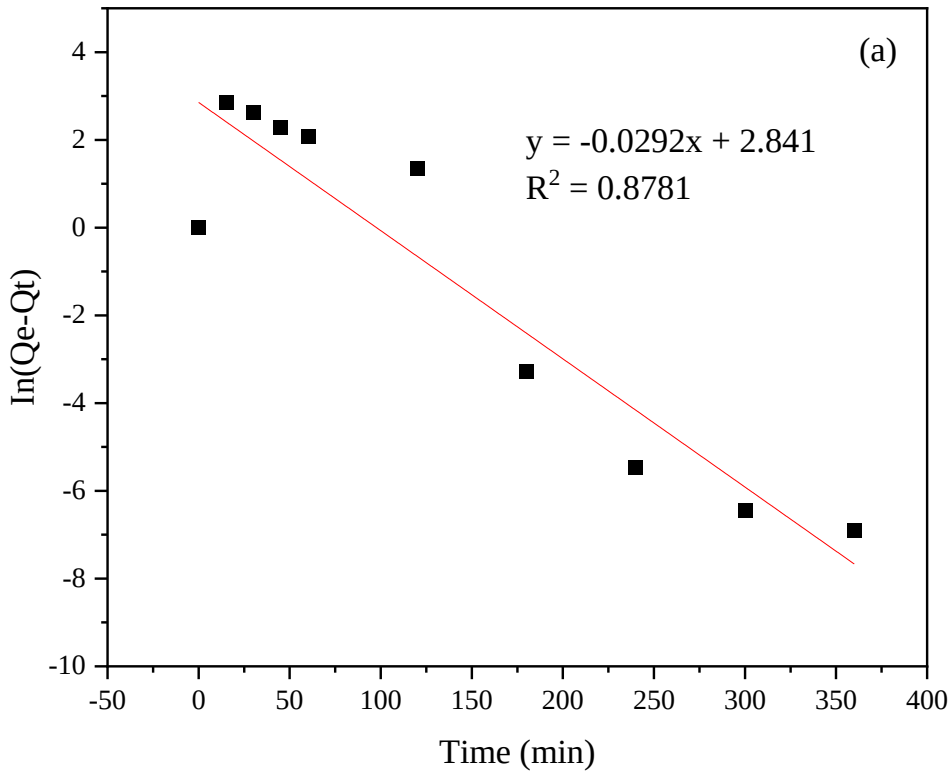

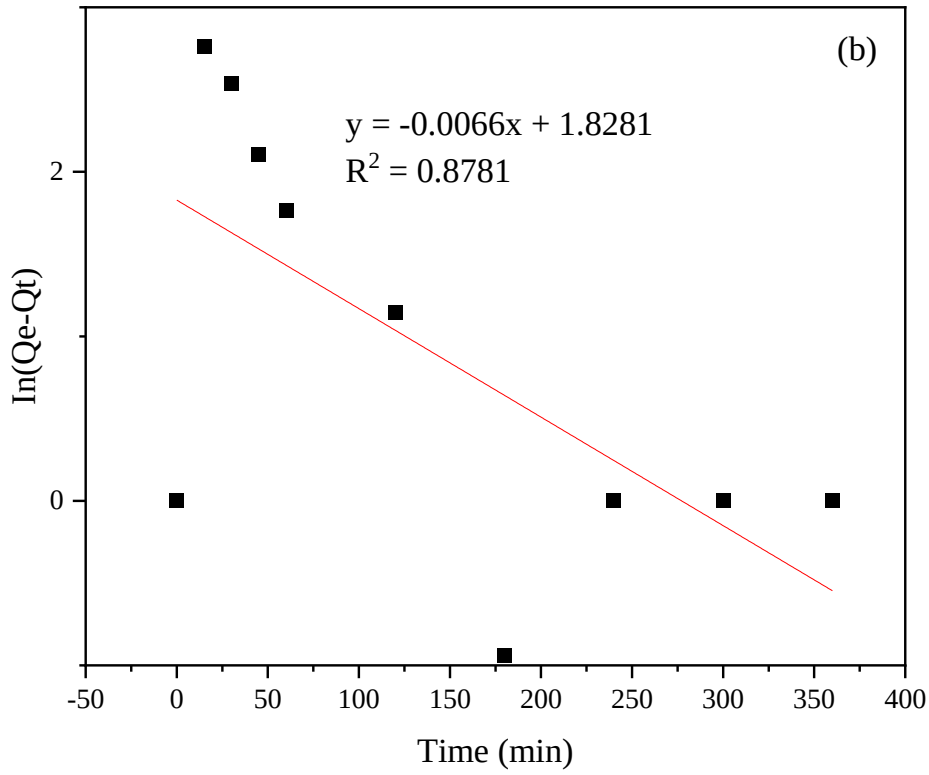

(b)

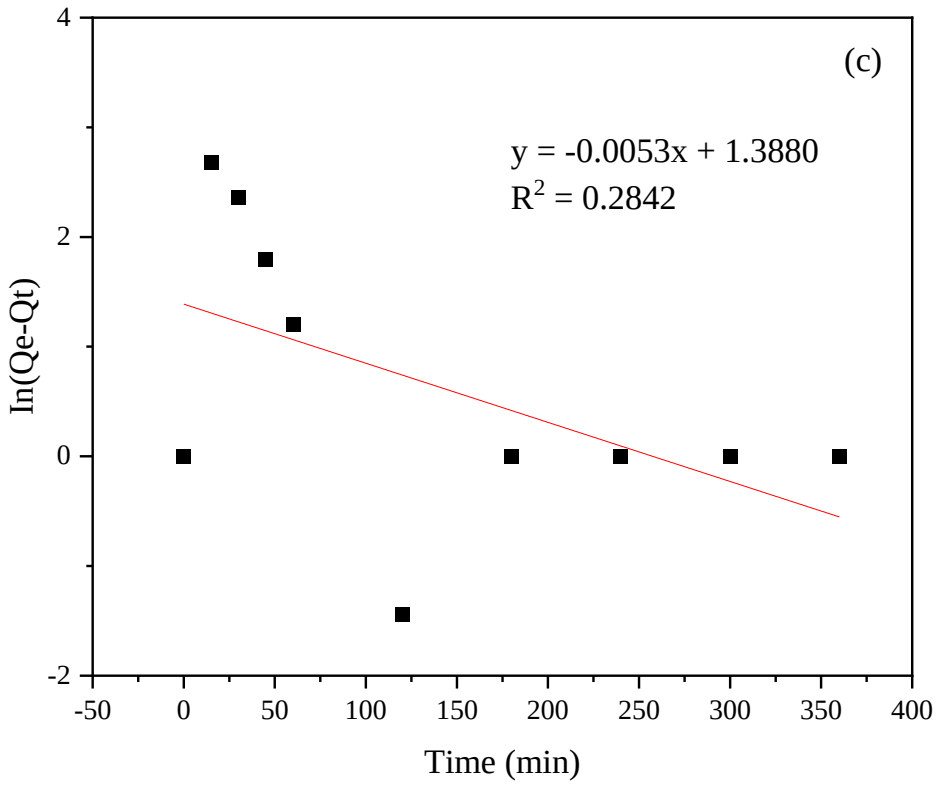

Appendix G- 1: Phosphorus Pseudo-First Order plots (a) pH 5, (b) pH 7 and (b) pH 9.

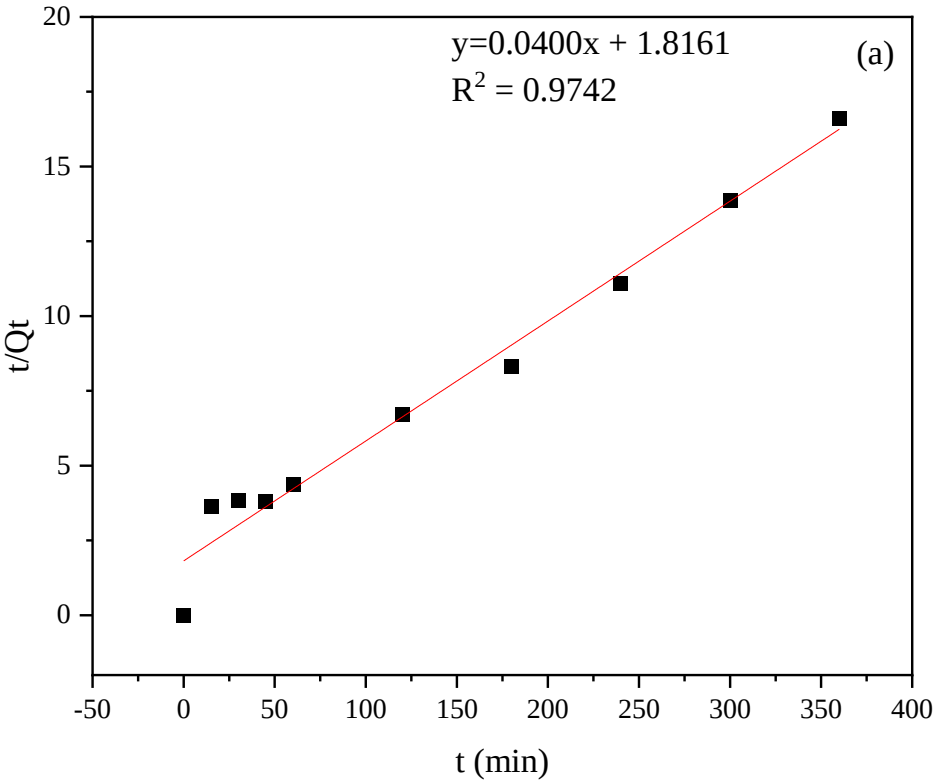

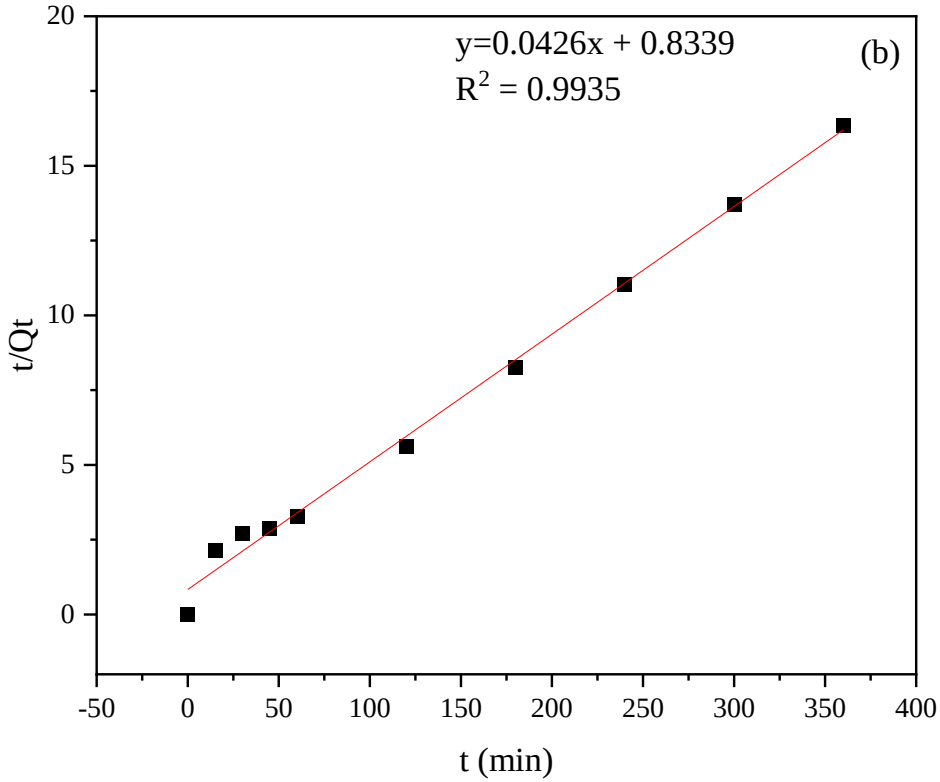

Appendix G- 2: Phosphorus Pseudo-Second Order plots (a) pH 5 and (b) pH 9.

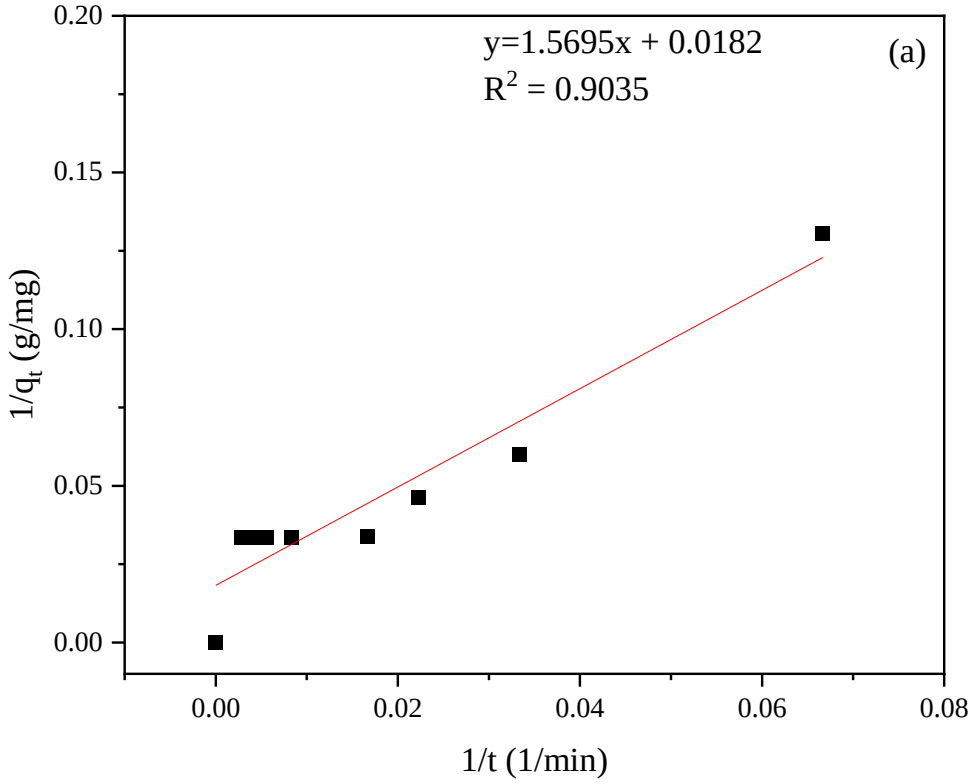

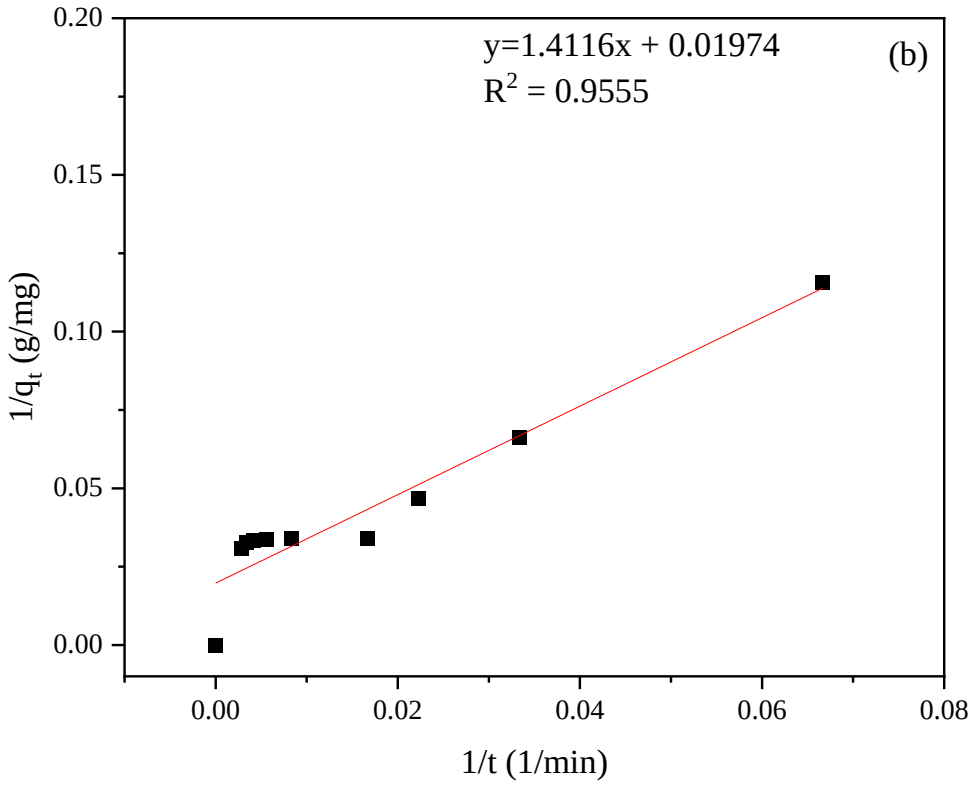

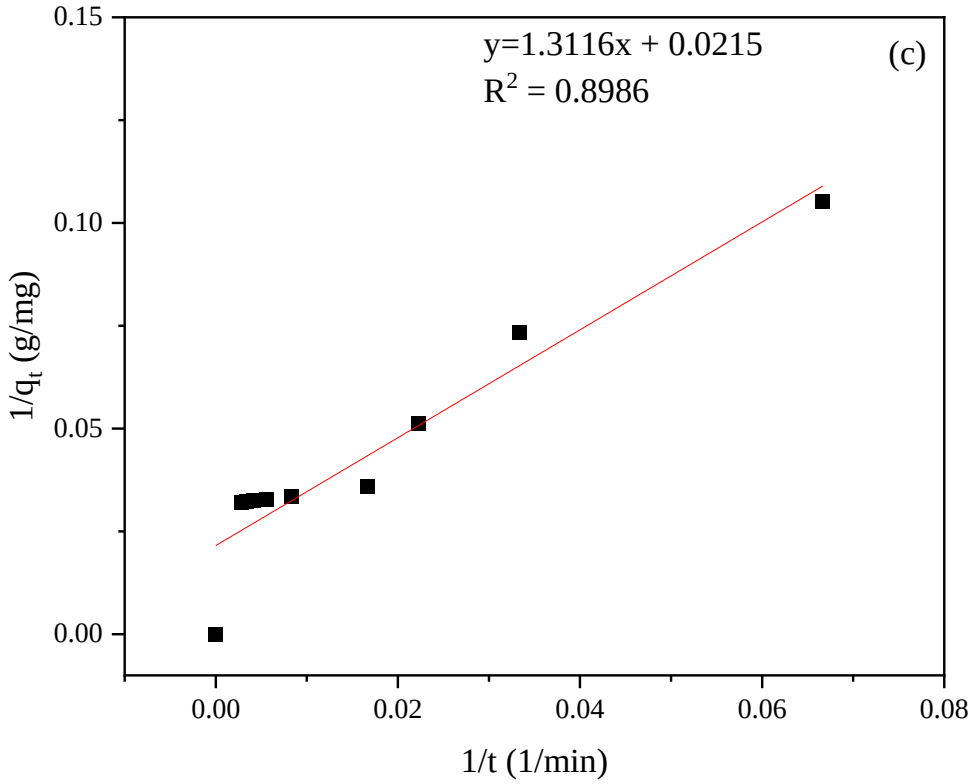

Appendix G- 3: Selenium Pseudo-First Order plots (a) pH 5, pH 7 and (b) pH 9

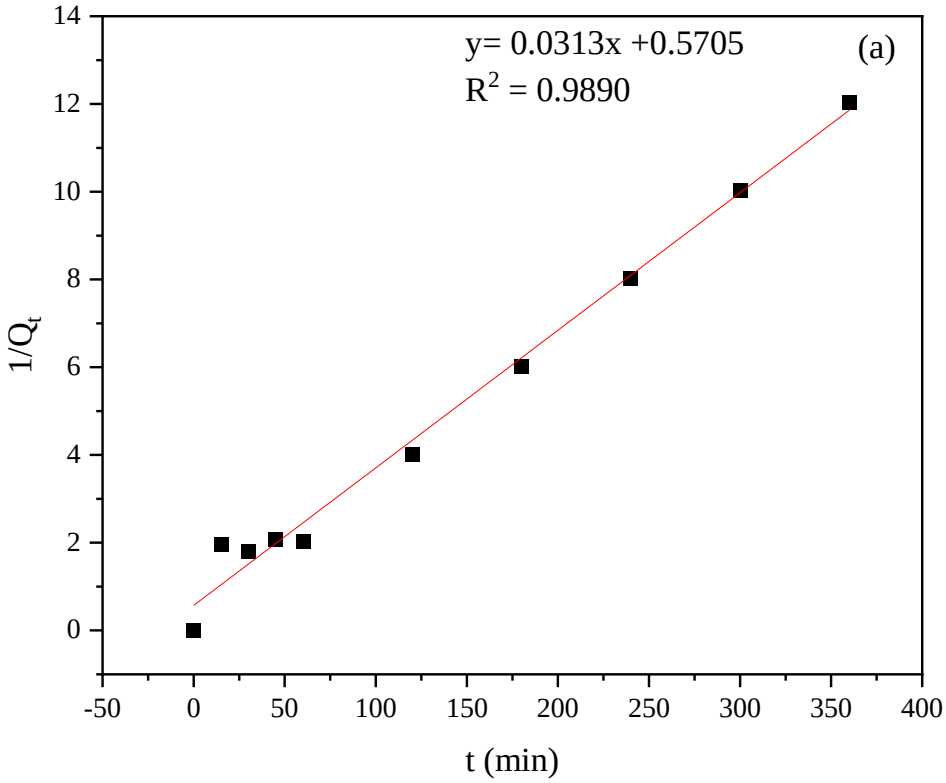

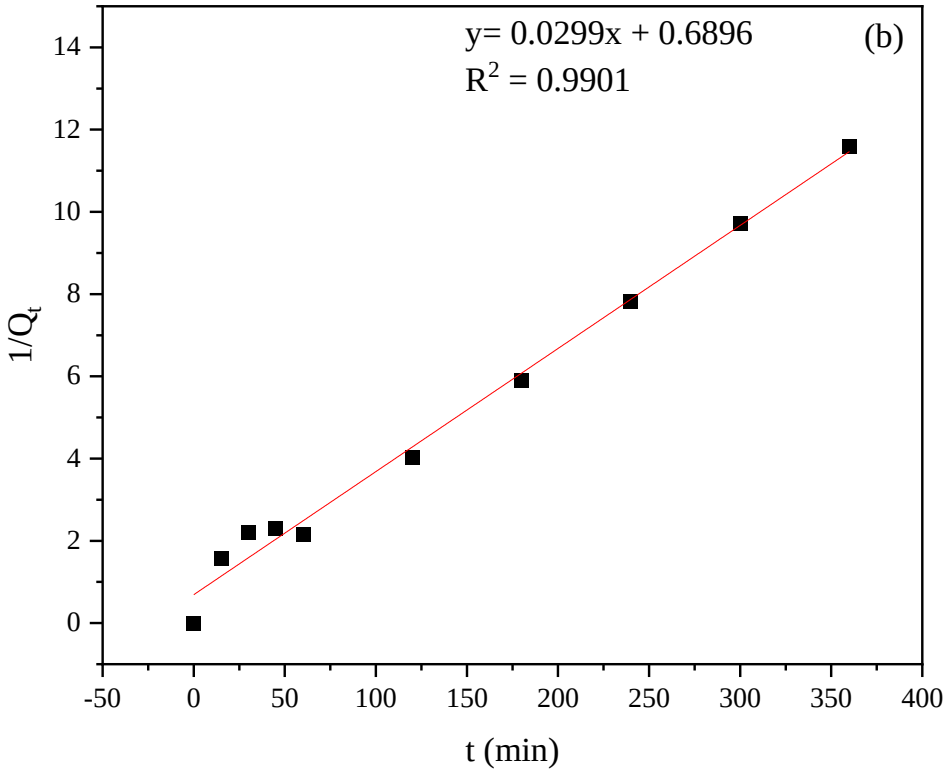

Appendix G- 4: Selenium Pseudo-Second Order plots (a) pH 5 and (b) pH 9

Appendix G- 5: Adsorption kinetic model parameters

Adsorbate		**Pseudo-First Order**			**Pseudo-Second Order**		
	pH	q_e ($L.g^{-1}$)	$K_1 \times 10^{-3}$ (min^{-1})	R 2	q_e ($mg.g^{-1}$)	$K_2 \times 10^{-3}$ ($g\ min^{-1} min^{-1}$)	R 2
P	5	17.35	-0.0811	0.878	24.95	0.88	0.974
	7	6.22	-0.0183	0.933	24.05	1.32	0.987
	9	1.03	4.746	0.284	234.30	0.02	0.993
Se	5	1.018	4.359	0.903	31.88	1.72	0.989
	7	1.019	3.921	0.913	33.40	1.29	0.990
	9	1.021	3.643	0.898	33.40	1.29	0.990
MB	7	1.31	79.99	0.814	2.02	57.79	0.968

Appendix H: UV Spectrophotometer calibration data

Concentration	Spectrophotometer Reading
0	0.001
2.5	0.252
5	0.765
7.5	1.173
10	1.525

$Y = mX + C$

Y	Residual concentration	
m	Gradient	6.2463
X	spectrophotometer reading	
C	Intercept	0.3578

Appendix H- 1: UV Spectrophotometer calibration

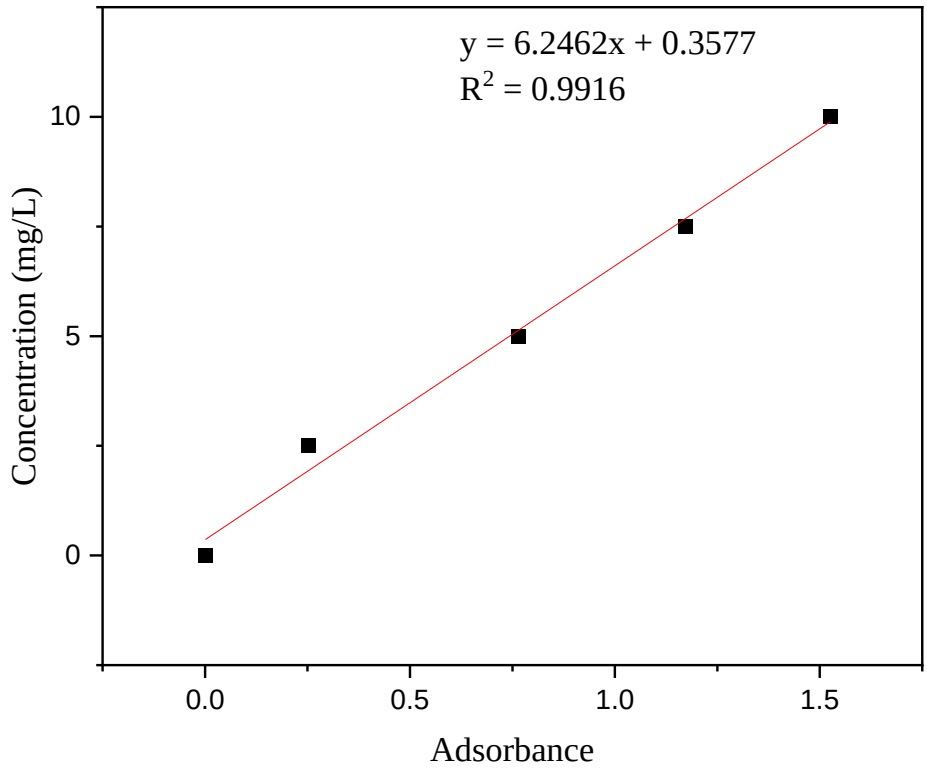

Appendix H- 2: UV Spectrophotometer calibration plot